Phase-Field Modelling of Crack Initiation and Propagation in Polycrystalline Materials under Thermomechanical Loadings

Dissertation
zur Erlangung des akademischen Grades

Doktoringenieur
(Dr.-Ing.)

von M.Sc. Zhengkun Liu
geb. am 27.07.1987 in Liaoning
genehmigt durch die Fakultät für Maschinenbau
der Otto-von-Guericke-Universität Magdeburg

Gutachter: Prof. Dr.-Ing. Daniel Juhre
Otto-von-Guericke-Universität Magdeburg

Prof. Dr.-Ing. Kerstin Weinberg
Universität Siegen

Promotionskolloquium am 26.02.2021

Zusammenfassung

Das Ziel dieser Doktorarbeit ist die Entwicklung eines Phasenfeldmodells, welches die mathematische Beziehung zwischen den thermomechanischen Belastungen und der Rissinitiierung sowie der Rissausbreitung in polykristallinen Werkstoffen beschreiben kann. Die Mikrostrukturen werden durch einen Voronoi-Tessellierungsalgorithmus erzeugt und jedes Korn ist zufällig orientiert. Die numerischen Beispiele zeigen die Fähigkeit des entwickelten Modells zur Vorhersage des thermomechanischen Risswachstums in polykristallinen Werkstoffen. Darüber hinaus werden die Auswirkungen der Korngröße auf das Bruchverhalten untersucht.

Abstract

A phase-field model for crack initiation and propagation in polycrystalline materials under thermomechanical loadings is proposed. Therefore, the thermomechanical coupling constitutive model is implemented, while an evolving phase-field captures the diffuse crack. Microstructures are generated by a Voronoi tessellation algorithm with randomly distributed material orientation for each grain. The numerical examples presented in this thesis demonstrate the capability of the proposed model to predict thermoelastic crack evolution in polycrystalline materials. Furthermore, the effects of grain size on the fracture behavior are investigated.

Contents

List of Figures

List of Tables

1

Introduction

1.1 Motivation and state of the art

Crack growth can lead to loss of structural integrity and catastrophic failure as shown in Fig. 1.1. Therefore, accurate prediction of crack development in technical structures and components plays a pivotal role in the most diverse industrial sectors, ranging from mechanical engineering to renewable energy [190].

Polycrystalline materials, such as alloys and ceramics, are composed of many small randomly oriented grains at micro- and mesostructural level. The macroscopic frac-

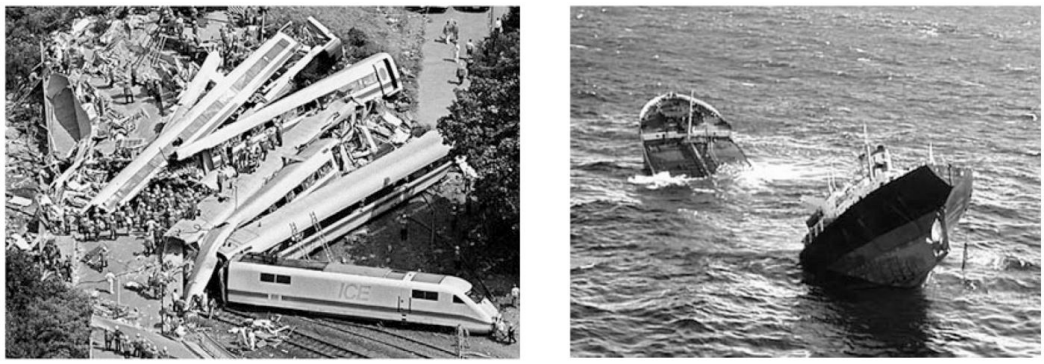

(**a**) (**b**)

Figure 1.1: Serious cases of engineering failures caused by crack growth in the recent past. **a** A high-speed ICE train disaster on June 3, 1998 [212]. **b** Collapse of the oil tanker Prestige on November 19, 2002 [212].

ture is originated mainly from crack evolution in the microstructure, and the direction of crack propagation is often changed from grain to grain depending on the grain orientation. Thus, failure prediction is essential for the development of high performance polycrystalline materials.

Thermally induced stress is one of the common causes of failures in polycrystalline materials, such as cooling of silicon carbide ceramics and thermal barrier coatings (TBCs) for high-pressure turbine blades. The inhomogeneous temperature gradients may lead to the emergence of complex crack patterns in polycrystalline materials.

Fig. 1.2 illustrates different failure stages in polycrystalline materials. It can be seen from the figure that the direction of crack propagation is not consistent. Furthermore, two types of fracture behavior, intergranular fracture (cracks following the grain boundaries) and transgranular fracture (cracks growing through the grains), are observed in this microstructure. Intergranular fracture may occur when the orientation of the neighbouring grain resists crack propagation from the neighboring transgranular fracture systems [184].

The total service life of polycrystalline materials is strongly influenced by the fracturing processes at micro- and mesostructural level (see Fig. 1.2). Moreover, the inho-

mogeneous stress distribution in polycrystalline solids may be considered as a random variable, which cannot be determined by means of analytical methods. Thus, highly accurate prediction of thermoelastic crack nucleation and propagation in polycrystalline materials is still a complex and challenging task [180, 184].

The aim of this work is to propose a phase-field model for simulating thermoelastic fracturing processes in polycrystalline materials, taking into account the thermoelastic fracture behavior of anisotropic materials.

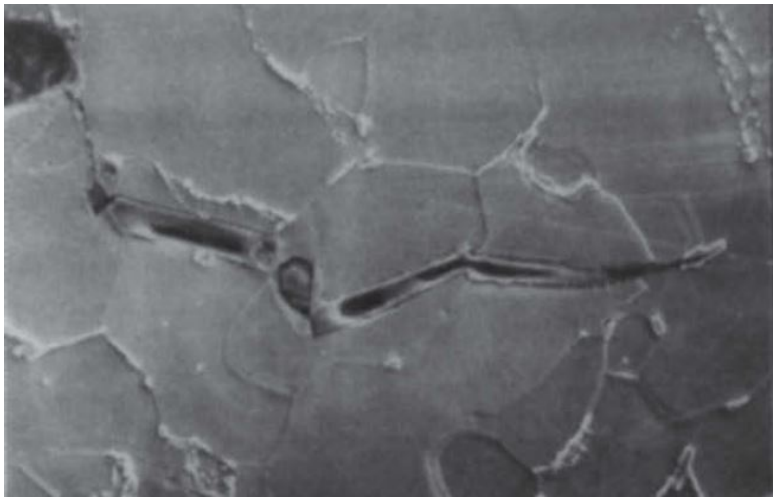

Figure 1.2: Crack nucleation and propagation in polycrystalline materials [14].

1.1.1 Phase-field models for isotropic brittle fracture

The fundamental theory to predict crack initiation and propagation in brittle solids was given by Griffith [101]. In order to deal with the stress field ahead the crack tip, the stress intensity factor was introduced by Irwin [121]. Analytical methods are mostly used to solve simple problems of fracture mechanics. However, research has consistently shown that the fracture problems comprise special characteristics, e.g. complex geometries and boundary conditions. Hence, a considerable amount of literature has been published on advanced computational techniques for simulating crack

growth, e.g. the extended finite element method (XFEM), the embedded finite element method (EFEM), cohesive zone models (CZM), virtual crack closure technique (VCCT) and linear elastic fracture mechanics (LEFM) [173]. The main challenge faced by many researchers is that the application of these methods has some limitations, such as tracking of arbitrary propagation, branching and pattern of cracks. To circumvent these drawbacks, a new strategy called phase-field method was developed in the late 1990's. In this method, the crack surface is represented by the diffuse phase-field parameter s which ensures a continuous transition between undamaged ($s = 1$) and totally damaged material ($s = 0$). Based on the phase-field evolution equation, the requirement for additional ad-hoc criteria is removed. This specific feature results in that the phase-field method has a big advantage over the discrete approach for modelling curved crack paths, crack kinking and branching angles, as well as crack-front segmentation [50]. The phase-field model for brittle fracture which unfolded from the pioneering work of Francfort & Marigo [87] has been improved by many researchers [52, 166, 171]. Furthermore, the phase-field method has been extended to simulate ductile fracture [10, 12, 27], crack propagation at finite strains [34], cohesive fracture [57, 84, 191], crack propagation in shell structures [126, 127] and fatigue crack growth [154, 226, 228], as well as dynamic fracture [110, 114, 115].

The phase-field model for brittle fracture was first proposed by Bourdin et al. [41] (see also [42, 190, 235, 252]). The model proposed by Bourdin et al. [41] is numerically isotropic in the sense that there is no distinction between the fracture behavior in tension and compression.

In order to avoid physically unrealistic crack evolution under compressive loadings, the volumetric/deviatoric split was proposed by Amor et al. [13]. In their method, the elastic strain energy density is decomposed into a volumetric part and a deviatoric part. In case of compression, the degradation function is only allowed herein

to be coupled with the deviatoric part of the elastic strain energy density. The volumetric/deviatoric split has been applied by many researchers [132, 221, 223, 224]. Alternatively, Miehe et al. [169] introduced a spectral split based on the spectral decomposition of elastic strains together with the assumption that the evolution of the crack phase-field is only conducted by positive principal elastic strains. Various studies have been carried out by means of the spectral split [49, 126, 179, 295]. In order to take advantage of the linear nature of the isotropic model [41] whilst preserving unrealistic crack evolution in compression, the hybrid model was introduced by Ambati et al. [11]. That is, the stress-strain relation is still given from the isotropic model [41], while a different one is postulated for the driving energy density in the phase-field evolution equation that is associated with those numerically anisotropic phase-field models [13, 169]. This numerical feature has attracted considerable attention (see also [69, 123, 205, 277, 294]).

Despite the growing applications of the phase-field method in modelling crack growth in compression, none of the exciting models are capable of capturing crack propagation under compressive loadings correctly [145]. Moreover, until now, self-contacts algorithms have not yet been implemented in the phase-field modelling of fracture.

1.1.2 Phase-field models for brittle fracture in polycrystalline materials

Nowadays, many components in engineering and industrial applications are designed using polycrystalline materials (e.g. metals, alloys and ceramics). However, conventional methods such as strength calculation cannot be used to simulate crack propagation in polycrystals, and the modelling of inter- and transgranular crack propagation may be a major challenging task to study among many researchers [28, 230, 248].

In order to accurately simulate crack nucleation and propagation in polycrystalline materials, many numerical methods have been developed in the past few decades. These methods can be broadly divided into two categories: discrete crack approach and diffuse crack approach.

In the discrete crack approach, the sharp crack topology is represented using a singular element near the crack tip, in which stress intensity factors (SIFs) can be precisely calculated. Sfantos & Aliabadi [230] employed the boundary element method (BEM) for modelling intergranular crack propagation in polycrystals. This work has been extended by Benedetti et al. [30] to simulate stress-corrosion cracking (SCC) in polycrystalline structures. More recently, the dual boundary element method (DBEM) was applied for modelling crack evolution in polycrystalline materials [197, 198]. Furthermore, Sukumar et al. [248] simulated crack propagation through a polycrystalline structure by means of the extended finite element method (XFEM), which involves local enrichment of approximation spaces based on the partitioning of unity concept. However, this method is very time consuming, especially in the calculation of complex crack paths.

Until now, the number of contributions concerning the phase-field modelling of crack initiation and propagation in polycrystalline materials is very limited. Clayton & Knap [55] carried out a phase-field model for three-dimensional fracture propagation in polycrystalline materials at finite deformations. In their work, a second order tensor $\boldsymbol{\omega}$ was used to enforce the crack propagation along one preferential plane. Nguyen et al. [184] used as well this phase-field model for simulating the failure process in polycrystalline solids whereas they extended the simulation by inserting cohesive zone elements in terms of grain boundaries to investigate the effect of interphase failure processes. Here, the elastic strain energy density function was modified under compressive loadings, and a staggered solution scheme within the finite element

framework was used. Some selected parameters in the proposed anisotropic phase-field model were analyzed. Paggi et al. [190] presented a phase field model for brittle fracture to apply it for crack propagation in solar-grade polycrystalline silicon. The isotropic phase-field model for crack propagation in brittle solids was applied whereas the value of the critical energy release rate depends on the material orientation [41].

1.1.3 Phase-field models for thermoelastic fracture in polycrystalline materials

Thermal stress induced fracture has gained considerable attention among many researchers, because the temperature gradient plays a pivotal role in the fracturing process [93, 94]. The investigations in this contribution are exclusively related to spontaneous processes where time-dependent mechanisms should not play an important role.

Evans [78] presented the experimental analysis of microcrack nucleation and growth caused by anisotropic thermal expansion. Further on, the experimental investigations of the effects of the residual stresses on thermoelastic fracture behavior in alumina ceramics were carried out by Yousef et al. [284].

In order to reduce the experimental costs and make new representations which are experimentally impossible, numerical methods have been applied. In the work by Prasad et al. [199, 201], DBEM was applied for solving thermoelastic fracture problems. Willam et al. [270] introduced zero-thickness interface models for thermoelastic damage evolution in heterogeneous materials. In the work by Zamani & Eslami [285], XFEM was used for simulating dynamic thermal fracture. More recently, Sapora & Paggi [216] proposed a coupled cohesive zone model for modelling thermally induced debonding phenomena at imperfect interfaces. Geraci & Aliabadi [93, 94] introduced a thermomechanical cohesive model for predicting inter- and transgranular fracturing

processes in polycrystalline materials under thermomechanical loadings.

Some applications of phase-field models to thermomechanical fracture are reported for instance in [132, 164, 168, 223]. Corson et al. [58] proposed a phase-field model for simulating oscillatory crack evolution in brittle materials under thermomechanical loadings. Bourdin et al. [42] introduced a phase field model for dynamic thermal fracture. Dittmann et al. [68] developed a phase-field model to solve thermo-fracture mechanical contact problems at finite strains. Badnava et al. [23] introduced an adaptive phase-field method to simulate thermoelastic crack growth in brittle materials. Nguyen et al. [185] proposed a chemo-thermo-mechanical phase-field model for simulating complex fracturing processes in cement-based materials. In the work by Wang et al. [264], explicit time-integration schemes were applied for solving thermomechanical fracture problems.

All those phase-field models neglected the anisotropic thermal properties, and the investigation of the effects of grain size on the fracture behavior in polycrystalline solids was still missing. Therefore, the anisotropic properties, such as anisotropic elastic modulus, anisotropic thermal conductivity, and anisotropic thermal deformation, need to be considered in the proposed model. Moreover, the proposed model should be able to simulate various kinds of thermomechanical fracturing processes, i.e. thermoelastic crack propagation: (i) in a sole material; (ii) in a bi-material; (iii) in a multi-layered material; (iv) in polycrystalline materials.

1.1.4 Adaptive phase-field models for brittle fracture

The spatial discretization h cannot be larger than the crack width κ in the implementation of finite element methods for phase-field modelling of crack initiation and propagation [114, 115]. In other words, the phase-field model for fracture needs a fine mesh rather than a coarse mesh [108]. The most trivial one is the globally pre-defined

mesh wherein the high solution accuracy is achieved by a very large number of mesh elements, hence the globally pre-defined mesh becomes computationally expensive [179]. One of the other methods that has proven its ability to reduce the computational time is the locally pre-defined mesh. However, the locally pre-defined mesh refinement cannot be applied to simulate crack evolution at arbitrary locations since the (unknown) crack path is dependent on the locally pre-defined mesh refinement [107]. In contrast to the uniform and locally pre-defined mesh refinements, the adaptive mesh refinement allows us to recover optimal convergence rates [108]. Burke et al. [45] first proposed the adaptive phase-field model for crack evolution in brittle materials. Borden et al. [40] developed an adaptive phase-field model to solve dynamic fracture problems. Heister et al. [107] proposed a primal-dual active set method and predictor-corrector mesh strategy for simulating crack nucleation and propagation in two-dimensional structures. This work has been extended to solve three-dimensional fracture problems [108], too. Multi-level *hp*-refinement was applied for phase-field modelling of crack propagation in the work by Nagaraja et al. [179]. Mang et al. [157] introduced a residual-type error estimator for adaptive phase-field analysis of crack growth. However, the most adaptive phase-field models were applied to simulate crack growth in tension and shear. Few attention was paid to the simulation of crack evolution in compression and therefore further studies would be necessary.

1.2 Research objectives and overview

In the first step, the existing phase field models are derived and reviewed. Next, simulations of compressive fracturing processes are performed. Furthermore, representative examples are applied to illustrate the potential of the proposed model for simulating thermoelastic crack evolution in polycrystalline materials. At last, an adaptive phase-field model is used for modelling compressive crack growth.

This thesis is structured as follows: In Chapter 2, the basic concepts of continuum mechanics and thermodynamics are presented. The review focuses on the balance equations for mass, linear momentum, angular momentum, energy and entropy.

Chapter 3 introduces phase-field models for brittle fracture. On this subject, Griffith's criterion in the linear elastic fracture mechanics is first presented. This chapter further reviews the diffuse description of crack surfaces by means of the phase-field method. Thereafter, the theory pertaining to the variational phase-field approach for brittle fracture is provided.

Chapter 4 starts with a quasi-static fracture problem. The performances of four commonly used phase-field models for simulating crack evolution are investigated. Furthermore, the compressive fracturing processes in a specimen containing two parallel preexisting cracks are simulated, and the results are discussed in detail.

Chapter 5 and Chapter 6 demonstrate the capability of the proposed model for predicting crack evolution in anisotropic solids under isothermal and non-isothermal conditions.

In Chapter 7 an adaptive mesh refinement strategy [107] is used for modelling compressive fracturing processes in a PBX 9502 plate.

Chapter 8 concludes the thesis and gives an outlook on future research.

2

Basics of continuum mechanics

This chapter describes the basic relations concerning continuum mechanics and thermodynamics. In Sect. 2.1, the basic concepts of kinematics are reviewed under the assumption of small deformations. Next, the balance equations of mass, linear and angular momentum, and the fundamental laws of thermodynamics are described in Sect. 2.2. Furthermore, the Hamilton's principle is introduced in Sect. 2.3. For an in-depth understanding of continuum mechanics the reader is referred to standard books, e.g. Bertram & Glüge [32], Betten [33], Bower [43], Naumenko & Altenbach

[180] and Willner [271]. The basic concept of continuum mechanics is presented in the lecture notes of Steinmann [244].

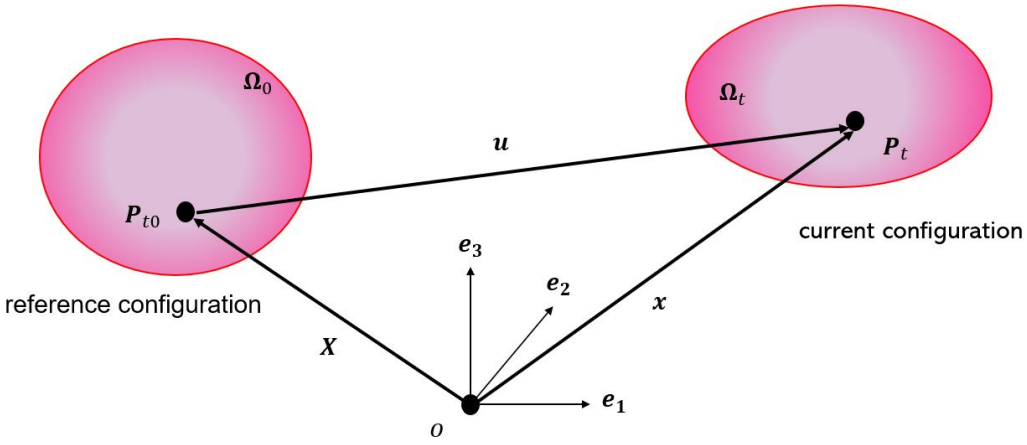

Figure 2.1: Material domain at the reference (undeformed, Ω_0) and current (deformed, Ω_t) configurations.

2.1 Kinematics

The statements in this chapter refer to a deformable material domain Ω with boundary $\partial\Omega$ in Euclidean space $\mathbb{E}^3$ as shown in Fig. 2.1. The initial position of the material point P in the reference configuration is denoted with $\boldsymbol{X}$. Its position in the current configuration is referred to as $\boldsymbol{x}$. The motion is described by a mapping of the initial position of a material point P in the reference configuration Ω_0 at time t_0 into the current configuration Ω_t at time t, i.e.

$$\boldsymbol{x} = \varphi(\boldsymbol{X}, t). \tag{2.1}$$

The displacement vector $\boldsymbol{u}$ is defined as

$$\boldsymbol{u} = \boldsymbol{x} - \boldsymbol{X}. \tag{2.2}$$

The velocity vector $\boldsymbol{v}$ and acceleration vector $\boldsymbol{a}$ are obtained from the time derivative of the displacement vector $\boldsymbol{u}$, i.e.

$$\boldsymbol{v} = \frac{\mathrm{d}\boldsymbol{u}}{\mathrm{d}t} = \dot{\boldsymbol{x}}, \tag{2.3}$$

and

$$\boldsymbol{a} = \frac{\mathrm{d}\boldsymbol{v}}{\mathrm{d}t} = \frac{\partial \boldsymbol{v}(\boldsymbol{X}, t)}{\partial t} = \dot{\boldsymbol{v}} = \ddot{\boldsymbol{x}}. \tag{2.4}$$

The deformation gradient describes the deformation of infinitesimal vectorial line elements

$$\boldsymbol{F}(\boldsymbol{X}, t) = \frac{\partial \boldsymbol{x}}{\partial \boldsymbol{X}} = \frac{\partial \varphi}{\partial \boldsymbol{X}} = \frac{\partial (\boldsymbol{X} + \boldsymbol{u}(\boldsymbol{X}, t))}{\partial \boldsymbol{X}} = \mathbf{1} + \nabla \boldsymbol{u}(\boldsymbol{X}, t), \tag{2.5}$$

where $\mathbf{1}$ denotes the identity tensor of second order. The deformation gradient is non-singular, i.e.

$$\boldsymbol{F}\mathrm{d}\boldsymbol{X} \neq 0 \quad \text{for all} \quad \mathrm{d}\boldsymbol{X} \neq 0. \tag{2.6}$$

Consequently, the determinant of the deformation gradient is non-zero

$$J = \det \boldsymbol{F} \neq 0, \tag{2.7}$$

and thus the inverse of the deformation gradient is defined as

$$\boldsymbol{F}^{-1} = \frac{\partial \boldsymbol{X}}{\partial \boldsymbol{x}} = \frac{\partial \varphi^{-1}(\boldsymbol{x}, t)}{\partial \boldsymbol{x}}. \tag{2.8}$$

According to the polar decomposition theorem, the deformation gradient $\boldsymbol{F}$ can be rewritten as

$$\boldsymbol{F} = \boldsymbol{R}\boldsymbol{U} = \boldsymbol{V}\boldsymbol{R}, \quad \boldsymbol{R}^T\boldsymbol{R} = \mathbf{1}, \quad \boldsymbol{U} = \boldsymbol{U}^T, \quad \boldsymbol{V} = \boldsymbol{V}^T, \tag{2.9}$$

with a rotation tensor $\boldsymbol{R}$, a right stretch tensor $\boldsymbol{U}$ and a left stretch tensor $\boldsymbol{V}$.

For the description of strains during the motion of a body the change in squared length of these elements $\mathrm{d}s^2 = \mathrm{d}\boldsymbol{x} \cdot \mathrm{d}\boldsymbol{x}$ and $\mathrm{d}S^2 = \mathrm{d}\boldsymbol{X} \cdot \mathrm{d}\boldsymbol{X}$ is given by

$$\begin{aligned} \mathrm{d}\boldsymbol{x} \cdot \mathrm{d}\boldsymbol{x} - \mathrm{d}\boldsymbol{X} \cdot \mathrm{d}\boldsymbol{X} &= \boldsymbol{F}\mathrm{d}\boldsymbol{X} \cdot \boldsymbol{F}\mathrm{d}\boldsymbol{X} - \mathrm{d}\boldsymbol{X} \cdot \boldsymbol{1}\mathrm{d}\boldsymbol{X} = \mathrm{d}\boldsymbol{X} \cdot \boldsymbol{F}^T\boldsymbol{F}\mathrm{d}\boldsymbol{X} - \mathrm{d}\boldsymbol{X} \cdot \boldsymbol{1}\mathrm{d}\boldsymbol{X} \\ &= \mathrm{d}\boldsymbol{X} \cdot \left(\boldsymbol{F}^T\boldsymbol{F} - \boldsymbol{1}\right) \mathrm{d}\boldsymbol{X} = \mathrm{d}\boldsymbol{X} \cdot (\boldsymbol{C} - \boldsymbol{1})\mathrm{d}\boldsymbol{X} = \mathrm{d}\boldsymbol{X} \cdot 2\boldsymbol{E}\mathrm{d}\boldsymbol{X}, \end{aligned} \tag{2.10}$$

where $\boldsymbol{C} = \boldsymbol{F}^T\boldsymbol{F}$ is denoted as the right Cauchy-Green tensor, and $\boldsymbol{E}$ is defined as the Green-Lagrange strain tensor

$$\begin{aligned} \boldsymbol{E} &= \frac{1}{2}\left(\boldsymbol{C} - \boldsymbol{1}\right) = \frac{1}{2}\left(\boldsymbol{F}^T\boldsymbol{F} - \boldsymbol{1}\right) = \frac{1}{2}\left([\boldsymbol{1} + \nabla\boldsymbol{u}]^T[\boldsymbol{1} + \nabla\boldsymbol{u}] - \boldsymbol{1}\right) \\ &= \underbrace{\frac{1}{2}\left(\nabla\boldsymbol{u} + [\nabla\boldsymbol{u}]^T\right)}_{\boldsymbol{E}_{\mathrm{lin}} = \boldsymbol{\varepsilon}} + \underbrace{\frac{1}{2}[\nabla\boldsymbol{u}]^T\nabla\boldsymbol{u}}_{\boldsymbol{E}_{\boldsymbol{n}1}}. \end{aligned} \tag{2.11}$$

In this work the deformations are assumed to be small, i.e. $\|\nabla\boldsymbol{u}\| \ll 1$. Therefore, the quadratic term in Eq. (2.11) can be neglected, and the Green-Lagrange strain tensor $\boldsymbol{E}$ reduces to the infinitesimal strain tensor $\boldsymbol{\varepsilon}$

$$\boldsymbol{\varepsilon} = \frac{1}{2}\left(\nabla\boldsymbol{u} + [\nabla\boldsymbol{u}]^T\right). \tag{2.12}$$

2.2 Balance equations

This section describes the fundamental balance equations in continuum mechanics, such as balance equations of mass, linear and angular momentum, energy and entropy.

2.2.1 Balance of mass

The mass m of a solid body is obtained by integration

$$m(\boldsymbol{x}, t) = \int_{\Omega} \rho(\boldsymbol{x}, t) \, \mathrm{d}v, \tag{2.13}$$

with the mass density ρ.

Assuming that the mass m is conserved during the motion, the change of mass m in time takes the form

$$\dot{m}(\boldsymbol{x}, t) = \frac{d}{\mathrm{d}t} \int_{\Omega} \rho(\boldsymbol{x}, t) \, \mathrm{d}v. \tag{2.14}$$

The local form of the balance of mass is given by

$$\dot{\rho}(\boldsymbol{x}, t) + \rho(\boldsymbol{x}, t) \mathrm{div} \dot{\boldsymbol{u}} = 0. \tag{2.15}$$

2.2.2 Balance of linear momentum

By Eq. (2.13), the linear momentum is defined as

$$\boldsymbol{P}(t) = \int_{\Omega} \rho \dot{\boldsymbol{u}} \, \mathrm{d}v. \tag{2.16}$$

We assume that a solid body Ω is subjected to a body force (volume force) $\boldsymbol{b}(\boldsymbol{x}, t)$ and the Cauchy traction vector $\boldsymbol{t}(\boldsymbol{x}, \boldsymbol{n}, t)$ on the surface as shown in Fig. 2.2. The change of linear momentum $\boldsymbol{P}$ in time is equal to the sum of all external forces (volume and surface forces) acting on the body

$$\dot{\boldsymbol{P}} = \frac{\mathrm{d}}{\mathrm{d}t} \int_{\Omega} \rho \dot{\boldsymbol{u}} \, \mathrm{d}v = \int_{\Omega} \rho \boldsymbol{b} \, \mathrm{d}v + \int_{\partial\Omega} \boldsymbol{t} \, \mathrm{d}a. \tag{2.17}$$

By means of the divergence theorem, the surface part can be recovered by

$$\int_{\partial\Omega} \boldsymbol{t}\,\mathrm{d}a = \int_{\partial\Omega} \boldsymbol{\sigma}\cdot\boldsymbol{n}\,\mathrm{d}a = \int_{\Omega} \mathrm{div}\boldsymbol{\sigma}\,\mathrm{d}v. \tag{2.18}$$

The local form of the balance of linear momentum can be obtained from Eq. (2.17), i.e.

$$\rho\ddot{\boldsymbol{u}} = \mathrm{div}\boldsymbol{\sigma} + \rho\boldsymbol{b}. \tag{2.19}$$

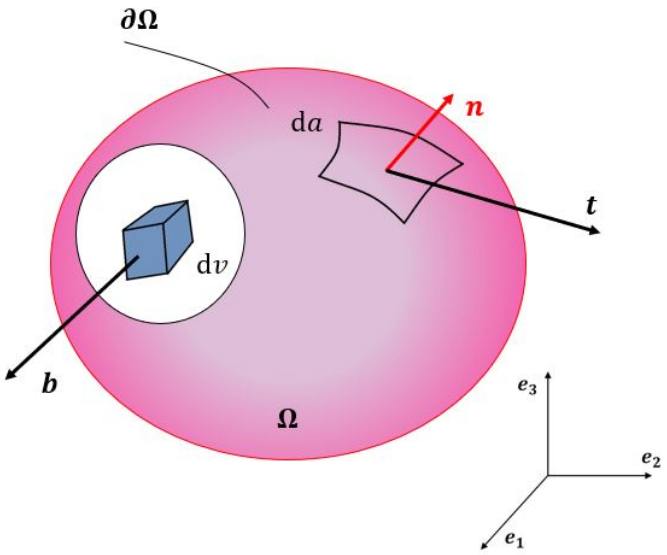

Figure 2.2: Description of the body and surface forces acting on the body.

2.2.3 Balance of angular momentum

The angular momentum $\boldsymbol{J}$ relative to a fixed point $\boldsymbol{x}_0$ is defined as

$$\boldsymbol{J}(t) = \int_{\Omega} (\boldsymbol{x}-\boldsymbol{x}_0)\times\rho\dot{\boldsymbol{u}}\,\mathrm{d}v, \tag{2.20}$$

where $\times$ denotes the cross product of two vectors. According to the balance of angular momentum, the change of angular momentum $\boldsymbol{J}$ in time is equal to the resultant applied moment of the surface and external sources acting on the body, i.e.

$$\dot{\boldsymbol{J}}(t) = \frac{\mathrm{d}}{\mathrm{d}t}\int_\Omega (\boldsymbol{x}-\boldsymbol{x}_0)\times\rho\dot{\boldsymbol{u}}\,\mathrm{d}v = \int_\Omega (\boldsymbol{x}-\boldsymbol{x}_0)\times\boldsymbol{b}\,\mathrm{d}v + \int_{\partial\Omega}(\boldsymbol{x}-\boldsymbol{x}_0)\times\boldsymbol{t}\,\mathrm{d}a. \tag{2.21}$$

A consequence of the balance of angular momentum is the symmetry of the Cauchy stress tensor, i.e.

$$\boldsymbol{\sigma} = \boldsymbol{\sigma}^T. \tag{2.22}$$

For a proof, e.g. see Ref. [244].

2.2.4 First law of thermodynamics

The first law of thermodynamics postulates that the total energy remains constant during any change which may occur in it.

The kinetic energy is given by

$$\mathcal{K} = \int_\Omega \frac{1}{2}\rho\dot{\boldsymbol{u}}\cdot\dot{\boldsymbol{u}}\,\mathrm{d}v. \tag{2.23}$$

Furthermore, the balance of the mechanical energy takes the form

$$\mathcal{P}_{\mathrm{ext}} = \dot{\mathcal{K}} + \mathcal{P}_{\mathrm{int}}, \tag{2.24}$$

and states that the external mechanical power $\mathcal{P}_{\mathrm{ext}}$ is equal to the sum of the stress power $\mathcal{P}_{\mathrm{int}}$ and the rate of kinetic energy $\dot{\mathcal{K}}$. The external mechanical power is given by

$$\mathcal{P}_{\mathrm{ext}} = \int_\Omega \boldsymbol{b}\cdot\dot{\boldsymbol{u}}\,\mathrm{d}v + \int_{\partial\Omega}\boldsymbol{t}\cdot\dot{\boldsymbol{u}}\,\mathrm{d}a. \tag{2.25}$$

The stress power $\mathcal{P}_{\text{int}}$ is conveniently expressed in terms of the stress tensor and the rate of the strain tensor, i.e.

$$\mathcal{P}_{\text{int}} = \int_{\Omega} \boldsymbol{\sigma} : \dot{\boldsymbol{\varepsilon}} \, \mathrm{d}v. \tag{2.26}$$

In order to include the thermal energy contribution, the thermal power $\mathcal{Q}$ is defined as

$$\mathcal{Q} = \int_{\partial\Omega} q \, \mathrm{d}a + \int_{\Omega} r \, \mathrm{d}v, \tag{2.27}$$

with the heat sources r and the heat fluxes q.

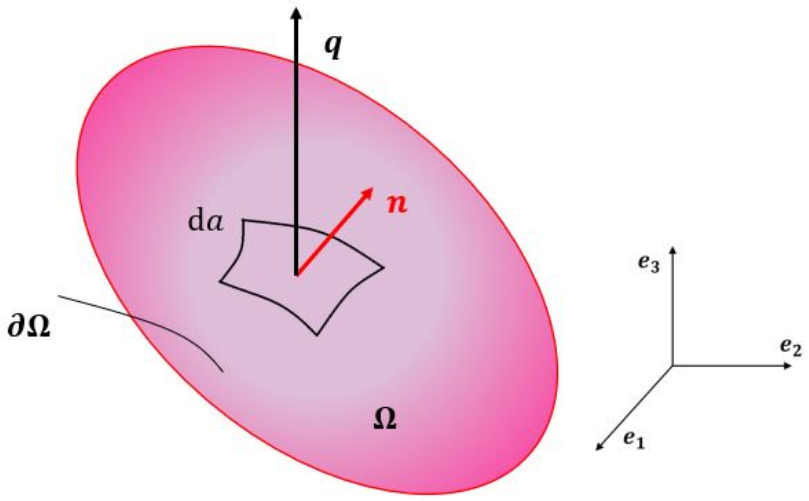

Figure 2.3: Description of the heat flux.

According to the Stoke's heat flux theorem, the scalar fluxes are obtained from the heat flux vectors and outward unit normals (see Fig. 2.3), i.e.

$$q(\boldsymbol{x}, t, \boldsymbol{n}) = -\boldsymbol{q}(\boldsymbol{x}, t) \cdot \boldsymbol{n}. \tag{2.28}$$

The internal energy of a body is given by

$$\mathcal{E} = \int_{\Omega} \rho e \, \mathrm{d}v, \tag{2.29}$$

where e denotes the specific internal energy. The rate of the internal energy $\mathcal{E}$ is equal to the sum of the thermal power $\mathcal{Q}$ and the stress power $\mathcal{P}_{\text{int}}$, i.e.

$$\dot{\mathcal{E}} = \mathcal{P}_{\text{int}} + \mathcal{Q}. \tag{2.30}$$

By substituting (2.24) into (2.30), the rate of the total energy $(\mathcal{E} + \mathcal{K})$ is balanced by the external stress and thermal power

$$\dot{\mathcal{E}} + \dot{\mathcal{K}} = \mathcal{P}_{\text{ext}} + \mathcal{Q}. \tag{2.31}$$

As a consequence, the local form of the first law of thermodynamics is defined as

$$\rho \dot{e} = \boldsymbol{\sigma} : \dot{\boldsymbol{\varepsilon}} + r - \mathrm{div}\boldsymbol{q}. \tag{2.32}$$

2.2.5 Second law of thermodynamics and Helmholtz free energy

Another balance law, which states that the thermodynamic process follows a certain direction of the energy transfer, is known as the second law of thermodynamics. This directional aspect is described by the entropy $\mathcal{S}$ that is defined as a measure of disorder in a body

$$\mathcal{S} = \int_{\Omega} \rho \chi \, \mathrm{d}v, \tag{2.33}$$

with $\chi = \chi(\boldsymbol{x}, t)$ denoting specific entropy per unit mass. According to the balance of entropy, the rate of the entropy $\mathcal{S}$ is equal to the sum of the entropy production Γ

plus the entropy supply $\mathcal{H}$ (due to heat sources and heat fluxes)

$$\dot{\mathcal{S}} = \mathcal{H} + \Gamma, \tag{2.34}$$

where the entropy production Γ is non-negative, i.e.

$$\Gamma = \dot{\mathcal{S}} - \mathcal{H} \geq 0, \tag{2.35}$$

which provides the entropy inequality. Furthermore, the entropy supply $\mathcal{H}$ is given by

$$\mathcal{H} = \int_\Omega \frac{r}{\theta} \, \mathrm{d}v - \int_{\partial\Omega} \frac{\boldsymbol{q}}{\theta} \cdot \boldsymbol{n} \, \mathrm{d}a, \tag{2.36}$$

where $\theta = \theta(\boldsymbol{x}, t) > 0$ presents the thermodynamic (or absolute) temperature.

By substituting Eq. (2.33) and Eq. (2.36) into Eq. (2.35), the second law of thermodynamics can be expressed in form of the Clausius-Duhem inequality

$$\Gamma = \frac{\mathrm{d}}{\mathrm{d}t} \int_\Omega \rho\chi \, \mathrm{d}v + \int_{\partial\Omega} \frac{q}{\theta} \cdot \boldsymbol{n} \, \mathrm{d}a - \int_\Omega \frac{r}{\theta} \, \mathrm{d}v \geq 0, \tag{2.37}$$

which can be rewritten as

$$\Gamma = \int_\Omega \rho\gamma \, \mathrm{d}v \geq 0, \tag{2.38}$$

with the divergence theorem and the local entropy production γ

$$\begin{aligned} \gamma &= \dot{\chi} + \frac{1}{\rho}\mathrm{div}\left(\frac{\boldsymbol{q}}{\theta}\right) - \frac{r}{\rho\theta} = \dot{\chi} + \frac{1}{\rho}\left[\frac{1}{\theta}\mathrm{div}\boldsymbol{q} - \frac{1}{\theta^2}\boldsymbol{q}\cdot\nabla\theta\right] - \frac{r}{\rho\theta} \\ &= \dot{\chi} + \frac{1}{\rho\theta}\left[\mathrm{div}\boldsymbol{q} - r - \frac{1}{\theta}\boldsymbol{q}\cdot\nabla\theta\right] \geq 0. \end{aligned} \tag{2.39}$$

Considering the fact that heat flows from the warmer region to the colder region as

shown in Fig. 2.4, the heat conduction inequality is expressed as

$$-\boldsymbol{q} \cdot \nabla\theta \geq 0, \tag{2.40}$$

where the heat flux $\boldsymbol{q}$ is given by Fourier's law $\boldsymbol{q} = -\boldsymbol{K}\nabla\theta$ with a thermal conductivity tensor $\boldsymbol{K}$.

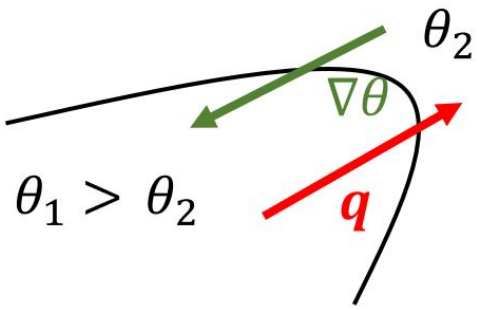

Figure 2.4: Description of the heat transfer.

The Clausius-Planck inequality is defined as

$$\mathcal{D}_{\text{int}} = \frac{1}{\rho}\boldsymbol{\sigma} : \dot{\boldsymbol{\varepsilon}} - (\dot{e} - \theta\dot{\chi}) \geq 0, \tag{2.41}$$

which describes the internal dissipation per unit mass.

Furthermore, the specific (Helmholtz) free energy per unit mass ψ_m is given by

$$\psi_m = e - \theta\chi, \tag{2.42}$$

and its time derivative takes the form

$$\dot{\psi}_m = \dot{e} - \dot{\theta}\chi - \theta\dot{\chi}. \tag{2.43}$$

For phase-field modelling of fracture, it is convenient to relate to volume rather than

mass, i.e.

$$\psi = \rho\psi_m. \tag{2.44}$$

By substituting Eq. (2.44) into Eq. (2.41), the internal dissipation per unit volume can be expressed as

$$\mathcal{D}_{\text{int}} = \boldsymbol{\sigma} : \dot{\boldsymbol{\varepsilon}} - (\dot{\psi} + \rho\dot{\theta}\chi) \geq 0. \tag{2.45}$$

In case of isothermal conditions ($\dot{\theta} = 0$), this inequality is rewritten as

$$\mathcal{D}_{\text{int}} = \boldsymbol{\sigma} : \dot{\boldsymbol{\varepsilon}} - \dot{\psi} \geq 0. \tag{2.46}$$

2.3 Hamilton's principle

Let us consider the Dirichlet boundary conditions on $\partial\Omega_{\boldsymbol{q}} \subseteq \partial\Omega$ and Neumann boundary conditions on $\partial\Omega_{\nabla\boldsymbol{q}} \subseteq \partial\Omega$ in terms of the local fields $\boldsymbol{q}$ and their derivatives $\{\nabla\boldsymbol{q}, \dot{\boldsymbol{q}}\}$. The Lagrangian is defined as

$$L = \int_{\Omega} \mathcal{L}\,\mathrm{d}v = \mathcal{K} - \Pi, \tag{2.47}$$

where $\mathcal{K} = \mathcal{K}(\boldsymbol{q}, \nabla\boldsymbol{q}, \dot{\boldsymbol{q}})$, $\Pi = \Pi(\boldsymbol{q}, \nabla\boldsymbol{q}, \dot{\boldsymbol{q}})$ and $\mathcal{L} = \mathcal{L}(\boldsymbol{q}, \nabla\boldsymbol{q}, \dot{\boldsymbol{q}})$ are defined as the kinetic energy, potential energy and Lagrangian density, respectively.

For arbitrary times $t_1 < t_2$, the Hamilton's principle is expressed as

$$\int_{t_1}^{t_2} (\delta\mathcal{L} + \delta\mathcal{W})\,\mathrm{d}t = 0, \tag{2.48}$$

where $\delta\mathcal{W}$ is defined as the virtual work $\delta\mathcal{W}$ and $\delta\mathcal{L}$ is denoted as the variation of the Lagrange density.

In order to apply the Hamilton's principle for deriving the phase-field evolution equation (for more detail, see Sect. 3.2.3), the appropriate requirements of applica-

tions are presented in the following Lemmas (described in the work by Bedford & Passman [26], pp. 36-37).

Lemma 1 *Let W be an inner product space, and consider a C^0 field $\boldsymbol{h} : \Omega \times [t_1, t_2] \to \mathcal{W}$. If the equation*

$$\int_{t_1}^{t_2} \int_{\Omega} \boldsymbol{h} \cdot \boldsymbol{q} \, \mathrm{d}v \, \mathrm{d}t = 0, \tag{2.49}$$

holds for every C^∞ field $\boldsymbol{q} : \Omega \times [t_1, t_2] \to W$ that vanishes at time t_1, at time t_2, and on $\partial\Omega$, then $\boldsymbol{h} = \boldsymbol{0}$ on $\Omega \times [t_1, t_2]$.

Lemma 2 *Suppose that $\partial\Omega$ consists of complementary regular sub-surfaces $\partial\Omega_q$ and $\partial\Omega_{\nabla q}$. Let W be an inner product space, and consider a function $\boldsymbol{h} : \partial\Omega_{\nabla \boldsymbol{q}} \times [t_1, t_2] \to W$ that is piecewise regular and continuous in time. If the equation*

$$\int_{t_1}^{t_2} \int_{\partial\Omega_{\nabla \boldsymbol{q}}} \boldsymbol{h} \cdot \boldsymbol{q} \, \mathrm{d}a \, \mathrm{d}t = 0 \tag{2.50}$$

holds for every C^∞ field $\boldsymbol{q} : \Omega \times [t_1, t_2] \to W$ that vanishes at time t_1, at time t_2, and on $\partial\Omega_{\boldsymbol{q}}$, then $\boldsymbol{h} = \boldsymbol{0}$ on $\partial\Omega_{\nabla \boldsymbol{q}} \times [t_1, t_2]$.

3

Phase-field models for brittle fracture

This chapter first describes the Griffith's criterion of brittle fracture in Sect. 3.1. Next, the phase-field models for isotropic and anisotropic fracture are presented in Sect. 3.2 and Sect. 3.3, respectively. Furthermore, initial values and boundary conditions for phase-field modelling of fracture are briefly discussed in Sect. 3.4. Finally, three commonly used methods for the irreversibility of the crack phase-field are introduced in Sect. 3.5.

3.1 Linear elastic fracture mechanics: Griffith's criterion

Consider the first law of thermodynamics

$$\dot{\mathcal{E}} + \dot{\mathcal{K}} = \mathcal{P}_{\text{ext}} + \mathcal{Q}, \tag{3.1}$$

where $\dot{\mathcal{E}}$, $\dot{\mathcal{K}}$, $\mathcal{P}_{\text{ext}}$, and $\mathcal{Q}$ are defined as the rate of internal energy, the rate of kinetic energy, the external stress power and the thermal power, respectively. The fracture surface energy ψ_s is the critical energy required to generate the new crack surfaces during the fracturing processes, which takes the form

$$\psi_s = \mathscr{G}_c A, \tag{3.2}$$

with A denoting the area of the crack.

The Griffith's criterion of brittle fracture introduces a new term in Eq. (3.1), i.e.

$$\dot{\mathcal{E}} + \dot{\mathcal{K}} + \dot{\psi}_s = \mathcal{P}_{\text{ext}} + \mathcal{Q}. \tag{3.3}$$

If we assume that the contribution of kinetic energy is negligible for the quasi static fracturing process, Eq. (3.3) can be rewritten as

$$\dot{\psi}_s = \mathcal{P}_{\text{ext}} + \mathcal{Q} - \dot{\mathcal{E}}. \tag{3.4}$$

Considering that the internal energy $\mathcal{E}$, the rate of work associated to the external forces $\mathcal{P}_{\text{ext}}$, and thermal power $\mathcal{Q}$ are expressed in terms of potentials: $\Pi_{\text{int}} = \mathcal{E}$, $\frac{\mathrm{d}\Pi_{\text{ext}}^{\text{mech}}}{\mathrm{d}t} = -\mathcal{P}_{\text{ext}}$ and $\frac{\mathrm{d}\Pi_{\text{ext}}^{\text{ther}}}{\mathrm{d}t} = -\mathcal{Q}$, the total potential is defined as

$$\Pi = \Pi_{\text{int}} + \Pi_{\text{ext}}^{\text{mech}} + \Pi_{\text{ext}}^{\text{ther}}. \tag{3.5}$$

Using these definitions, Eq. (3.4) can be rewritten as

$$\frac{\mathrm{d}\Pi}{\mathrm{d}t} + \frac{\psi_s}{\mathrm{d}t} = 0. \tag{3.6}$$

If the crack surface is assumed to be infinitesimal, Eq. (3.6) can be extended to

$$\left[\frac{\mathrm{d}\Pi}{\mathrm{d}A} + \frac{\psi_s}{\mathrm{d}A}\right] \frac{\mathrm{d}A}{\mathrm{d}t} = 0, \tag{3.7}$$

which can be further simplified to

$$\left(\mathscr{G}_c - \mathscr{G}\right) \dot{A} = 0, \tag{3.8}$$

with the energy release rate $\mathscr{G} = -\frac{\mathrm{d}\Pi}{\mathrm{d}A}$ and the critical energy release rate $\mathscr{G}_c$ (or fracture toughness).

The Griffth's criterion of brittle fracture can be obtained from Eq. (3.8), i.e.

$$\mathscr{G} = \mathscr{G}_c, \tag{3.9}$$

which states that the dissipation of potential energy that occurs during the fracturing process must be greater than or equal the increase in surface energy due to the creation of new crack surfaces.

Nevertheless, stress intensity factors only arise from the solution of fracture problems in homogeneous isotropic linear elastic materials. The energy release rate can be calculated by the stress intensity factors (K_I, K_{II} and K_{III}), i.e.

$$\mathscr{G} = \frac{K_I^2 + K_{II}^2}{E} + \frac{K_{III}^2}{2\mu}, \tag{3.10}$$

with the Young's modulus E and the shear modulus μ.

3.2 Phase-field modelling of brittle fracture in isotropic materials

3.2.1 Fracture resistance in isotropic materials

Consider an isotropic linear elastic homogeneous bar with a cross-section Γ of infinite length with a crack at the axial position $x = 0$, as shown in Fig. 3.1a. In the sharp crack topology, an order parameter $s(x) \in [0, 1]$ is described by

$$s(x) := \begin{cases} 0 & \text{for } x = 0 \\ \\ 1 & \text{otherwise} \end{cases}, \tag{3.11}$$

which has a value of 0 in a totally damaged region and 1 at undamaged material points as plotted in Fig. 3.1b.

In the phase-field method, the sharp crack topology is replaced by a diffuse crack (see Fig. 3.1c), which can be approximated using a standard exponential function

$$s(x) = 1 - e^{-|x|/2\kappa}, \tag{3.12}$$

where κ is defined as the crack width. The Eq. (3.12) satisfies the ordinary differential equation

$$s - 4\kappa^2 s'' - 1 = 0 \ , \tag{3.13}$$

with the boundary conditions: $s(0) = 0$ and $s(\pm\infty) = 1$.

$$I(s) = \frac{1}{2} \int_\Omega \left\{ (1 - s)^2 + 4\kappa^2 s'^2 \right\} \, \mathrm{d}x, \tag{3.14}$$

which represents the quadratic functional of phase-field second order. The second order Taylor expansion of the functional for the crack surface Γ_κ can be expressed in

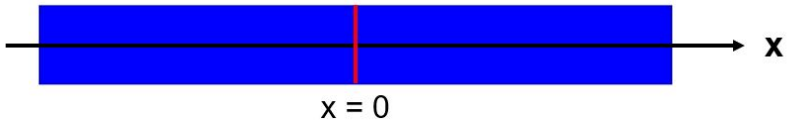

(a) Cracked 1D bar

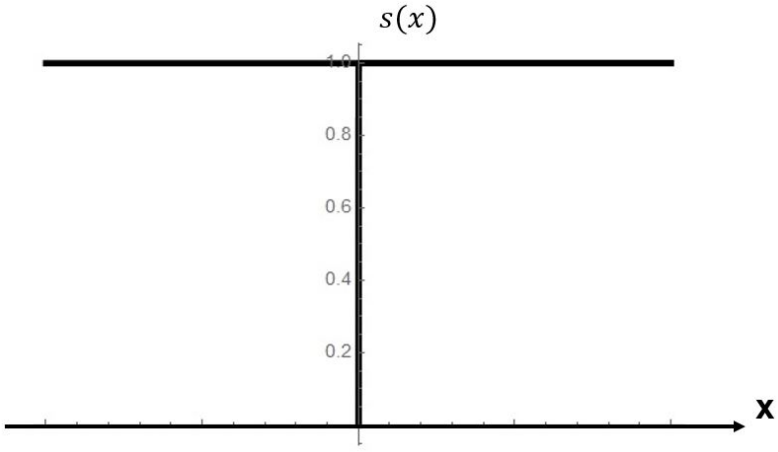

(b) Sharp crack

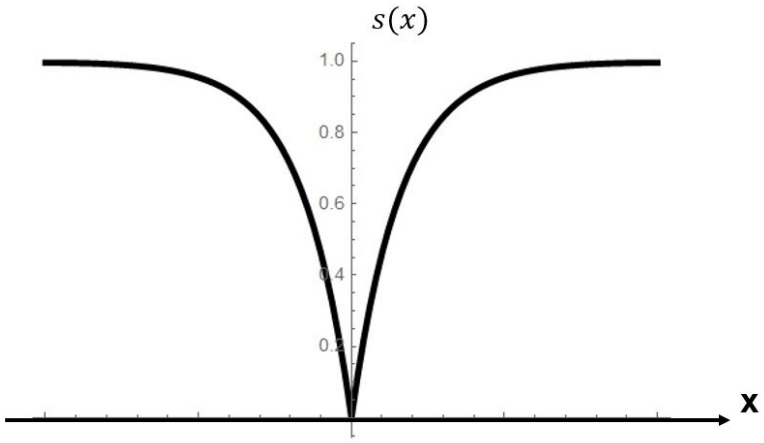

(c) Diffuse crack

Figure 3.1: (a) 1D bar with a crack at $x = 0$. (b) Sharp crack topology at $x = 0$. (c) Diffuse crack topology at $x = 0$.

the form

$$\Gamma_\kappa(s) := \frac{1}{2\kappa} I(s) = \frac{1}{4\kappa} \int_\Omega \left\{ (1-s)^2 + 4\kappa^2 s'^2 \right\} \, \mathrm{d}x, \tag{3.15}$$

under the assumption of $\mathrm{d}v = \Gamma \mathrm{d}x$.

In multidimensional cases $\Omega \subset \mathbb{E}^{n\in[2,3]}$, the crack $\Gamma_\kappa(s)$ is defined as

$$\Gamma_\kappa(s) = \int_\Omega \gamma(s, \nabla s) \, \mathrm{d}v, \tag{3.16}$$

with γ denoting the crack density function per unit volume

$$\gamma(s, \nabla s) = \frac{(1-s)^2}{4\kappa} + \kappa |\nabla s|^2 \, . \tag{3.17}$$

The Euler-Lagrange equation associated with the variational principle for fracture is given by

$$s - 4\kappa^2 \Delta s - 1 = 0 \;\; \text{in} \;\; \Omega \;\; \text{and} \;\; \nabla s \cdot \mathbf{n} = 0 \;\; \text{on} \; \partial\Omega, \tag{3.18}$$

in which Δs is denoted as the Laplacian operation of the phase-field variable s and $\mathbf{n}$ is defined as the outward normal to $\partial\Omega$. A two-dimensional illustration of the phase-field modelling of fracture is depicted in Fig. 3.2.

3.2.2 Phase-field modelling of crack evolution in isotropic materials

Consider a linear elastic, homogeneous and isotropic material domain Ω with an initial crack Γ, as shown in Fig. 3.2. The total strain tensor $\boldsymbol{\varepsilon}$ consists of an elastic part $\boldsymbol{\varepsilon}_e$ and a thermal part $\boldsymbol{\varepsilon}_\theta$

$$\boldsymbol{\varepsilon} = \boldsymbol{\varepsilon}_e + \boldsymbol{\varepsilon}_\theta, \tag{3.19}$$

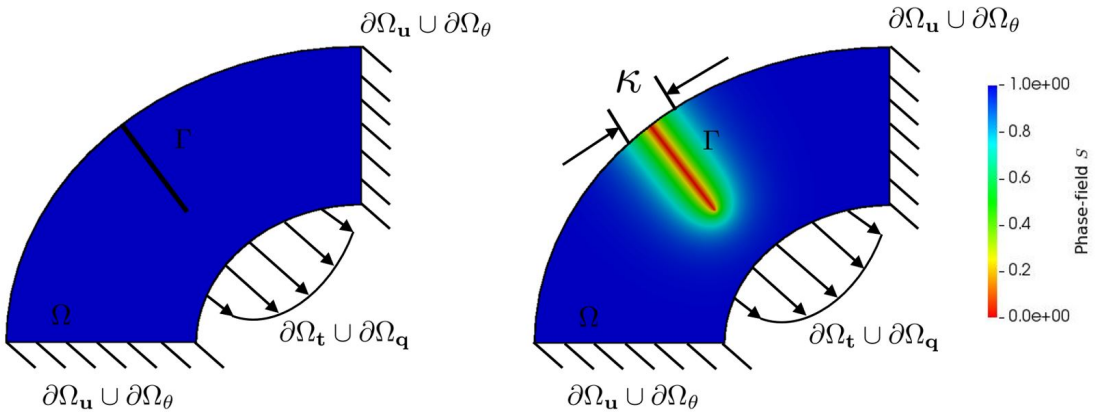

Figure 3.2: Sharp crack (left) of a solid medium, and a diffuse crack presented by a phase-field (right).

where the thermal strain $\boldsymbol{\varepsilon}_\theta$ is generally proportional to the temperature change $\Delta\theta$

$$\boldsymbol{\varepsilon}_\theta = \alpha_T \Delta\theta \mathbf{1}, \tag{3.20}$$

with $\alpha_T > 0$ denoting the coefficient of thermal expansion.

By Eq. (3.19) and Eq. (3.20), the elastic strain energy density in isotropic materials is given by

$$\psi_e(\boldsymbol{u}) = \frac{1}{2}\boldsymbol{\varepsilon}_e : \mathbb{C} : \boldsymbol{\varepsilon}_e, \tag{3.21}$$

with the isotropic fourth-order elastic stiffness tensor $\mathbb{C}$

$$\mathbb{C} = \lambda \mathbf{1} \otimes \mathbf{1} + 2\mu\mathbb{I}, \tag{3.22}$$

where $\mathbb{I}$ is denoted as the fourth-order identity tensor and λ is defined as the Lamé's first parameter.

In order to prevent crack growth under compressive loadings, a decomposition of the elastic strain energy density is usually considered, which is obtained by splitting

the elastic strain energy density into a tension part ψ_e^+ coupled with crack evolution and a compression part ψ_e^- unassociated with fracturing processes. This implies the following modification of the elastic strain energy density

$$\psi_e = \psi_e^+ + \psi_e^-. \tag{3.23}$$

Several studies have been conducted to provide an appropriate formulation for ψ_e^+. Three popular phase-field models are: (a) the one of Amor et al. [13] hereby noted by "volumetric/deviatoric split" and (b) that of Miehe et al. [169] denoted here "spectral split" as well as (c) the one of Ambati et al. [11] expressed by "hybrid model". The main concepts of these three schemes are reviewed in Sect. 3.2.4.

3.2.3 Governing equations for the evolution of the crack phase-field in isotropic materials

According to Ref. [224], the Lagrangian L for fracture problems in isotropic materials is defined as

$$\begin{aligned} L &= \int_\Omega \mathcal{L}(\nabla \boldsymbol{u}, s, \nabla s)\,\mathrm{d}v + \int_{\partial\Omega_t} \boldsymbol{t}\cdot\boldsymbol{u}\,\mathrm{d}a \\ &= -\int_\Omega \left[g(s)\,\psi_e^+ + \psi_e^- + \mathscr{G}_c \left[\frac{(1-s)^2}{4\kappa} + \kappa |\nabla s|^2 \right] \right] \mathrm{d}v \\ &\quad + \int_{\partial\Omega_t} \boldsymbol{t}\cdot\boldsymbol{u}\,\mathrm{d}a, \end{aligned} \tag{3.24}$$

when body forces are neglected. In Eq. (3.24) the degradation function $g(s) = s^2 + \eta$ is introduced to reduce the material stiffness due to the damage evolution, and the phase-field s varies smoothly from 1 (intact material) to 0 (broken material). A small positive dimensionless parameter $0 < \eta \ll 1$ is used to ensure a numerically well-conditioned system for a totally damaged state ($s = 0$). The effects of quadratic,

quartic and cubic degradation functions have been investigated by Kuhn et al. [137].

For an arbitrary time interval $[t_1, t_2]$, the displacements $\boldsymbol{u}$ and the phase-field s must fulfill the Hamilton's principle

$$\int_{t_1}^{t_2} \int_{\Omega} \delta\mathcal{L} \, \mathrm{d}v \, \mathrm{d}t + \int_{t_1}^{t_2} \int_{\partial\Omega_{\boldsymbol{t}}} \boldsymbol{t} \cdot \delta\boldsymbol{u} \, \mathrm{d}a \, \mathrm{d}t = 0, \tag{3.25}$$

where $\delta\mathcal{L}$ is defined as the variation of the Lagrange density

$$\delta\mathcal{L} = \frac{\partial\mathcal{L}}{\partial\nabla\boldsymbol{u}} : \nabla\delta\boldsymbol{u} + \frac{\partial\mathcal{L}}{\partial s}\delta s + \frac{\partial\mathcal{L}}{\partial\nabla_S} \cdot \nabla\delta s, \tag{3.26}$$

with

$$\begin{aligned} \tfrac{\partial\mathcal{L}}{\partial\nabla\boldsymbol{u}} : \nabla\,\delta\boldsymbol{u} &= -\mathrm{div}\left(\tfrac{\partial\mathcal{L}}{\partial\nabla\boldsymbol{u}}\right) \cdot \delta\boldsymbol{u} + \mathrm{div}\left(\left(\tfrac{\partial\mathcal{L}}{\partial\nabla\boldsymbol{u}}\right)^T \delta\boldsymbol{u}\right), \\ \tfrac{\partial\mathcal{L}}{\partial\nabla_S} \cdot \nabla\,\delta s &= -\mathrm{div}\left(\tfrac{\partial\mathcal{L}}{\partial\nabla s}\right) \delta s + \mathrm{div}\left(\tfrac{\partial\mathcal{L}}{\partial\nabla s}\,\delta s\right). \end{aligned} \tag{3.27}$$

By using the divergence theorem [224], the first term in Eq. (3.25) can be expressed as

$$\begin{aligned} \int_{t_1}^{t_2} \int_{\Omega} \delta\mathcal{L} \, \mathrm{d}v \, \mathrm{d}t = &\int_{t_1}^{t_2} \int_{\Omega} \left[-\mathrm{div}\left(\frac{\partial\mathcal{L}}{\partial\nabla\boldsymbol{u}}\right)\right] \cdot \delta\boldsymbol{u} \, \mathrm{d}v \, \mathrm{d}t \\ &+ \int_{t_1}^{t_2} \int_{\Omega} \left[\frac{\partial\mathcal{L}}{\partial s} - \mathrm{div}\left(\frac{\partial\mathcal{L}}{\partial\nabla s}\right)\right] \delta s \, \mathrm{d}v \, \mathrm{d}t \\ &+ \int_{t_1}^{t_2} \int_{\partial\Omega} \left[\left(\frac{\partial\mathcal{L}}{\partial\nabla\boldsymbol{u}}\right)^T \boldsymbol{n}\right] \cdot \delta\boldsymbol{u} \, \mathrm{d}a \, \mathrm{d}t \\ &+ \int_{t_1}^{t_2} \int_{\partial\Omega} \left[\frac{\partial\mathcal{L}}{\partial\nabla s} \cdot \boldsymbol{n}\right] \delta s \, \mathrm{d}a \, \mathrm{d}t. \end{aligned} \tag{3.28}$$

According to the Lemma 1 and Lemma 2, the variation of the Lagrangian L with respect to the fields $\{\boldsymbol{u}, s\}$, considering the arbitrary variations $\delta\boldsymbol{u}$ and δs, yields the Euler-Lagrange equations as follows

$$\mathrm{div}\left(\frac{\partial\mathcal{L}}{\partial\nabla\boldsymbol{u}}\right) = \boldsymbol{0}, \quad \text{in } \Omega \tag{3.29}$$

$$\left(\frac{\partial \mathcal{L}}{\partial \nabla \boldsymbol{u}}\right)^T \boldsymbol{n} + \boldsymbol{t} = 0, \quad \text{on } \partial\Omega_{\boldsymbol{t}} \tag{3.30}$$

$$\frac{\partial \mathcal{L}}{\partial s} - \text{div}\left(\frac{\partial \mathcal{L}}{\partial \nabla s}\right) = 0, \quad \text{in } \Omega \tag{3.31}$$

and

$$\frac{\partial \mathcal{L}}{\partial \nabla s} \cdot \boldsymbol{n} = 0. \quad \text{on } \partial\Omega_s \tag{3.32}$$

Now we recall the effective stress tensor $\boldsymbol{\sigma}$

$$\boldsymbol{\sigma} = (s^2 + \eta) \underbrace{\frac{\partial \psi_e^+}{\partial \boldsymbol{\varepsilon}_e}}_{\boldsymbol{\sigma}^+} + \underbrace{\frac{\partial \psi_e^-}{\partial \boldsymbol{\varepsilon}_e}}_{\boldsymbol{\sigma}^-}. \tag{3.33}$$

Evaluation of Eq. (3.29) and Eq. (3.31) provides the governing equations of the displacements and the phase-field,

$$\begin{cases} \text{div}\boldsymbol{\sigma} = \boldsymbol{0}, & \text{in } \Omega \times [0,T] \\ 2s\psi_{\text{e}}^+ - \mathscr{G}_c \left[2\kappa\Delta s + \dfrac{1-s}{2\kappa}\right] = 0. & \text{in } \Omega \times [0,T] \end{cases} \tag{3.34}$$

In addition, evaluations of Eq. (3.30) and Eq. (3.32) provide the Neumann boundary conditions of the displacements and the phase-field,

$$\begin{cases} \boldsymbol{\sigma} \cdot \boldsymbol{n} = \boldsymbol{t}, & \text{on } \partial\Omega_{\boldsymbol{t}} \times [0,T] \\ \nabla s \cdot \mathbf{n} = 0. & \text{on } \partial\Omega_{\text{s}} \times [0,T] \end{cases} \tag{3.35}$$

3.2.4 Elastic strain energy density decompositions in phase-field fracture theories

In this subsection we review four commonly used phase-field models for brittle fracture. These models mainly differ in their choice of the positive part of the elastic

strain energy density.

Isotropic model

We first consider the isotropic phase-field model proposed by Bourdin et al. [41]. In this model, no difference is made between the fracture behavior in tension and compression. Thus

$$\psi(\boldsymbol{\varepsilon}_e, s) = (s^2 + \eta)\psi_e(\boldsymbol{\varepsilon}_e) = (s^2 + \eta)\left[\frac{\lambda}{2}(\mathrm{tr}(\boldsymbol{\varepsilon}_e))^2 + \mu \mathrm{tr}(\boldsymbol{\varepsilon}_e^2)\right], \tag{3.36}$$

and

$$\boldsymbol{\sigma}(\boldsymbol{\varepsilon}_e, s) = (s^2 + \eta)\frac{\partial \psi_e(\boldsymbol{\varepsilon}_e)}{\partial \boldsymbol{\varepsilon}_e} = (s^2 + \eta)\left[\lambda(\mathrm{tr}(\boldsymbol{\varepsilon}_e))\mathbf{1} + 2\mu\boldsymbol{\varepsilon}_e\right]. \tag{3.37}$$

These yield

$$\mathbb{C}(\boldsymbol{\varepsilon}_e, s) = (s^2 + \eta)\frac{\partial^2 \psi_e(\boldsymbol{\varepsilon}_e)}{\partial \boldsymbol{\varepsilon}_e^2} = (s^2 + \eta)\left[\lambda \mathbf{1} \otimes \mathbf{1} + 2\mu\mathbb{I}\right]. \tag{3.38}$$

Spectral split

In order to prevent damage from crack developing under compressive loadings, a spectral split was herein proposed by Miehe et al. [169]. In this case, a spectral decomposition of the elastic strain tensor considers

$$\boldsymbol{\varepsilon}_e = \sum_{a=1}^{3} \langle \boldsymbol{\varepsilon}_e^a \rangle \, \boldsymbol{n}_a \otimes \boldsymbol{n}_a, \tag{3.39}$$

where $\boldsymbol{\varepsilon}_e^a$ and $\boldsymbol{n}_a$ are the principal elastic strains and principal elastic strain directions (with $a = 1, 2, 3$).

Further on, the elastic strain tensor is split into a positive part $\boldsymbol{\varepsilon}_e^+$ and a negative

part $\boldsymbol{\varepsilon}_e^-$, i.e.

$$\boldsymbol{\varepsilon}_e = \boldsymbol{\varepsilon}_e^+ + \boldsymbol{\varepsilon}_e^-, \tag{3.40}$$

with

$$\boldsymbol{\varepsilon}_e^+ = \sum_{a=1}^{3} \langle \varepsilon_e^a \rangle_+ \, \boldsymbol{n}_a \otimes \boldsymbol{n}_a, \tag{3.41}$$

and

$$\boldsymbol{\varepsilon}_e^- = \sum_{a=1}^{3} \langle \varepsilon_e^a \rangle_- \, \boldsymbol{n}_a \otimes \boldsymbol{n}_a, \tag{3.42}$$

in terms of the Macaulay brackets $\langle \cdot \rangle_+ = (\cdot + |\cdot|)/2$ and $\langle \cdot \rangle_- = (\cdot - |\cdot|)/2$, respectively.

In Ref. [169], the additive decomposition of ψ based on tension-compression spectral split is defined as

$$\psi(\boldsymbol{\varepsilon}_e, s) = (s^2 + \eta)\psi_e^+(\boldsymbol{\varepsilon}_e) + \psi_e^-(\boldsymbol{\varepsilon}_e), \tag{3.43}$$

with

$$\psi_e^+(\boldsymbol{\varepsilon}_e) = \frac{\lambda}{2}\langle \mathrm{tr}(\boldsymbol{\varepsilon}_e) \rangle_+^2 + \mu(\boldsymbol{\varepsilon}_e^+ : \boldsymbol{\varepsilon}_e^+), \tag{3.44}$$

and

$$\psi_e^-(\boldsymbol{\varepsilon}_e) = \frac{\lambda}{2}\langle \mathrm{tr}(\boldsymbol{\varepsilon}_e) \rangle_-^2 + \mu(\boldsymbol{\varepsilon}_e^- : \boldsymbol{\varepsilon}_e^-), \tag{3.45}$$

wherein only the positive part ψ_e^+ due to tension is considered in the phase-field evolution equation (Eq. (3.34)).

The effective stress tensor $\boldsymbol{\sigma}$ is calculated by

$$\boldsymbol{\sigma}(\boldsymbol{\varepsilon}_e, s) = (s^2 + \eta)\frac{\partial \psi_e^+(\boldsymbol{\varepsilon}_e)}{\partial \boldsymbol{\varepsilon}_e} + \frac{\partial \psi_e^-(\boldsymbol{\varepsilon}_e)}{\partial \boldsymbol{\varepsilon}_e} = (s^2 + \eta)\boldsymbol{\sigma}_e^+(\boldsymbol{\varepsilon}_e) + \boldsymbol{\sigma}_e^-(\boldsymbol{\varepsilon}_e), \tag{3.46}$$

with

$$\boldsymbol{\sigma}_e^+(\boldsymbol{\varepsilon}_e) = \lambda\langle \mathrm{tr}(\boldsymbol{\varepsilon}_e) \rangle_+ \mathbf{1} + 2\mu\boldsymbol{\varepsilon}_e^+, \tag{3.47}$$

and

$$\boldsymbol{\sigma}_e^-(\boldsymbol{\varepsilon}_e) = \lambda\langle \mathrm{tr}(\boldsymbol{\varepsilon}_e)\rangle_- \mathbf{1} + 2\mu\boldsymbol{\varepsilon}_e^-. \tag{3.48}$$

The resulting stiffness tensor is expressed as

$$\begin{aligned}\mathbb{C}(\boldsymbol{\varepsilon}_e, s) &= (s^2+\eta)\mathbb{C}^+(\boldsymbol{\varepsilon}_e) + \mathbb{C}^-(\boldsymbol{\varepsilon}_e) \\ &= (s^2+\eta)\left[\lambda\,\mathrm{sign}^+(\mathrm{tr}(\boldsymbol{\varepsilon}_e))\mathbf{I}\otimes\mathbf{I} + 2\mu\mathbb{P}^+\right] + \lambda\,\mathrm{sign}^-(\mathrm{tr}(\boldsymbol{\varepsilon}_e))\mathbf{I}\otimes\mathbf{I} + 2\mu\mathbb{P}^-,\end{aligned} \tag{3.49}$$

with the signum functions

$$\begin{aligned} x \geq 0 &\Rightarrow \mathrm{sign}^+(x) = 1,\ \mathrm{sign}^-(x) = 0, \\ x < 0 &\Rightarrow \mathrm{sign}^+(x) = 0,\ \mathrm{sign}^-(x) = 1. \end{aligned} \tag{3.50}$$

In Eq.(3.49), $\mathbb{P}^+$ and $\mathbb{P}^-$ are the mappings of the elastic strains onto their positive and negative elastic parts, i.e.

$$\mathbb{P}^+ = \partial_{\boldsymbol{\varepsilon}_e}\left[\boldsymbol{\varepsilon}_e^+(\boldsymbol{\varepsilon}_e)\right] \quad \text{and} \quad \mathbb{P}^- = \partial_{\boldsymbol{\varepsilon}_e}\left[\boldsymbol{\varepsilon}_e^-(\boldsymbol{\varepsilon}_e)\right]. \tag{3.51}$$

These projection tensors can be computed according to the algorithms outlined in Refs. [165, 167].

Volumetric/deviatoric split

Alternatively, Amor et al. [13] introduced a volumetric/deviatoric split model which can distinguish between the fracture behavior in tension and compression. Thus

$$\psi(\boldsymbol{\varepsilon}_e, s) = (s^2+\eta)\psi_e^+(\boldsymbol{\varepsilon}_e) + \psi_e^-(\boldsymbol{\varepsilon}_e), \tag{3.52}$$

where

$$\psi_e^+(\boldsymbol{\varepsilon}_e) = \frac{K}{2}\langle \mathrm{tr}(\boldsymbol{\varepsilon}_e)\rangle_+^2 + \mu(\boldsymbol{\varepsilon}_e^{\mathrm{dev}} : \boldsymbol{\varepsilon}_e^{\mathrm{dev}}), \tag{3.53}$$

and

$$\psi_e^-(\boldsymbol{\varepsilon}_e) = \frac{K}{2}\langle \mathrm{tr}(\boldsymbol{\varepsilon}_e)\rangle_-^2, \tag{3.54}$$

with the bulk modulus $K = \lambda + 2/3\mu$ and the deviatoric strain tensor $\boldsymbol{\varepsilon}_e^{\mathrm{dev}} := \boldsymbol{\varepsilon}_e - \frac{1}{3}\mathrm{tr}(\boldsymbol{\varepsilon}_e)\mathbf{1}$.

Hence, the effective stress tensor $\boldsymbol{\sigma}$ and the stiffness tensor $\mathbb{C}$ are given by

$$\begin{aligned}\boldsymbol{\sigma}(\boldsymbol{\varepsilon}_e, s) &= (s^2+\eta)(K\langle \mathrm{tr}(\boldsymbol{\varepsilon}_e)\rangle_+ \mathbf{1} + 2\mu\,\boldsymbol{\varepsilon}_e^{\mathrm{dev}}) + K\langle \mathrm{tr}(\boldsymbol{\varepsilon}_e)\rangle_- \mathbf{1} \\ &= (s^2+\eta)\boldsymbol{\sigma}_e^+(\boldsymbol{\varepsilon}_e) + \boldsymbol{\sigma}_e^-(\boldsymbol{\varepsilon}_e),\end{aligned} \tag{3.55}$$

and

$$\mathbb{C}(\boldsymbol{\varepsilon}_e, s) = \Big(s^2+\eta\Big)\left[K\mathrm{sign}^+(\mathrm{tr}(\boldsymbol{\varepsilon}_e))\mathbf{1}\otimes\mathbf{1} + 2\mu\left[\mathbb{I} - \frac{1}{3}\mathbf{1}\otimes\mathbf{1}\right]\right] + K\mathrm{sign}^-(\mathrm{tr}(\boldsymbol{\varepsilon}_e))\mathbf{1}\otimes\mathbf{1}, \tag{3.56}$$

respectively.

Hybrid model

To prevent unrealistic crack evolution under compressive loadings, the numerically anisotropic formulations (Amor et al. [13]; Miehe et al. [169]) can be applied. However, in this case the stress-strain relation is no longer linear due to the split of the elastic strains, inevitably increasing the computational cost.

To overcome the limitation of the numerically anisotropic splits, the so-called hybrid model (Ambati et al. [11]; Doan et al. [69]) can be used, in which the stress-strain relation is still associated with the isotropic strain energy density (Eq. (3.2.4)), whereas the phase-field evolution equation is associated with a different one, i.e. the positive part of the elastic strain energy density ψ_e^+. In [11], the positive part of the elastic strain energy density remains the same as the volumetric/deviatoric split (Eq. (3.2.4)).

In [69], the positive part of the elastic strain energy density from the spectral split formulation (Eq. (3.2.4)) is used. In the following sections, the hybrid formulation in [69] is applied for phase-field simulations.

The positive and negative parts of the elastic strain energy density in the hybrid model are given by

$$\psi_e^+(\boldsymbol{\varepsilon}_e) = \frac{\lambda}{2}\langle \mathrm{tr}(\boldsymbol{\varepsilon}_e)\rangle_+^2 + \mu(\boldsymbol{\varepsilon}_e^+ : \boldsymbol{\varepsilon}_e^+), \tag{3.57}$$

and

$$\psi_e^-(\boldsymbol{\varepsilon}_e) = \frac{\lambda}{2}\langle \mathrm{tr}(\boldsymbol{\varepsilon}_e)\rangle_-^2 + \mu(\boldsymbol{\varepsilon}_e^- : \boldsymbol{\varepsilon}_e^-), \tag{3.58}$$

respectively.

Moreover, the effective stress tensor $\boldsymbol{\sigma}$ is defined as

$$\boldsymbol{\sigma}(\boldsymbol{\varepsilon}_e, s) = (s^2 + \eta)\Big[\lambda(\mathrm{tr}(\boldsymbol{\varepsilon}_e))\mathbf{1} + 2\mu\boldsymbol{\varepsilon}_e\Big], \tag{3.59}$$

and the stiffness tensor $\mathbb{C}$ is expressed as

$$\mathbb{C}(\boldsymbol{\varepsilon}_e, s) = (s^2 + \eta)\Big[\lambda\mathbf{1}\otimes\mathbf{1} + 2\mu\mathbb{I}\Big]. \tag{3.60}$$

Remark 1 *Storm et al. [246] emphasized that the crack closure effect is not considered in the hybrid model [11].*

Remark 2 *Wu [274] indicated that the hybrid formulation [11] is no longer variationally consistent, whereas such a variationally inconsistency violates the dissipation inequality.*

3.2.5 Governing equations for heat transfer in isotropic materials

Considering that the volumetric heat generation per unit volume per unit time is neglected, the transient heat conduction equation for an isotropic material is given by

$$\rho c_p \dot{\theta} + \mathrm{div}\boldsymbol{q} = 0, \tag{3.61}$$

with the mass density ρ and the specific heat capacity c_p. An isotropic Fourier's law is applied to describe the constitutive relation between the heat flux $\boldsymbol{q}$ and the temperature field θ, i.e.

$$\boldsymbol{q} = -k\left(\zeta\left(s^2 - 1\right) + 1\right)\nabla\theta, \tag{3.62}$$

where k is denoted as the coefficient of isotropic thermal conductivity, and $\zeta \in [0, 1]$ is the numerical parameter that considers the hindering effect of cracks on heat transfer [223]. In case of $\zeta = 0$, the crack phase-field is conducting. On the contrary, a thermally isolating crack is considered in case of $\zeta = 1$.

On the surface of a body, the following thermal boundary conditions have to be satisfied,

$$\begin{cases} \theta = \theta_s, & \text{on } \partial\Omega_\theta \times [0, T] \\ -\boldsymbol{q} \cdot \boldsymbol{n} = \boldsymbol{q}_s, & \text{on } \partial\Omega_{\boldsymbol{q}} \times [0, T] \end{cases} \tag{3.63}$$

where θ_s is denoted as the specified temperature on $\partial\Omega_\theta$, and $\boldsymbol{q}_s$ is defined as the prescribed heat flux on $\partial\Omega_{\boldsymbol{q}}$.

3.3 Phase-field modelling of brittle fracture in anisotropic materials

3.3.1 Fracture resistance in anisotropic materials

In the phase-field model for anisotropic fracture, a second order structural tensor $\boldsymbol{\omega}$, as an additional material parameter for the direction dependent fracture toughness, was introduced by Dal et al. [60]

$$\boldsymbol{\omega} = \mathbf{1} + \beta\, \mathbf{M} \otimes \mathbf{M}, \tag{3.64}$$

with

$$\mathbf{M} = \begin{bmatrix} \cos(\alpha) \\ \sin(\alpha) \end{bmatrix}, \tag{3.65}$$

in which $\mathbf{M}$ represents the unit vector along the material orientation. An illustration for the vector $\mathbf{M}$ and the material orientation α is shown in Fig. 3.3. $\beta \gg 0$ is denoted as a penalty factor which mainly penalizes the direction of crack evolution on planes along the material orientation α. In case of isotropic fracture, β must be chosen as 0.

For application in phase-field modelling of anisotropic fracture, various values β have been chosen for the restriction of crack orientation, such as $\beta = 100$ in Ref. [55] and $\beta = 50$ in Ref. [256], as well as $\beta = 20$ in Refs. [113, 152, 183, 184]. Why β is chosen like that has not been discussed by the authors, but it is obvious that a proper chosen value of β has to accurately reflect the anisotropic fracture behavior. Therefore, the effects of the penalty factor β on the results are investigated in Sect. 5.1.

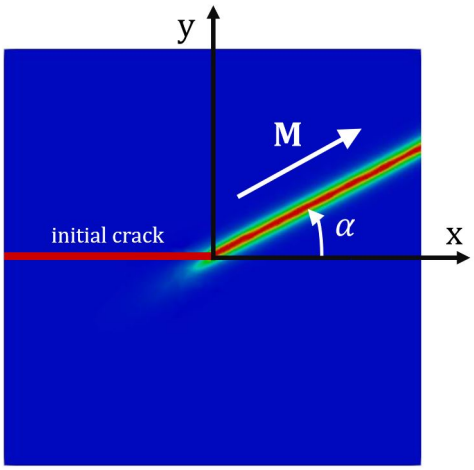

Figure 3.3: Anisotropic phase-field approach.

In two-dimensional case, the global components of the coefficients of the second

order structural tensor $\boldsymbol{\omega}$ are expressed as

$$\boldsymbol{\omega} = \begin{bmatrix} 1+\beta\cos^2(\alpha) & \beta\cos(\alpha)\sin(\alpha) \\ \beta\cos(\alpha)\sin(\alpha) & 1+\beta\sin^2(\alpha) \end{bmatrix}. \tag{3.66}$$

Thus, the crack density function γ per unit volume in Eq. (3.17) is rewritten as

$$\gamma(s, \nabla s) = \frac{(1-s)^2}{4\kappa} + \kappa\,\boldsymbol{\omega} : (\nabla s \otimes \nabla s). \tag{3.67}$$

3.3.2 Phase-field modelling of crack evolution in anisotropic materials

Consider a homogenous anisotropic linear elastic body Ω with an initial crack Γ, as shown in Fig. 3.2. The local components of the coefficients of thermal expansion in two-dimensional case are expressed as

$$\underline{\boldsymbol{\alpha}}_T = \begin{bmatrix} \underline{\alpha}_{T,11} & 0 \\ 0 & \underline{\alpha}_{T,22} \end{bmatrix}, \tag{3.68}$$

where $\underline{\alpha}_{T,11}$ and $\underline{\alpha}_{T,22}$ are defined as the coefficients of thermal expansion in principal directions. For an isotropic medium, $\underline{\alpha}_{T,11} = \underline{\alpha}_{T,22}$. A coordinate transformation is required as the global cartesian axes will not be aligned with the principal directions (see Fig. 3.4). The global components of the coefficients of thermal expansion in two-dimensional case are given by

$$\boldsymbol{\alpha}_T = \begin{bmatrix} \alpha_{T,xx} & \alpha_{T,xy} \\ \alpha_{T,yx} & \alpha_{T,yy} \end{bmatrix} = \boldsymbol{R}\underline{\boldsymbol{\alpha}}_T\boldsymbol{R}^T, \tag{3.69}$$

or when multiplied out $\left(\alpha_{T,xy} = \alpha_{T,yx}\right)$

$$\boldsymbol{\alpha}_T = \begin{bmatrix} \underline{\alpha}_{T,11}\cos^2(\alpha) + \underline{\alpha}_{T,22}\sin^2(\alpha) & -\underline{\alpha}_{T,11}\sin\alpha\cos\alpha + \underline{\alpha}_{T,22}\sin(\alpha)\cos(\alpha) \\ -\underline{\alpha}_{T,11}\sin(\alpha)\cos(\alpha) + \underline{\alpha}_{T,22}\sin(\alpha)\cos(\alpha) & \underline{\alpha}_{T,11}\sin^2(\alpha) + \underline{\alpha}_{T,22}\cos^2(\alpha) \end{bmatrix}, \tag{3.70}$$

with the material orientation α and the rotation matrix $\boldsymbol{R}$

$$\boldsymbol{R} = \begin{bmatrix} \cos(\alpha) & \sin(\alpha) \\ -\sin(\alpha) & \cos(\alpha) \end{bmatrix}. \tag{3.71}$$

Using Eq. (3.69), anisotropic thermal strains in cartesian coordinates are expressed as

$$\boldsymbol{\varepsilon}_\theta = (\theta - \theta_0)\,\boldsymbol{\alpha}_T, \tag{3.72}$$

where θ, θ_0 are defined as the temperature and reference temperature, respectively. In an isothermal case, θ is equal to θ_0 for $t \in [0, T]$.

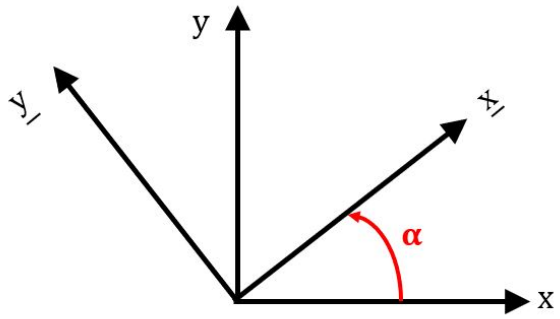

Figure 3.4: Local and global coordinate systems.

By Eq. (3.72), the elastic strain energy density in anisotropic materials is defined as

$$\psi_e(\boldsymbol{\varepsilon}_e, \theta) = \frac{1}{2}\boldsymbol{\varepsilon}_e : \mathbb{C} : \boldsymbol{\varepsilon}_e, \tag{3.73}$$

with the anisotropic fourth-order elastic stiffness tensor $\mathbb{C}$.

In the following we want to focus only on transversely isotropic materials and hence, the principal stiffness matrix in 2D can be reduced to

$$\underline{\boldsymbol{C}} = \begin{bmatrix} \underline{C}_{11} & \underline{C}_{12} & 0 \\ \underline{C}_{12} & \underline{C}_{22} & 0 \\ 0 & 0 & \underline{C}_{44} \end{bmatrix}, \tag{3.74}$$

and transversely isotropic is achieved if $\underline{C}_{44} \neq (\underline{C}_{11} - \underline{C}_{12})/2$ and $\underline{C}_{11} \neq \underline{C}_{22}$.

The Voigt notation of the anisotropic fourth-order elastic stiffness tensor is expressed as

$$\boldsymbol{C} = \boldsymbol{P}\underline{\boldsymbol{C}}\boldsymbol{P}^T, \tag{3.75}$$

where $\boldsymbol{P}$ is a matrix which transposes the principal stiffness matrix $\underline{\boldsymbol{C}}$ to the oriented stiffness matrix $\boldsymbol{C}$ in cartesian coordinates. The transformation matrix $\boldsymbol{P}$ is defined as

$$P = \begin{bmatrix} \cos^2(\alpha) & \sin^2(\alpha) & 2\cos(\alpha)\sin(\alpha) \\ \sin^2(\alpha) & \cos^2(\alpha) & -2\cos(\alpha)\sin(\alpha) \\ -\cos(\alpha)\sin(\alpha) & \cos(\alpha)\sin(\alpha) & \cos^2(\alpha) - \sin^2(\alpha) \end{bmatrix}. \tag{3.76}$$

To avoid unphysical compressive fracture in anisotropic solids, we follow the work by Amor et al. [13]

$$\psi(\boldsymbol{\varepsilon}_e, s) = (s^2 + \eta)\psi_e^+ + \psi_e^-, \tag{3.77}$$

with

$$\psi_e^+ = \frac{1}{2}\boldsymbol{\varepsilon}_e[\mathbb{C} - K\mathbf{1} \otimes \mathbf{1}\text{sign}^-(\text{tr}(\boldsymbol{\varepsilon}_e))]\boldsymbol{\varepsilon}_e, \tag{3.78}$$

and

$$\psi_e^- = \frac{1}{2}K\text{sign}^-(\text{tr}(\boldsymbol{\varepsilon}_e))\boldsymbol{\varepsilon}_e\mathbf{1} \otimes \mathbf{1}\boldsymbol{\varepsilon}_e, \tag{3.79}$$

where the elastic strain energy density is split into a positive part ψ_e^+ and a negative part ψ_e^-. The crack phase-field s is only associated with the positive part of the elastic energy density in case of compression.

3.3.3 Governing equations for the evolution of the crack phase-field in anisotropic materials

The Lagrangian for anisotropic fracture problems is defined as

$$\begin{aligned} L = &- \int_\Omega \left[(s^2+\eta)\psi_e^+ + \psi_e^- + \mathscr{G}_c \left[\frac{(1-s)^2}{4\kappa} + \kappa\, \boldsymbol{\omega} : (\nabla s \otimes \nabla s) \right] \right] \mathrm{d}v \\ &+ \int_{\partial\Omega_{\boldsymbol{t}}} \boldsymbol{t} \cdot \boldsymbol{u}\, \mathrm{d}a, \end{aligned} \tag{3.80}$$

when body forces are neglected.

The strong-form governing equations can be derived from Eq. (3.80):

$$\begin{cases} \operatorname{div} \boldsymbol{\sigma} = \mathbf{0}, \text{ in } \Omega \times [0,T] \\ 2s\psi_{\mathrm{e}}^+ - \mathscr{G}_c \left[2\kappa \nabla s \cdot (\boldsymbol{\omega} \nabla s) + \dfrac{1-s}{2\kappa} \right] = 0, \text{ in } \Omega \times [0,T] \end{cases} \tag{3.81}$$

in the domain Ω along with the Neumann boundary conditions

$$\begin{cases} \boldsymbol{\sigma} \cdot \boldsymbol{n} = \boldsymbol{t}, & \text{on } \partial\Omega_{\boldsymbol{t}} \times [0,T] \\ \nabla s \cdot \mathbf{n} = 0, & \text{on } \partial\Omega_{\mathrm{s}} \times [0,T] \end{cases} \tag{3.82}$$

where $\mathbf{n}$ presents the outward pointing normal vector to the boundary, and the effective stress tensor $\boldsymbol{\sigma}$ is given by

$$\boldsymbol{\sigma} = (s^2+\eta) \underbrace{[\mathbb{C} - K\mathbf{1}\otimes\mathbf{1}\mathrm{sign}^-(\mathrm{tr}(\boldsymbol{\varepsilon}))]\boldsymbol{\varepsilon}_e}_{\boldsymbol{\sigma}^+ = \dfrac{\partial \psi_e^+}{\partial \boldsymbol{\varepsilon}_e}} + \underbrace{K\mathrm{sign}^-(\mathrm{tr}(\boldsymbol{\varepsilon}_e))\mathbf{1}\otimes\mathbf{1}\boldsymbol{\varepsilon}_e}_{\boldsymbol{\sigma}^- = \dfrac{\partial \psi_e^-}{\partial \boldsymbol{\varepsilon}_e}}. \tag{3.83}$$

3.3.4 Governing equations for heat transfer in anisotropic materials

Assuming that the volumetric heat generation per unit volume per unit time is neglected, the transient heat conduction equation for an anisotropic material is given by

$$\rho c_p \dot{\theta} + \mathrm{div}\boldsymbol{q} = 0. \tag{3.84}$$

with the heat flux $\boldsymbol{q}$

$$\boldsymbol{q} = -\left(\zeta\left(s^2 - 1\right) + 1\right)\boldsymbol{K}\nabla\theta, \tag{3.85}$$

where $\zeta \in [0, 1]$ defines how the anisotropic thermal conductivity $\boldsymbol{K}$ is influenced by the crack phase-field [223]. If $\zeta = 1$, the crack phase-field is thermally isolating. If $\zeta = 0$, the heat transfer is not influenced by the crack phase-field.

In two-dimensional case, the local components of the coefficients of anisotropic thermal conductivity in principal directions are given by

$$\underline{\boldsymbol{K}} = \begin{bmatrix} \underline{k}_{11} & 0 \\ 0 & \underline{k}_{22} \end{bmatrix}, \tag{3.86}$$

with k_{11} and k_{22} denoting the thermal conductivity coefficients in principal directions. In case of an isotropic material, $\underline{k}_{11} = \underline{k}_{22}$. Further on, the global components of the coefficients of anisotropic thermal conductivity in cartesian coordinates are given by [207]

$$\boldsymbol{K} = \begin{bmatrix} k_{xx} & k_{xy} \\ k_{yx} & k_{yy} \end{bmatrix} = \boldsymbol{R}\underline{\boldsymbol{K}}\boldsymbol{R}^T, \tag{3.87}$$

or when multiplied out $\left(k_{xy} = k_{yx}\right)$

$$\boldsymbol{K} = \begin{bmatrix} \underline{k}_{11}\cos^2(\alpha) + \underline{k}_{22}\sin^2(\alpha) & -\underline{k}_{11}\sin(\alpha)\cos(\alpha) + \underline{k}_{22}\sin(\alpha)\cos(\alpha) \\ -\underline{k}_{11}\sin(\alpha)\cos(\alpha) + \underline{k}_{22}\sin(\alpha)\cos(\alpha) & \underline{k}_{11}\sin^2(\alpha) + \underline{k}_{22}\cos^2(\alpha) \end{bmatrix}, \tag{3.88}$$

where α is defined as the material orientation.

The temperature field satisfies the following boundary conditions on the surface of a body,

$$\begin{cases} \theta = \theta_s, & \text{on } \partial\Omega_\theta \times [0,T] \\ -\boldsymbol{q}\cdot\boldsymbol{n} = \boldsymbol{q}_s, & \text{on } \partial\Omega_{\boldsymbol{q}} \times [0,T] \end{cases} \tag{3.89}$$

with the specified temperature θ_s on $\partial\Omega_\theta$ and the prescribed heat flux $\boldsymbol{q}_s$ on $\partial\Omega_{\boldsymbol{q}}$.

3.4 Initial values and boundary conditions

The following initial values for phase-field brittle fracture problems are imposed:

$$\begin{cases} \boldsymbol{u}(\boldsymbol{x},0) = \boldsymbol{u}_0(\boldsymbol{x}), & \text{in } \Omega \times [0,T] \\ s(\boldsymbol{x},0) = \boldsymbol{s}_0(\boldsymbol{x}), & \text{in } \Omega \times [0,T] \\ \theta(\boldsymbol{x},0) = \theta_0(\boldsymbol{x}). & \text{in } \Omega \times [0,T] \end{cases} \tag{3.90}$$

In this work, the preexisting crack is modelled as a geometrical discontinuity by duplicated nodes [115]. Dirichlet and Neumann boundary conditions for the displacements, the crack phase-field and the temperature field are introduced in Sect. 3.2 and Sect. 3.3.

3.5 Irreversibility of the crack phase-field

In order to prevent unphysical healing of fractures, three commonly used methods that enforce the irreversibility constraints on the phase-field equations are introduced

in this section.

1. ***Damage like formulation [169]***

   In the first method, the irreversibility of the crack phase-field is ensured by introducing a penalty term, which enforces that the time derivative $\dot{s}$ is non-positive over time, i.e.

   $$\dot{s}(\boldsymbol{x}, t) \leq 0. \tag{3.91}$$

2. ***Homogeneous Dirichlet boundary conditions [133]***

   In the second method, a homogeneous Dirichlet boundary condition is applied. When $s \leq 0$ is reached for the time $t^*_{\boldsymbol{x}}$, the material point remains totally damaged for the subsequent time, i.e.

   $$s(\boldsymbol{x}, t \geq t^*_{\boldsymbol{x}}) = 0. \tag{3.92}$$

3. ***History variables $\mathcal{H}$ [114]***

   In the last method, a rate-independent history-field of the maximum strain energy density is introduced, i.e.

   $$\mathcal{H}(\boldsymbol{x}, t) = \max_{\tau \in [0,t]} \psi_e^+(\boldsymbol{\varepsilon}_e(\boldsymbol{x})). \tag{3.93}$$

4

A study on phase-field modelling of mixed mode crack propagation in compression

In this chapter, a set of numerical examples to demonstrate the performance of four commonly used phase-field models is presented. This set includes

- a V-notched specimen subjected to cyclic loadings,

- a V-notched specimen subjected to compressive loadings,
- a specimen containing two parallel preexisting cracks subjected to compressive loadings.

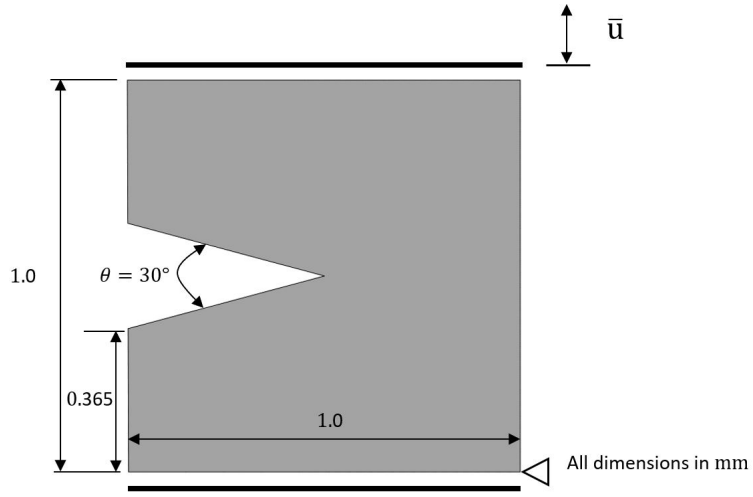

Figure 4.1: Geometry and boundary conditions of the V-notched specimen.

4.1 Crack evolution under cyclic loadings

First, four commonly used phase-field models are used for simulating crack evolution in a V-notched specimen under cyclic loadings. Fig. 4.1 shows the geometry size and boundary conditions of the V-notched specimen. The material parameters are chosen as $\lambda = 121\,150\,\mathrm{N/mm^2}$, $\mu = 80\,769\,\mathrm{N/mm^2}$, $\mathscr{G}_c = 2.7\,\mathrm{N/mm}$ and $\eta = 1.0 \times 10^{-6}$ [171]. The specimen is discretized by 23800 four-node quadrilateral elements with an effective mesh size $h = 0.005\,\mathrm{mm}$. Plane strain condition is assumed. The diffuse parameter κ is chosen as $0.005\,\mathrm{mm}$. The displacement increment is set as $\Delta\overline{\mathbf{u}} = 2.2 \times 10^{-6}\,\mathrm{mm}$ during the stable crack propagation (stage E). A cyclic imposed displacement envelope $\overline{\mathbf{u}}$ is prescribed as (see Fig. 4.2):

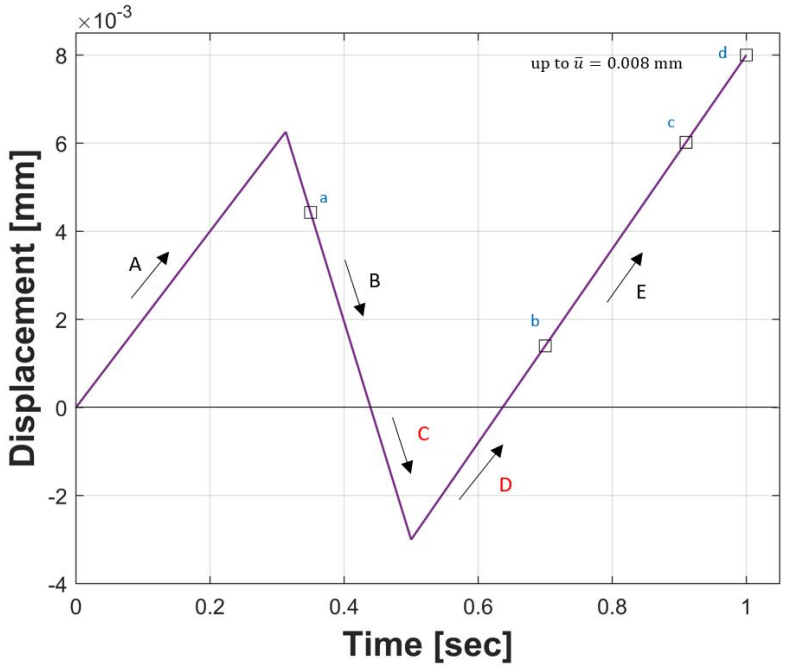

Figure 4.2: The cyclic loading history on $\overline{\mathbf{u}}$.

$$\overline{\mathbf{u}} = \begin{cases} 0.02 \cdot t \cdot 1\text{mm/s}, & \text{for } t \in \mathcal{I}_1 := [0; 0.313\text{s}] \\ (-0.0495175 \cdot t + 0.0217594) \cdot 1\text{mm/s}, & \text{for } t \in \mathcal{I}_2 := [0.313\text{s}; 0.5\text{s}] \\ (0.022 \cdot t - 0.014) \cdot 1\text{mm/s}, & \text{for } t \in \mathcal{I}_3 := [0.5\text{s}; 1.0\text{s}] \end{cases}$$

The force-displacement curves predicted by four commonly used models are depicted in Fig. 4.3, which present that all models have the same fracture behavior at all loading stages except for stage C and D, when the compressive loads act on the specimen.

Because the isotropic [41] and hybrid [69] models do not intrinsically possess the capability to prevent material interpenetration during the compression phase, the secant elastic responses are found at the stage C and D as shown in Fig. 4.3. More significantly, Storm et al. [246] pointed out that the crack closure effect is not considered in the hybrid model [11].

In order to avoid material interpenetration under compressive loadings, two kinds

of stress-strain relations are considered, namely: (i) decomposition of the elastic strain tensor into a deviatoric part and a volumetric part [169]; (ii) spectral decomposition of the elastic strain tensor into a tension part and a compression part [221]. As shown in Fig. 4.3, both spectral [169] and volumetric/deviatoric [221] splits guarantee the stiffness recovery at the stage C and D. However, the volumetric/deviatoric split shows a lower mechanical response due to the modification of the stiffness tensor in case of compression (see Sect. 3.2.4). It is worth mentioning that the peak force in the spectral split model is lower than in other models. One reason may be that the spectral split allows for the spectral decomposition of the elastic strain tensor under compressive loadings.

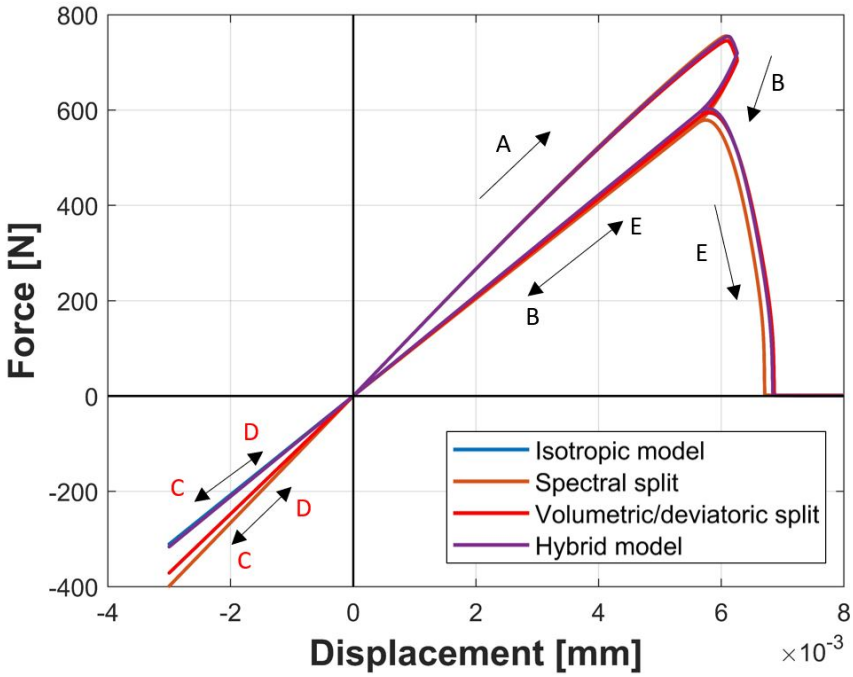

Figure 4.3: Force-displacement curves: comparison of different phase-field models at the loading stages in Fig. 4.2.

The contour plots of crack evolution predicted by different models are depicted in Figs. 4.4 to 4.7. Blue and red colors correspond to the intact and totally damaged

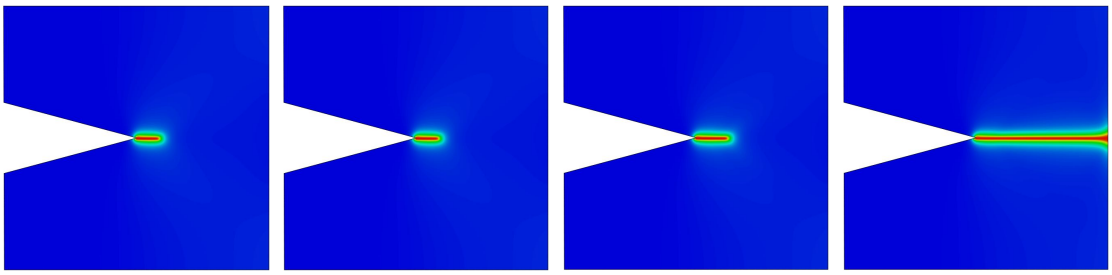

(a) $\overline{\mathbf{u}} = 0.0044\,\mathrm{mm}$ **(b)** $\overline{\mathbf{u}} = 0.0014\,\mathrm{mm}$ **(c)** $\overline{\mathbf{u}} = 0.0058\,\mathrm{mm}$ **(d)** $\overline{\mathbf{u}} = 0.008\,\mathrm{mm}$

Figure 4.4: Crack evolution process predicted by the isotropic model (a) $\overline{\mathbf{u}} = 0.0044\,\mathrm{mm}$ (b) $\overline{\mathbf{u}} = 0.0014\,\mathrm{mm}$ (c) $\overline{\mathbf{u}} = 0.0058\,\mathrm{mm}$ (d) $\overline{\mathbf{u}} = 0.008\,\mathrm{mm}$.

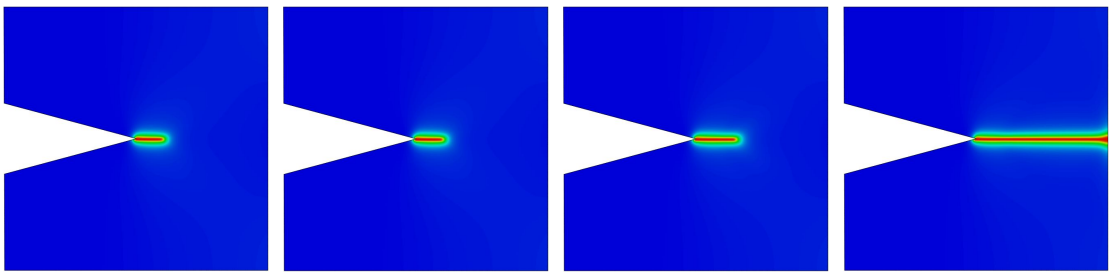

(a) $\overline{\mathbf{u}} = 0.0044\,\mathrm{mm}$ **(b)** $\overline{\mathbf{u}} = 0.0014\,\mathrm{mm}$ **(c)** $\overline{\mathbf{u}} = 0.0058\,\mathrm{mm}$ **(d)** $\overline{\mathbf{u}} = 0.008\,\mathrm{mm}$

Figure 4.5: Crack evolution process predicted by the spectral split (a) $\overline{\mathbf{u}} = 0.0044\,\mathrm{mm}$ (b) $\overline{\mathbf{u}} = 0.0014\,\mathrm{mm}$ (c) $\overline{\mathbf{u}} = 0.0058\,\mathrm{mm}$ (d) $\overline{\mathbf{u}} = 0.008\,\mathrm{mm}$.

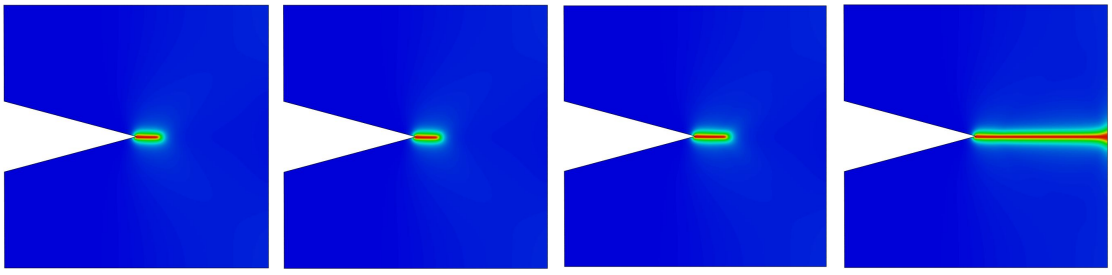

(a) $\overline{\mathbf{u}} = 0.0044\,\mathrm{mm}$ **(b)** $\overline{\mathbf{u}} = 0.0014\,\mathrm{mm}$ **(c)** $\overline{\mathbf{u}} = 0.0058\,\mathrm{mm}$ **(d)** $\overline{\mathbf{u}} = 0.008\,\mathrm{mm}$

Figure 4.6: Crack evolution process predicted by the volumetric/deviatoric split (a) $\overline{\mathbf{u}} = 0.0044\,\mathrm{mm}$ (b) $\overline{\mathbf{u}} = 0.0014\,\mathrm{mm}$ (c) $\overline{\mathbf{u}} = 0.0058\,\mathrm{mm}$ (d) $\overline{\mathbf{u}} = 0.008\,\mathrm{mm}$.

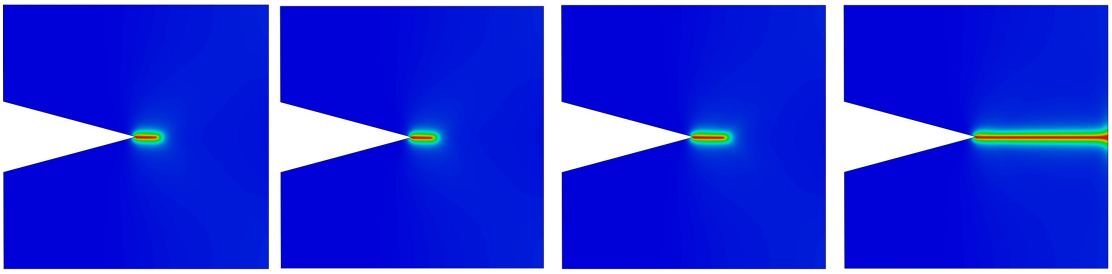

(a) $\overline{\mathbf{u}} = 0.0044\,\mathrm{mm}$ **(b)** $\overline{\mathbf{u}} = 0.0014\,\mathrm{mm}$ **(c)** $\overline{\mathbf{u}} = 0.0058\,\mathrm{mm}$ **(d)** $\overline{\mathbf{u}} = 0.008\,\mathrm{mm}$

Figure 4.7: Crack evolution process predicted by the hybrid model (a) $\overline{\mathbf{u}} = 0.0044\,\mathrm{mm}$ (b) $\overline{\mathbf{u}} = 0.0014\,\mathrm{mm}$ (c) $\overline{\mathbf{u}} = 0.0058\,\mathrm{mm}$ (d) $\overline{\mathbf{u}} = 0.008\,\mathrm{mm}$.

materials, respectively. It can be observed that all the samples evolve in a similar fashion. Table 4.1 shows a computational time comparison [1]. It can be seen that the hybrid model enables a reduction of the computational time. More precisely, the hybrid model is more efficient than the volumetric/deviatoric and spectral splits. Interestingly, however, the hybrid model runs slower than the isotropic model. One of the possible reasons is the calculation of the principal elastic strains and principal elastic strain directions.

	Isotropic model	Spectral split	V/D split	Hybrid model
Run time [s]	30808	35599	31490	31048

Table 4.1: Run time comparison for four commonly used phase-field models under consideration.

4.2 Crack evolution under compressive loadings

Next, we focus on crack growth in compression. To this end, the same arrangement of the V-notched specimen is used for another simulation, in which the loading on $\overline{\mathbf{u}}$ is

[1] The run time comparison is performed on a desktop workstation using an Intel(R) Core(TM) i7-4790 CPU @ 3.60GHz.

defined as (see Fig. 4.8):

$$\overline{\mathbf{u}} = \begin{cases} 0.02 \cdot t \cdot 1\text{mm/s}, & \text{for } t \in \mathcal{I}_1 := [0; 0.313\text{s}] \\ (-0.0671327 \cdot t + 0.0272725) \cdot 1\text{mm/s}. & \text{for } t \in \mathcal{I}_2 := [0.313; 1.2\text{s}] \end{cases}$$

The displacement increment is chosen as $\Delta\overline{\mathbf{u}} = 6.72 \times 10^{-6}\,\text{mm}$ during the stable crack propagation in compression. All other settings remain as before.

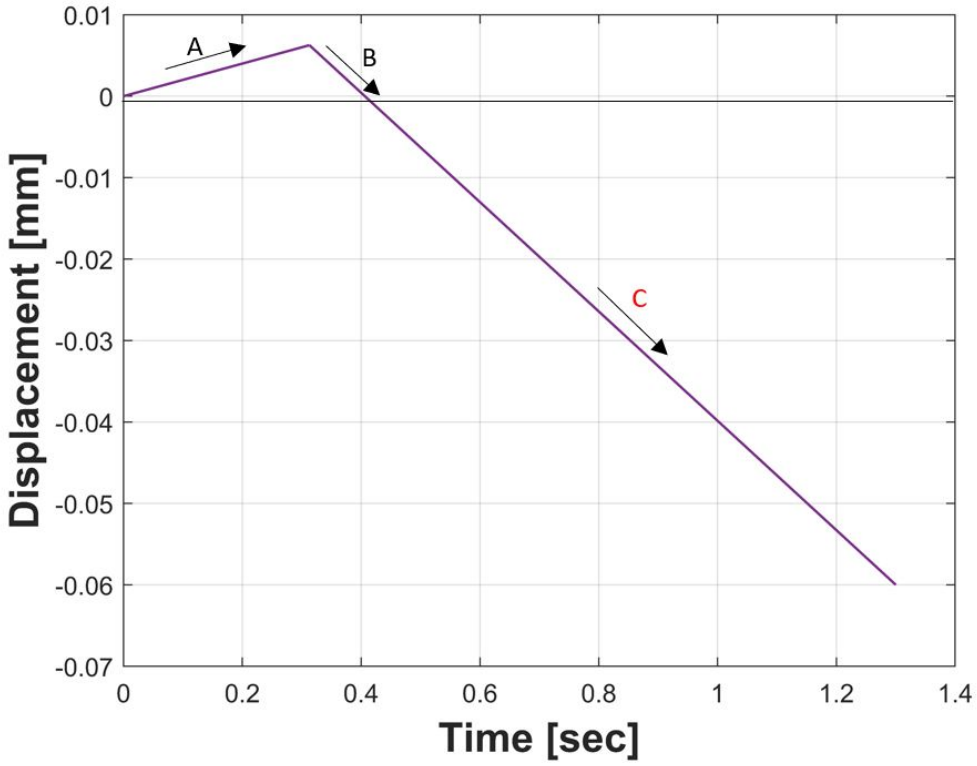

Figure 4.8: The loading history on $\overline{\mathbf{u}}$.

The load-displacement curves predicted by four commonly used models are plotted in Fig. 4.9. Even though the elastic responses at the stage A and B for all models are identical, different compressive fracture behaviors at the stage C are observed. It can be seen that the compressive bear capacity of the isotropic model is much lower than that of other models. The reason can be related to the fact that the isotropic model is

not able to distinguish between the fracture behavior in tension and compression.

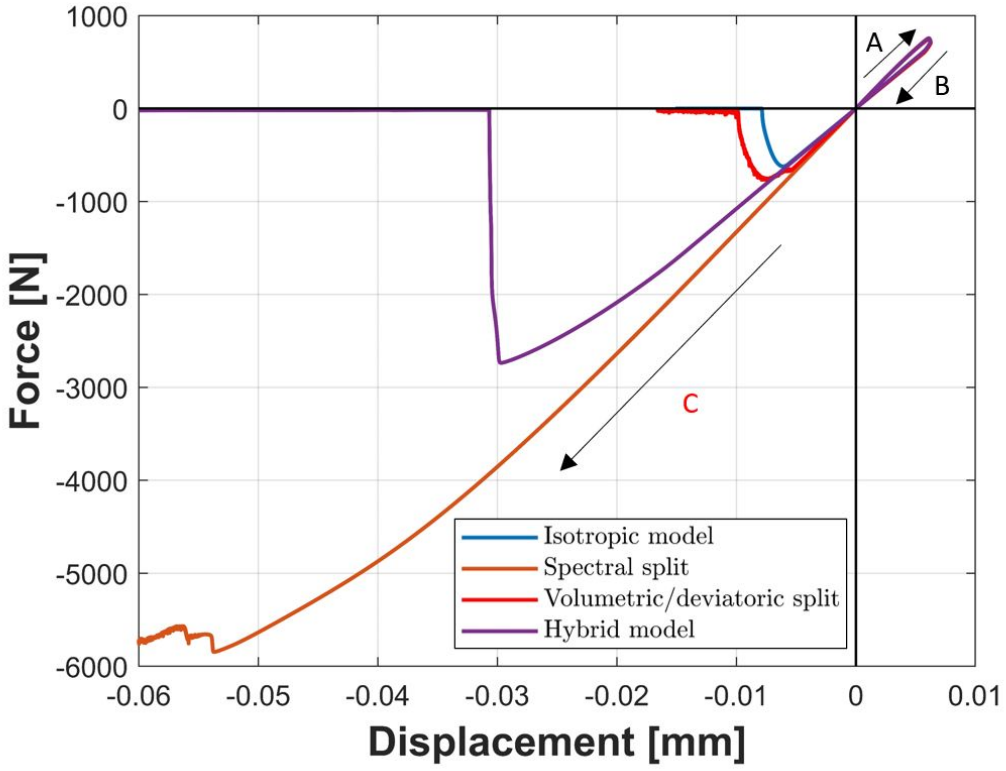

Figure 4.9: Force-displacement curves at the loading stages in Fig. 4.8.

Furthermore, the peak forces are not equal as shown in Fig. 4.9. The bear capacity of the volumetric/deviatoric split is much lower than that of the hybrid model [69] and spectral split [169]. One reason is that the compressive deviatoric strain energy density from the volumetric/deviatoric split contributes to crack evolution in compression. As illustrated in Fig. 4.9, it is of interest to note that the spectral split can absorb much more fracture energy than the hybrid model. One possible reason for this is that the hybrid model cannot avoid material interpenetration under continuous compressive loadings [246].

The contour plots of the crack phase-field predicted by the isotropic model at different load steps are shown in Fig. 4.10. It can be seen that the crack propagates in a

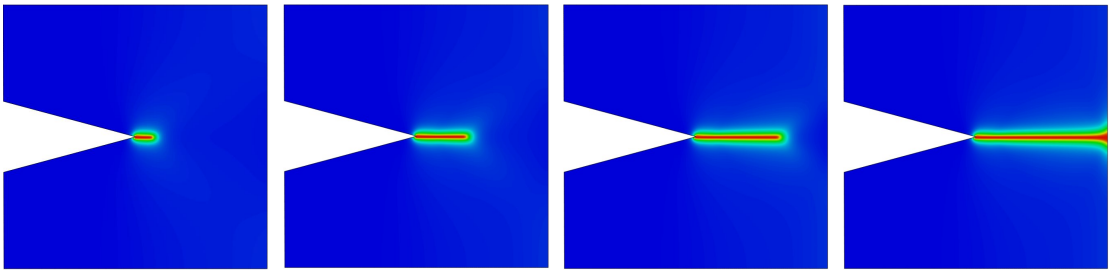

(a) $\overline{\mathbf{u}} = 0.0063\,\mathrm{mm}$ **(b)** $\overline{\mathbf{u}} = -0.0068\,\mathrm{mm}$ **(c)** $\overline{\mathbf{u}} = -0.0074\,\mathrm{mm}$ **(d)** $\overline{\mathbf{u}} = -0.008\,\mathrm{mm}$

Figure 4.10: Crack evolution process predicted by the isotropic model (a) $\overline{\mathbf{u}} = 0.0063\,\mathrm{mm}$ (b) $\overline{\mathbf{u}} = -0.0068\,\mathrm{mm}$ (c) $\overline{\mathbf{u}} = -0.0074\,\mathrm{mm}$ (d) $\overline{\mathbf{u}} = -0.008\,\mathrm{mm}$.

horizontal direction (see Figs. 4.10a to 4.10c). Moreover, the crack propagation period is quite short. Finally, the specimen is divided into two pieces as shown in Fig. 4.10d.

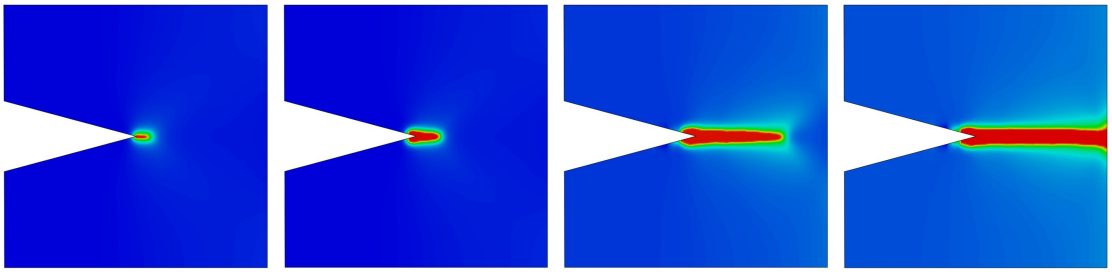

(a) $\overline{\mathbf{u}} = 0.0063\,\mathrm{mm}$ **(b)** $\overline{\mathbf{u}} = -0.0069\,\mathrm{mm}$ **(c)** $\overline{\mathbf{u}} = -0.0092\,\mathrm{mm}$ **(d)** $\overline{\mathbf{u}} = -0.012\,\mathrm{mm}$

Figure 4.11: Crack evolution process predicted by the volumetric/deviatoric split (a) $\overline{\mathbf{u}} = 0.0063\,\mathrm{mm}$ (b) $\overline{\mathbf{u}} = -0.0069\,\mathrm{mm}$ (c) $\overline{\mathbf{u}} = -0.0092\,\mathrm{mm}$ (d) $\overline{\mathbf{u}} = -0.012\,\mathrm{mm}$.

Next, the evolution of the crack phase-field predicted by the volumetric/deviatoric split is plotted in Fig. 4.11. At the stage A, the crack first initiates at the notch tip and propagates in a horizontal direction under tensile loadings (see Fig. 4.11a). As shown in Fig. 4.12, at the stage C, the compressive loading leads to unrealistic structural deformations and overlapping edge faces. In the meantime, the crack has a tendency to become fat (see Figs. 4.11b and 4.11c). Finally, the specimen breaks into two parts as shown in Fig. 4.11d.

Fig. 4.13 shows the evolution of the crack phase-field predicted by the hybrid model at different load steps. Due to the tensile loading, the crack first propagates in a hor-

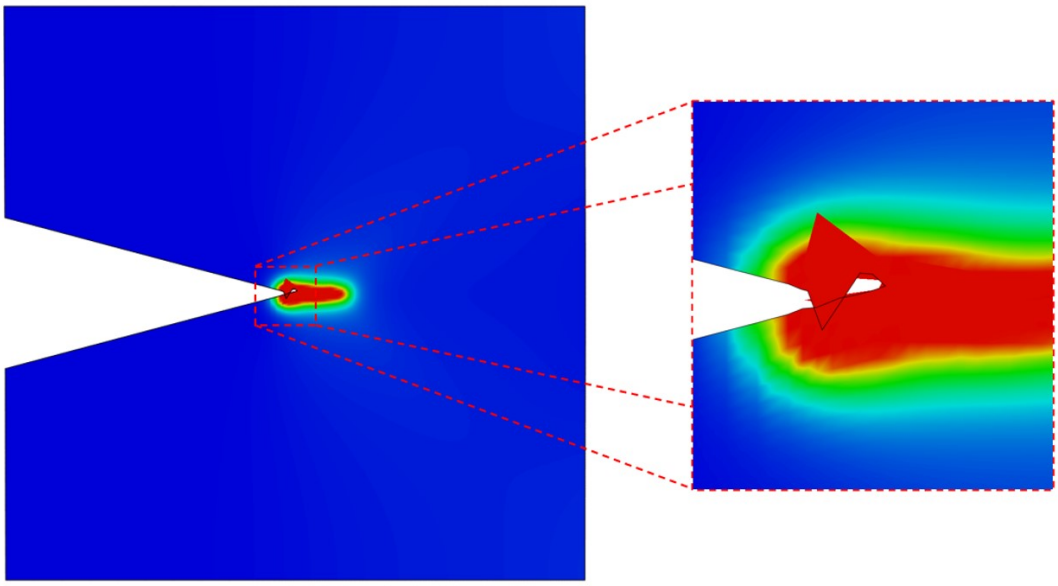

Figure 4.12: Deformed subversion predicted by the volumetric/deviatoric split ($\overline{\mathbf{u}} = -0.0069\,\mathrm{mm}$).

izontal direction at the stage A (see Fig. 4.13a). A secondary crack first initiates in front of the primary crack at the stage C (see Fig. 4.13b), and gradually turns to the vertical direction (see Fig. 4.13c). As opposed to the relatively stable crack propagation, the crack branching forms brutally (see Fig. 4.13d).

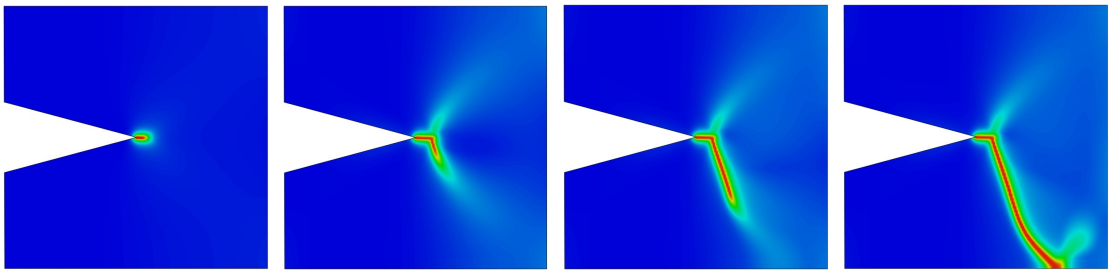

(a) $\overline{\mathbf{u}} = 0.0063\,\mathrm{mm}$ **(b)** $\overline{\mathbf{u}} = -0.0299\,\mathrm{mm}$ **(c)** $\overline{\mathbf{u}} = -0.0302\,\mathrm{mm}$ **(d)** $\overline{\mathbf{u}} = -0.0305\,\mathrm{mm}$

Figure 4.13: Crack evolution process predicted by the hybrid model (a) $\overline{\mathbf{u}} = 0.0063\,\mathrm{mm}$ (b) $\overline{\mathbf{u}} = -0.0299\,\mathrm{mm}$ (c) $\overline{\mathbf{u}} = -0.0302\,\mathrm{mm}$ (d) $\overline{\mathbf{u}} = -0.0305\,\mathrm{mm}$.

Fig. 4.14 presents the evolution of the crack phase-field predicted by the spectral split. At the stage A, the crack first initiates at the notch tip and propagates horizon-

tally as shown in Fig. 4.14a. After that, the compressive loading leads to secondary crack initiation at the notch tip (see Fig. 4.14b). For a better understanding of secondary crack nucleation and propagation in compression, the deformed subversion is plotted in Fig. 4.15. It can be observed that both upper and lower surfaces are brought into contact, leading to overlapping edge faces. With a significant load increase, the secondary cracks gradually turn to the vertical direction (see Figs. 4.14c and 4.14d).

It remains to be seen whether the spectral split correctly simulates the compressive fracturing process or not, because no such experimental information is available. A experimental study will therefore be pursued in future. Moreover, the volumetric/deviatoric and spectral splits induce spurious damage regions during the compression phase. On the contrary, such spurious effects cannot be found in the hybrid model. In particular, none of these models are capable of simulating self-contacts.

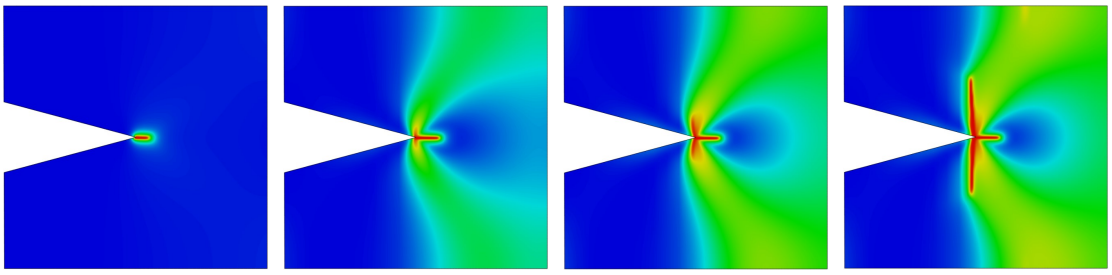

(a) $\overline{\mathbf{u}} = 0.0063\,\mathrm{mm}$ **(b)** $\overline{\mathbf{u}} = -0.0412\,\mathrm{mm}$ **(c)** $\overline{\mathbf{u}} = -0.0508\,\mathrm{mm}$ **(d)** $\overline{\mathbf{u}} = -0.0537\,\mathrm{mm}$

Figure 4.14: Crack evolution process predicted by the spectral split (a) $\overline{\mathbf{u}} = 0.0063\,\mathrm{mm}$ (b) $\overline{\mathbf{u}} = -0.0412\,\mathrm{mm}$ (c) $\overline{\mathbf{u}} = -0.0508\,\mathrm{mm}$ (d) $\overline{\mathbf{u}} = -0.0537\,\mathrm{mm}$.

Remark 3 *The work done by Nagaraja [178] has demonstrated that the hybrid model cannot be used for simulating crack initiation and propagation under compressive loadings.*

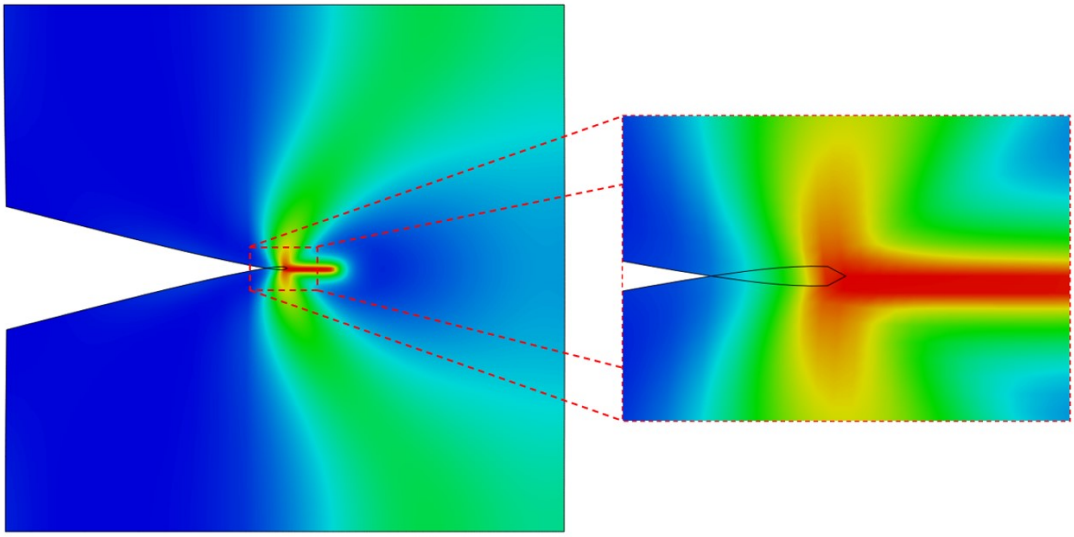

Figure 4.15: Deformed subversion predicted by the spectral split ($\overline{\mathbf{u}} = -0.0412\,\mathrm{mm}$).

4.3 Crack evolution in a specimen containing two parallel preexisting cracks under compressive loadings

In this example, four commonly used models are used for simulating crack evolution in a specimen containing two parallel preexisting cracks with different bridge angles γ under uniaxial compressive loadings. The orientation of the preexisting cracks is chosen as $\alpha = 45°$. The geometry and boundary conditions of the specimen subjected to compression are shown in Fig. 4.16. The length and width of preexisting cracks are given as 30 mm and 2 mm, respectively. The material parameters are taken as $\lambda = 41\,724\,\mathrm{N/mm^2}$, $\mu = 25\,573\,\mathrm{N/mm^2}$, $\mathscr{G}_c = 1.4\,\mathrm{N/mm}$, $\kappa = 0.25\,\mathrm{mm}$ and $\eta = 1.0 \times 10^{-6}$ [145]. A staggered solution scheme, a displacement-controlled uniaxial compression and plane strain condition are chosen. The specimen is discretized by 284152 four-node quadrilateral elements with an effective mesh size $h = 0.25\,\mathrm{mm}$. The orientation of the bridge is represented by the angle γ (see Fig. 4.16). Three cases, $\gamma = 23°$, $\gamma = 68°$ and $\gamma = 90°$ are considered. The displacement increment is set as

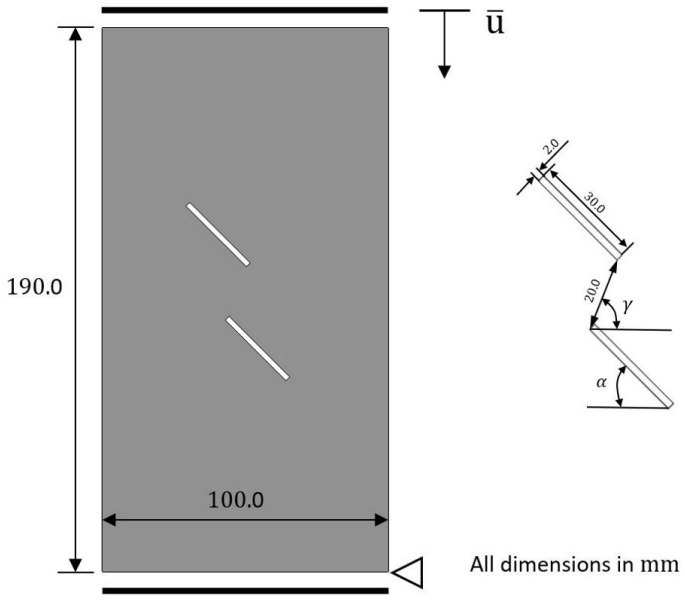

Figure 4.16: Geometry of specimen and boundary conditions of a specimen containing two parallel preexisting cracks under compressive loadings

$\Delta\overline{\mathbf{u}} = 9.5 \times 10^{-4}$ mm during the stable fracturing processes.

Crack propagation in case of $\gamma = 23°$

Fig. 4.17 presents the crack evolution process predicted by the isotropic model, as well as experimental results for the geometry in case of $\gamma = 23°$. For this case, four wing cracks first initiate at the inner and outer tips of the preexisting cracks due to the compressive loadings (see Fig. 4.17a). Subsequently, four wing cracks propagate in a horizontal direction and the evolution of wing cracks is relatively stable (see Fig. 4.17b). Finally, the shear-dominated fractures propagate brutally towards the left and right edges (see Figs. 4.17c and 4.17d). The simulated crack patterns do not coincide with the experimental results (see Fig. 4.17e).

Fig. 4.18 presents the crack evolution process predicted by the spectral split, as well as experimental results for the geometry in case of $\gamma = 23°$. For this case, all wing cracks first initiate at the tips of the preexisting cracks in compression (see

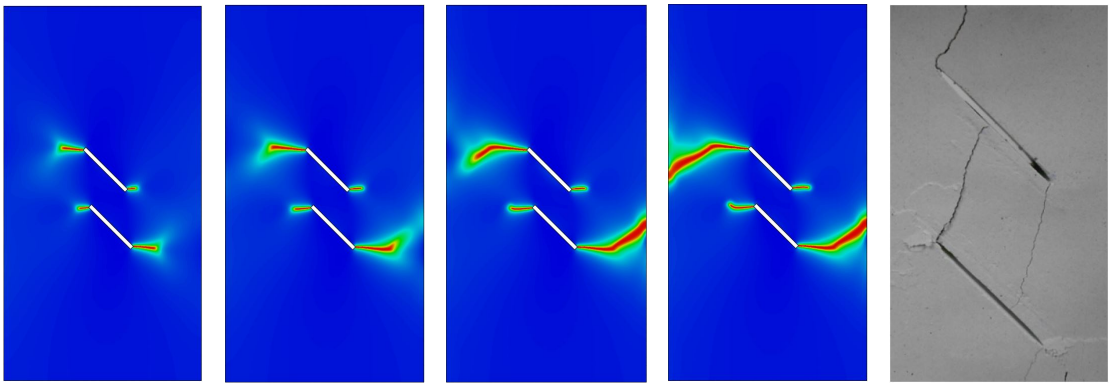

(a) $\overline{\mathbf{u}} = 0.25\,\mathrm{mm}$ **(b)** $\overline{\mathbf{u}} = 0.27\,\mathrm{mm}$ **(c)** $\overline{\mathbf{u}} = 0.28\,\mathrm{mm}$ **(d)** $\overline{\mathbf{u}} = 0.29\,\mathrm{mm}$ **(e)** experiment

Figure 4.17: Crack evolution process predicted by the isotropic model in case of $\gamma = 23°$.

Fig. 4.18a). Next, wing cracks propagate in the direction sub-perpendicular to the surface of the preexisting cracks (see Fig. 4.18b), which agrees well with the observations from the experimental results (see Fig. 4.18e). After that, secondary cracks initiate near the preexisting cracks (see Fig. 4.18c), which are deemed to be shear-dominated fractures [145]. Finally, the secondary cracks coalesce (see Fig. 4.18d).

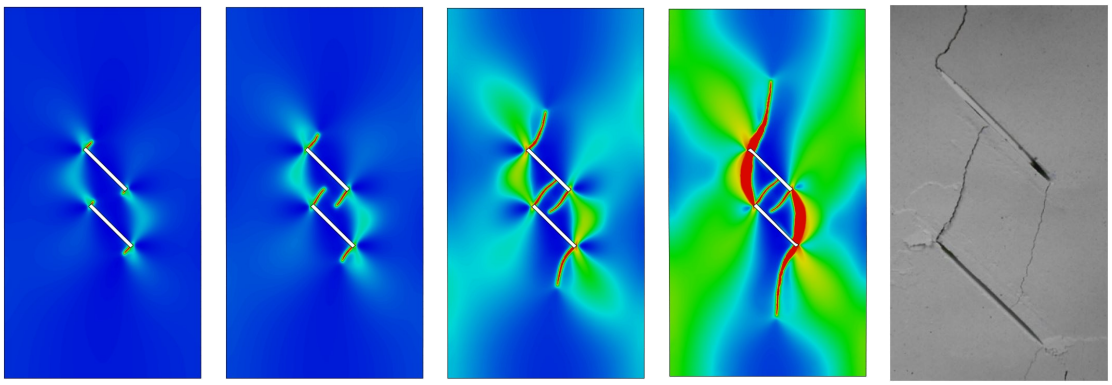

(a) $\overline{\mathbf{u}} = 0.74\,\mathrm{mm}$ **(b)** $\overline{\mathbf{u}} = 0.86\,\mathrm{mm}$ **(c)** $\overline{\mathbf{u}} = 1.25\,\mathrm{mm}$ **(d)** $\overline{\mathbf{u}} = 1.71\,\mathrm{mm}$ **(e)** experiment

Figure 4.18: Crack evolution process predicted by the spectral split in case of $\gamma = 23°$.

Fig. 4.19 presents the crack evolution process predicted by the volumetric/deviatoric split, as well as experimental results for the geometry in case of $\gamma = 23°$. For this case, compressive wing cracks initiate at the tips of the preexisting cracks (see Fig. 4.19a).

Next, four wing cracks become fat at the early stage of crack evolution (see Fig. 4.19b). Meanwhile, secondary fracture initiates in front of the outer wing cracks. The duration of crack initiation and propagation is quite short. Subsequently, one outer wing crack propagates along an angle of around $-135°$, and the other one propagates along an angle of around $45°$ (see Fig. 4.19c), because the orientation of secondary cracks may present the direction of maximum shear stresses ($\pm 45°$). As shown in Fig. 4.19d, the simulated crack patterns cannot be compared with the experimental results (see Fig. 4.19e).

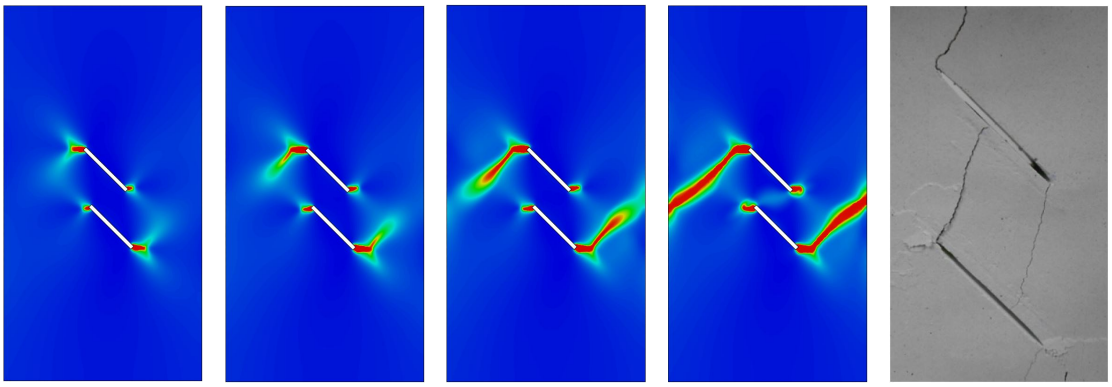

(a) $\overline{\mathbf{u}} = 0.32\,\mathrm{mm}$ **(b)** $\overline{\mathbf{u}} = 0.34\,\mathrm{mm}$ **(c)** $\overline{\mathbf{u}} = 0.35\,\mathrm{mm}$ **(d)** $\overline{\mathbf{u}} = 0.37\,\mathrm{mm}$ **(e)** experiment

Figure 4.19: Crack evolution process predicted by the volumetric/deviatoric split in case of $\gamma = 23°$.

Fig. 4.20 presents the crack evolution process predicted by the hybrid model, as well as experimental results for the geometry in case of $\gamma = 23°$. For this case, two wing cracks initiate at the outer tips, and propagate in the direction sub-perpendicular to the surfaces of preexisting cracks (see Fig. 4.20a). Meanwhile, another two wing cracks initiate at the inner tips of the preexisting cracks, and propagate nearly along the orientation of the surface of preexisting cracks (see Fig. 4.20a). The stable crack growth is the predominant fracture behavior at the early stage of failure (see Figs. 4.20b and 4.20c). After that, a strong shear stress zone arises between the outer tip of one preexisting crack and the front of the wing crack, which yields the appearance of

crack patterns as shown in Fig. 4.20d. Such crack patterns cannot be observed in experiments (see Fig. 4.20e).

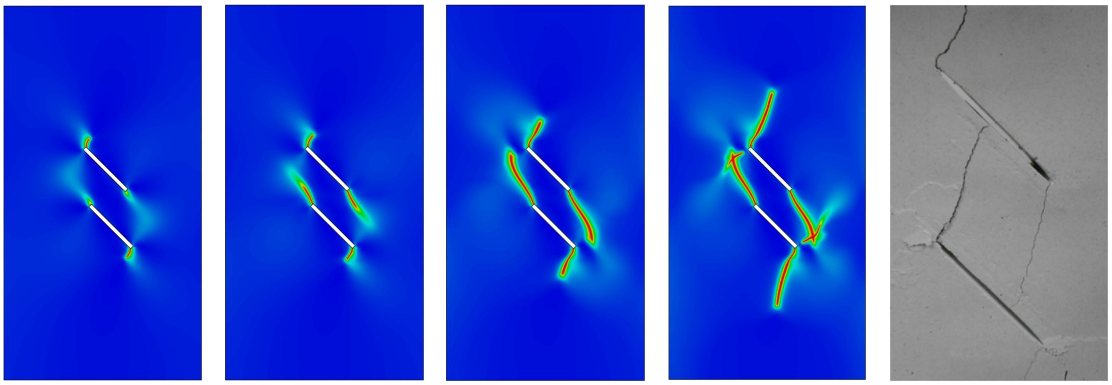

(a) $\overline{\mathbf{u}} = 0.65\,\mathrm{mm}$ **(b)** $\overline{\mathbf{u}} = 0.68\,\mathrm{mm}$ **(c)** $\overline{\mathbf{u}} = 0.71\,\mathrm{mm}$ **(d)** $\overline{\mathbf{u}} = 0.78\,\mathrm{mm}$ **(e)** experiment

Figure 4.20: Crack evolution process predicted by the hybrid model in case of $\gamma = 23°$.

Crack propagation in case of $\gamma = 68°$

Fig. 4.21 presents the crack evolution process predicted by the isotropic model, as well as experimental results for the geometry in case of $\gamma = 68°$. The fracture behavior is similar to the case of $\gamma = 23°$ (see Fig. 4.17). After a stable propagation of wing cracks (see Figs. 4.21a and 4.21b), strong shear zones arise near the left and right edges (see Fig. 4.21c). Fig. 4.21d and Fig. 4.21e show the numerically and experimentally obtained crack patterns, respectively. As evident, the simulated results are not similar to the ones obtained from the experiment.

Fig. 4.22 presents the crack evolution process predicted by the spectral split, as well as experimental results for the geometry in case of $\gamma = 68°$. For this case, the early stage of crack growth is similar to that in case of $\gamma = 23°$ (see Fig. 4.18). Four wing cracks first initiate at the tips of preexisting cracks, and propagate in a curvature manner (see Figs. 4.22a and 4.22b). Due to the further compressive loading, a strong shear zone forms between the preexisting cracks (see Fig. 4.22c). However, the inner

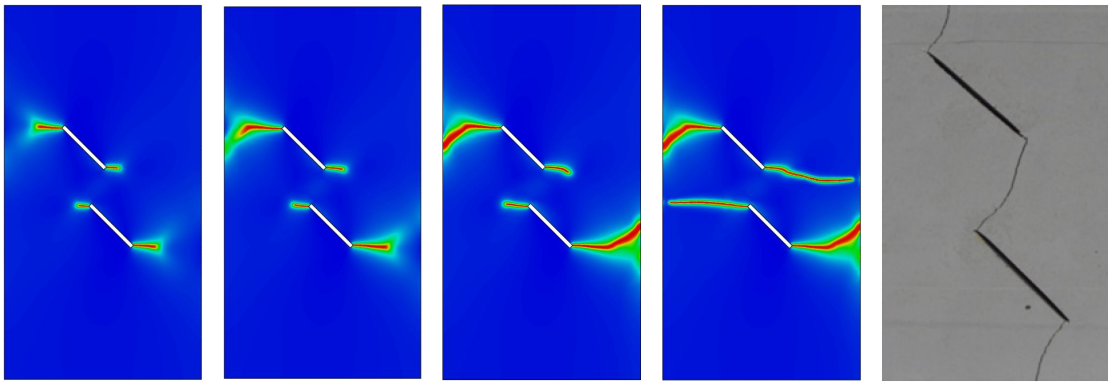

(a) $\overline{\mathbf{u}} = 0.25\,\mathrm{mm}$ **(b)** $\overline{\mathbf{u}} = 0.26\,\mathrm{mm}$ **(c)** $\overline{\mathbf{u}} = 0.29\,\mathrm{mm}$ **(d)** $\overline{\mathbf{u}} = 1.18\,\mathrm{mm}$ **(e)** experiment

Figure 4.21: Crack evolution process predicted by the isotropic model in case of $\gamma = 68°$.

wing cracks suddenly become fat, and finally get connected (see Fig. 4.22d). The numerical predictions do not agree with the experimental observations (see Fig. 4.22e).

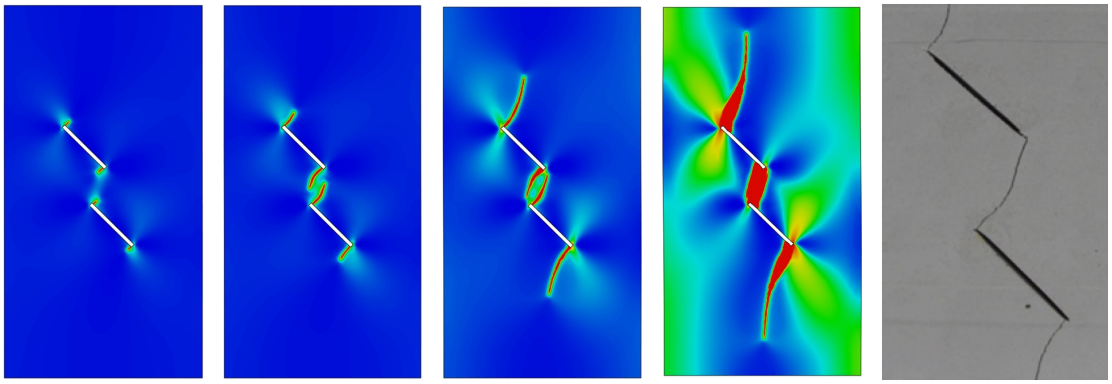

(a) $\overline{\mathbf{u}} = 0.58\,\mathrm{mm}$ **(b)** $\overline{\mathbf{u}} = 0.63\,\mathrm{mm}$ **(c)** $\overline{\mathbf{u}} = 0.86\,\mathrm{mm}$ **(d)** $\overline{\mathbf{u}} = 1.52\,\mathrm{mm}$ **(e)** experiment

Figure 4.22: Crack evolution process predicted by the spectral split in case of $\gamma = 68°$.

Fig. 4.23 presents the crack evolution process predicted by the volumetric/deviatoric split, as well as experimental results for the geometry in case of $\gamma = 68°$. The cracks first develop in a horizontal direction (see Figs. 4.23a and 4.23b). Moreover, secondary fractures propagate in a similar manner as those in case of $\gamma = 68°$ (see Fig. 4.19) except that the directions of secondary crack growth differ significantly. For this case, both outer wing cracks propagate along an angle of around $-45°$ (see

Fig. 4.23c). As shown in Fig. 4.23d, the obtained crack patterns, again, do not agree with the observations from experimental data (see Fig. 4.23e).

Fig. 4.24 presents the crack evolution process predicted by the hybrid model, as well as experimental results for the geometry in case of $\gamma = 68°$. All wing cracks initiate at the inner and outer tips of the preexisting cracks, and propagate in the direction sub-perpendicular to the surface of the preexisting cracks (see Fig. 4.24a). Due to the further compressive loading, the inner wing cracks propagate towards each other and coalesce at the shear zone (see Fig. 4.24b). As shown in Fig. 4.24e, the simulated wing crack initiation angles do not agree with the experimental observations (see Fig. 4.24c). With a significant load increase, the outer wing cracks start to propagate (see Fig. 4.24d).

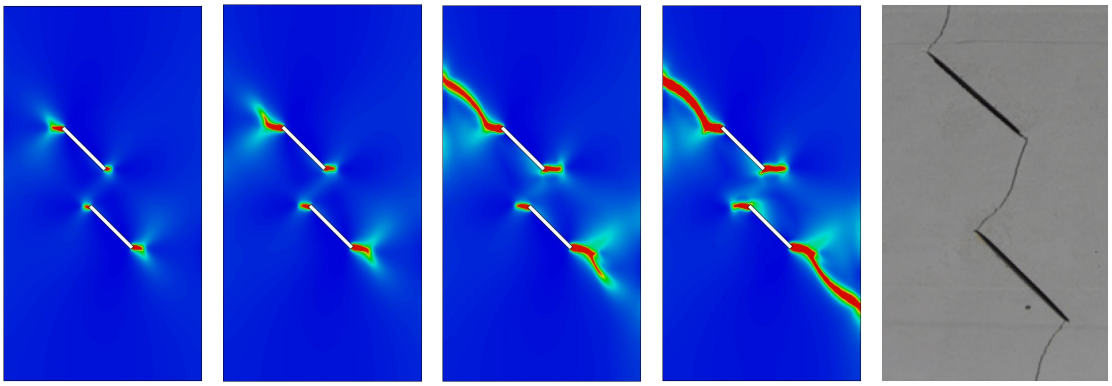

(a) $\overline{\mathbf{u}} = 0.28\,\mathrm{mm}$ **(b)** $\overline{\mathbf{u}} = 0.31\,\mathrm{mm}$ **(c)** $\overline{\mathbf{u}} = 0.34\,\mathrm{mm}$ **(d)** $\overline{\mathbf{u}} = 0.37\,\mathrm{mm}$ **(e)** experiment

Figure 4.23: Crack evolution process predicted by the volumetric/deviatoric split in case of $\gamma = 68°$.

Crack propagation in case of $\gamma = 90°$

Fig. 4.25 presents the crack evolution process predicted by the isotropic model, as well as experimental results for the geometry in case of $\gamma = 90°$. For this case, the evolution of the crack phase-field (see Figs. 4.25a to 4.25c) is similar to that in case of $\gamma = 68°$ (see Fig. 4.21) except for the secondary crack evolution (see Fig. 4.25d). As

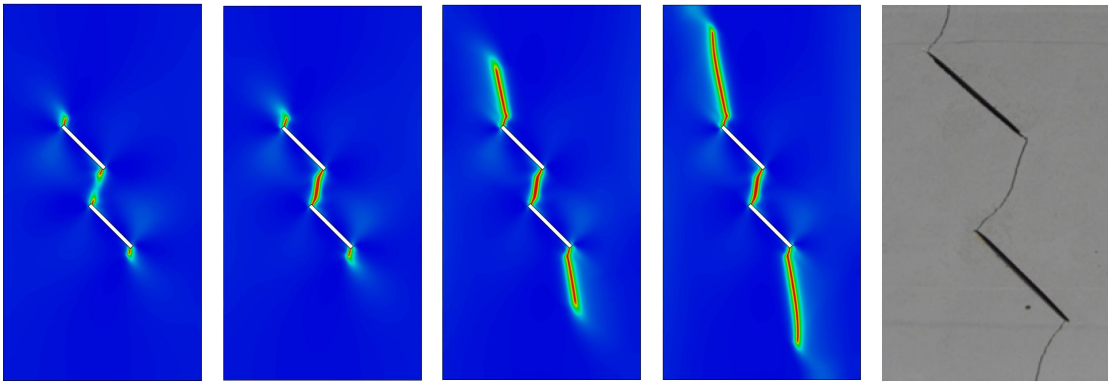

(a) $\overline{\mathbf{u}} = 0.56\,\mathrm{mm}$ **(b)** $\overline{\mathbf{u}} = 0.57\,\mathrm{mm}$ **(c)** $\overline{\mathbf{u}} = 0.63\,\mathrm{mm}$ **(d)** $\overline{\mathbf{u}} = 0.67\,\mathrm{mm}$ **(e)** experiment

Figure 4.24: Crack evolution process predicted by the hybrid model in case of $\gamma = 68°$.

shown in Fig. 4.25c, after a relatively stable evolution of wing cracks, a strong shear zone forms between the inner tip of one preexisting crack and the front of one wing crack (see Fig. 4.25d). The simulated results cannot be identified experimentally (see 4.25e)

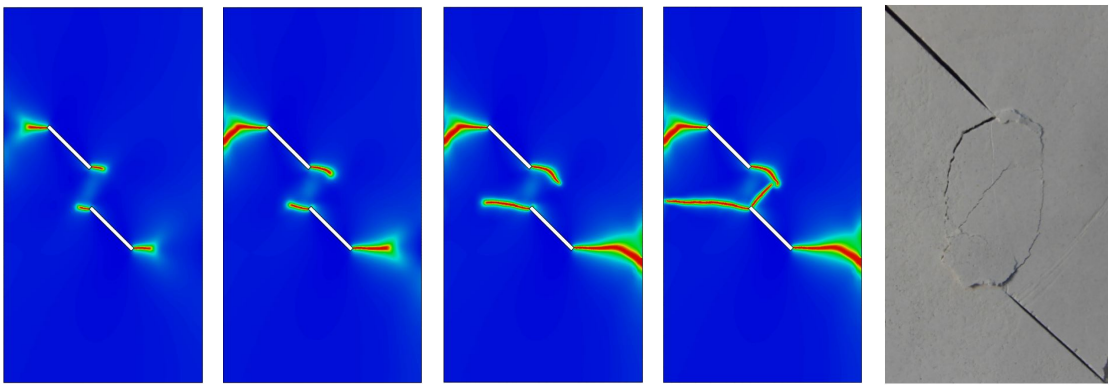

(a) $\overline{\mathbf{u}} = 0.23\,\mathrm{mm}$ **(b)** $\overline{\mathbf{u}} = 0.26\,\mathrm{mm}$ **(c)** $\overline{\mathbf{u}} = 0.38\,\mathrm{mm}$ **(d)** $\overline{\mathbf{u}} = 1.36\,\mathrm{mm}$ **(e)** experiment

Figure 4.25: Crack evolution process predicted by the isotropic model in case of $\gamma = 90°$.

Fig. 4.26 presents the crack evolution process predicted by the spectral split, as well as experimental results for the geometry in case of $\gamma = 90°$. For this case, the propagation of wing cracks is similar to that in case of $\gamma = 68°$ (see Fig. 4.22), but the type of crack coalescence differs significantly. At the early stage of the fracturing pro-

cess, the crack propagates in a curvature manner and gradually turns to the direction of the loading. After a considerable propagation of wing cracks (see Fig. 4.26c), the further loading results in appearance of a secondary crack. After that, the secondary crack propagates towards the front of the inner wing crack tip (see Fig. 4.26d). Crack patterns obtained from the numerical tests do not agree with the experimental results (see Fig. 4.26e).

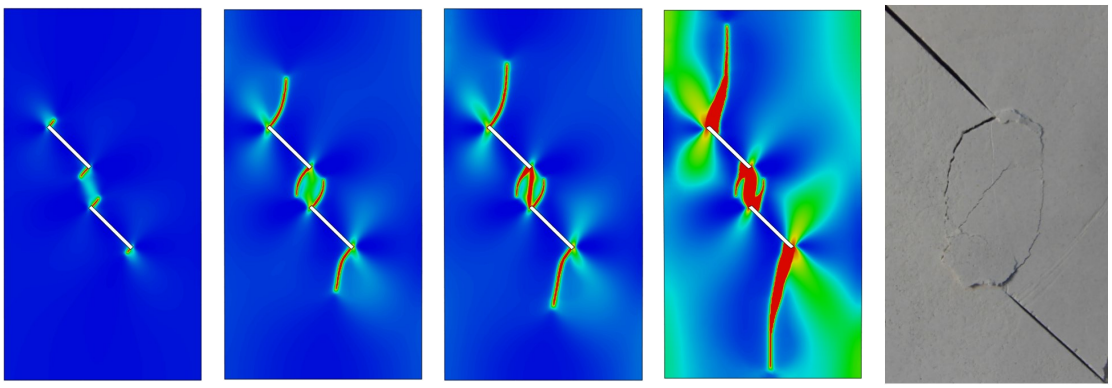

(a) $\overline{\mathbf{u}} = 0.50\,\mathrm{mm}$ **(b)** $\overline{\mathbf{u}} = 0.81\,\mathrm{mm}$ **(c)** $\overline{\mathbf{u}} = 0.88\,\mathrm{mm}$ **(d)** $\overline{\mathbf{u}} = 1.40\,\mathrm{mm}$ **(e)** experiment

Figure 4.26: Crack evolution process predicted by the spectral split in case of $\gamma = 90°$.

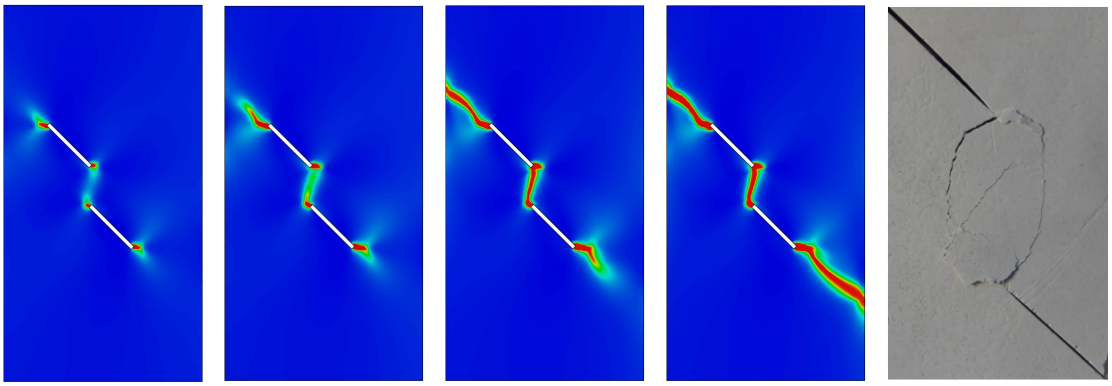

(a) $\overline{\mathbf{u}} = 0.27\,\mathrm{mm}$ **(b)** $\overline{\mathbf{u}} = 0.29\,\mathrm{mm}$ **(c)** $\overline{\mathbf{u}} = 0.30\,\mathrm{mm}$ **(d)** $\overline{\mathbf{u}} = 0.32\,\mathrm{mm}$ **(e)** experiment

Figure 4.27: Crack evolution process predicted by the volumetric/deviatoric split in case of $\gamma = 90°$.

Fig. 4.27 presents the crack evolution process predicted by the volumetric/deviatoric split, as well as experimental results for the geometry in case of $\gamma = 90°$. The process

of crack initiation and propagation is similar to that in case of $\gamma = 68°$ (see Fig. 4.23). As shown in Fig. 4.27c, the further loading results in the formation of a strong shear zone in ligament region. Two secondary cracks propagate towards each other, and finally get connected (see Fig. 4.27d). The numerical results are not in agreement with the experimental results (see Fig. 4.27e).

Fig. 4.28 presents the crack evolution process predicted by the hybrid model, as well as experimental results for the geometry in case of $\gamma = 90°$. For this case, crack coalescence (see Figs. 4.28a to 4.28c) is similar to that in the previous case (see Fig. 4.24). Due to the further compressive loading, strong shear stress zones arise in front of the outer wing cracks (see Fig. 4.28d). After that, secondary cracks initiate and propagate in these strong shear stress zones. The simulated crack patterns cannot be confirmed experimentally as shown in Fig. 4.28e.

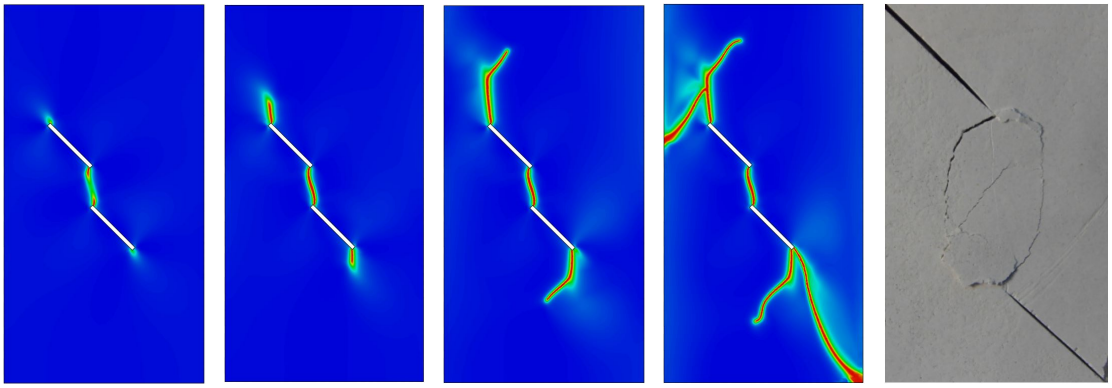

(a) $\overline{\mathbf{u}} = 0.45\,\mathrm{mm}$ **(b)** $\overline{\mathbf{u}} = 0.58\,\mathrm{mm}$ **(c)** $\overline{\mathbf{u}} = 0.66\,\mathrm{mm}$ **(d)** $\overline{\mathbf{u}} = 1.10\,\mathrm{mm}$ **(e)** experiment

Figure 4.28: Crack evolution process predicted by the hybrid model in case of $\gamma = 90°$.

5

Phase-field modelling of brittle fracture in anisotropic materials under tensile loadings

This chapter deals with application of the phase-field method to simulate the fracturing processes in anisotropic materials under tensile loadings. First of all, we investigate the effects of the penalty factor β and material orientation α on crack paths in

Mechanical	**Value**	**Unit**
Elastic moduli $\underline{C}_{11}$	565 000	MPa
Elastic moduli $\underline{C}_{12}$	501 000	MPa
Elastic moduli $\underline{C}_{22}$	95 000	MPa
Elastic moduli $\underline{C}_{44}$	169 000	MPa
Phase-field	**Value**	**Unit**
Crack width κ	0.005	mm
Stiffness resistance η	1.0×10^{-6}	-
Fracture toughness $\mathscr{G}_c$	0.02	N/mm

Table 5.1: Parameters used in the phase-field modelling of brittle fracture in anisotropic materials under tensile loadings (Silicon carbide [93])

anisotropic solids. Further on, simulations of inter- and transgranular fracture in polycrystalline materials are performed, and the numerical results are analyzed.

The initial crack is modelled as a geometric notch [114]. The phase-field model for anisotropic fracture has been implemented into a fully integrated four-node quadrilateral element. Plane strain condition is assumed. The input parameters are listed in Table 5.1.

5.1 Crack evolution in a sole material

In this example, simulations of anisotropic crack evolution in a specimen containing an initial crack are performed. The geometry and boundary conditions of the notched specimen are plotted in Fig. 5.1. The complete top edge is moved by a vertical displacement. The spatial domain is discretized by 21702 four-node quadrilateral elements with an effective element size $h = 0.005\,\mathrm{mm}$. The diffuse parameter κ is given as $0.005\,\mathrm{mm}$. The displacement increment is set as $\overline{\mathbf{u}} = 1.0 \times 10^{-6}\,\mathrm{mm}$ during the stable crack propagation.

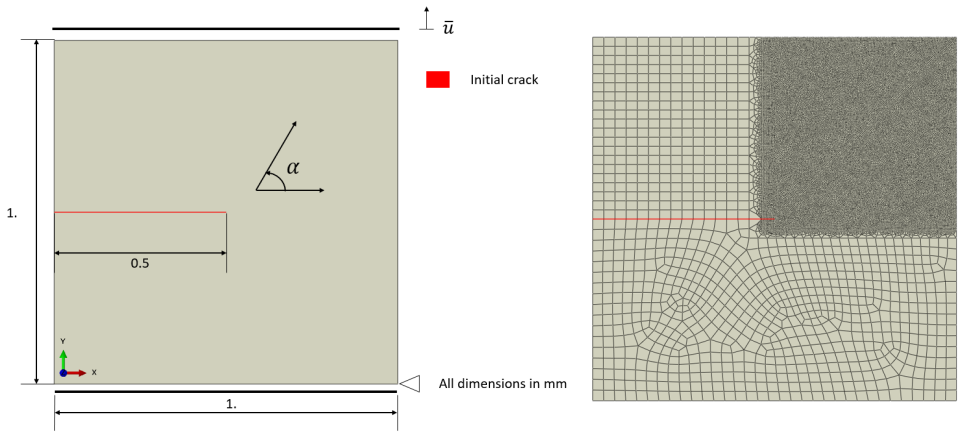

Figure 5.1: Geometry and boundary conditions of the single-edge notched tension test (left); Finite element discretization (right)

Variation of the penalty factor β

First, the effects of the penalty factor β are investigated. The material orientation is fixed at $\alpha = 45°$. The penalty factor β is varied in a range from 0 to 50. Fig. 5.2 presents the simulated crack paths for different penalty factors β. The crack propagates as expected in a horizontal direction in case of isotropic fracture $\beta = 0$. It can be observed that the crack path has been changed in case $\beta \neq 0$. For $0 < \beta < 1$, β almost has no influence on the crack orientation. For $\beta > 1$, the crack orientation is strongly influenced by β and it converges to the pre-defined material orientation α by increasing β. The results show that the crack orientation in anisotropic materials is significantly dependent on the chosen value of the penalty factor β.

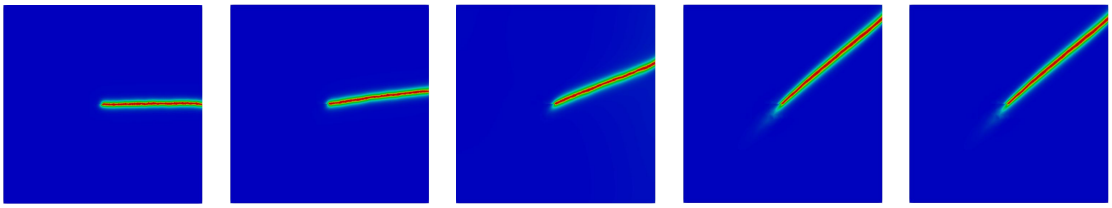

(a) $\beta = 0$ **(b)** $\beta = 1$ **(c)** $\beta = 5$ **(d)** $\beta = 20$ **(e)** $\beta = 50$

Figure 5.2: Influence of the penalty factor β on the direction of the crack path.

Variation of the material orientation α

In order to investigate the influence of the material orientation α on crack paths in anisotropic materials, the penalty factor is fixed at $\beta = 50$. The resulting crack paths obtained from different material orientations α are shown in Fig. 5.3. For $\alpha = 0°$ (see Fig. 5.3a) up to $\alpha = 60°$ (see Fig. 5.3d) the crack follows the pre-defined material orientation. However, if we choose $\alpha = 70°$ (see Fig. 5.3e) or even higher (see Fig. 5.3f - Fig. 5.3h), the resulting crack path is no longer in alignment with the pre-defined material orientation. It rather follows the opposite direction with fluctuating crack paths (see Fig. 5.3e-Fig. 5.3g) and finally results in a diffuse horizontally aligned crack for $\alpha = 90°$ (see Fig. 5.3h). Also Bleyer & Alessi [37] have already shown this phenomena exclusively in case of $\alpha = 90°$. However, the reason for these findings is until now not clarified, neither analytically nor experimentally, and has to be investigated in future studies.

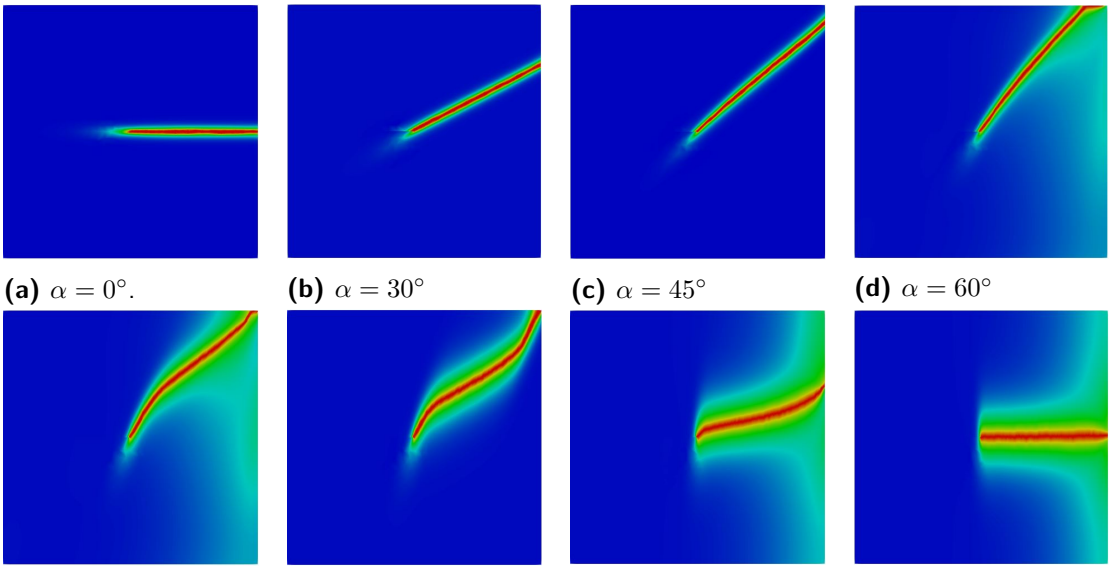

(a) $\alpha = 0°$. **(b)** $\alpha = 30°$ **(c)** $\alpha = 45°$ **(d)** $\alpha = 60°$

(e) $\alpha = 70°$ **(f)** $\alpha = 75°$ **(g)** $\alpha = 85°$ **(h)** $\alpha = 90°$

Figure 5.3: Influence of material orientation α on the crack path.

5.2 Crack evolution in a bi-material

The purpose of this example is to demonstrate the potential of the developed phase-field model to simulate trans- and intergranular fracture in a bi-material, and analyze how cracks propagate along the material boundary. Fig. 5.4 shows the geometry and boundary conditions of the notched specimen containing two different oriented materials. Moreover, the diffuse length $\kappa = 0.005\,\text{mm}$, the penalty factor $\beta = 50$, and 49888 four-node quadrilateral elements with an effective element size $h = 0.005\,\text{mm}$ are used. The material parameters are listed in Table 5.1. The material orientation in material 1 is given as $\alpha_1 = 45°$, and the material orientation in material 2 is varied in a range from $\alpha_2 = 60°$ to $\alpha_2 = -60°$. Fig. 5.5 illustrates that, except for $\alpha_2 = -60°$ (see Fig. 5.5e), all configurations lead to a transgranular fracture. After the crack crosses the material boundary, the crack follows the direction that correlates to α. It can also be observed that each material orientation only influences the crack direction in its own material domain. On the contrary, for the case $\alpha_2 = -60°$ (see Fig. 5.5e), the material orientation is lower than the angle between the material boundary and x-coordinates, and the result is that the crack crosses nearly the material boundary. In other words, the intergranular fracture behavior is strongly influenced by grain boundary orientations.

5.3 Crack evolution in polycrystalline materials

To demonstrate the capability of the developed model for predicting anisotropic brittle fracture in polycrystalline materials [190], crack initiation and propagation in a polycrystalline structure with $10\,\text{mm} \times 10\,\text{mm}$ domain consisting of an initial crack and 10 grains in uniaxial tension is simulated. The geometry and boundary conditions of the polycrystalline structure are shown in Fig. 5.6.

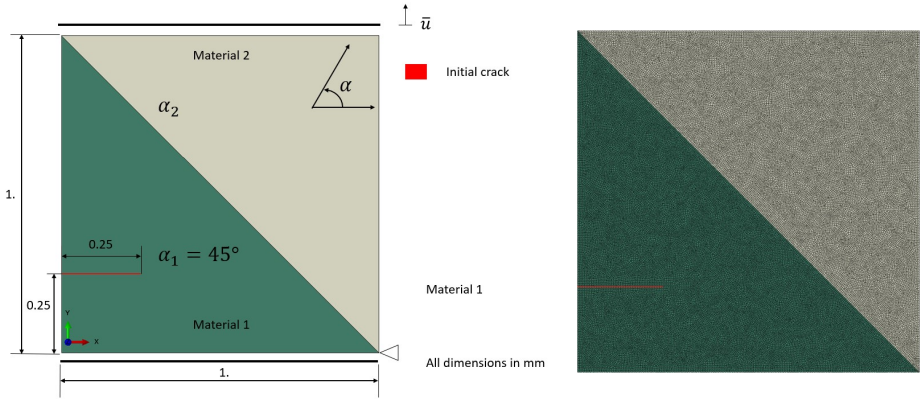

Figure 5.4: Geometry and boundary conditions of the notched specimen containing two different oriented materials subjected to tension (left); Finite element discretization (right).

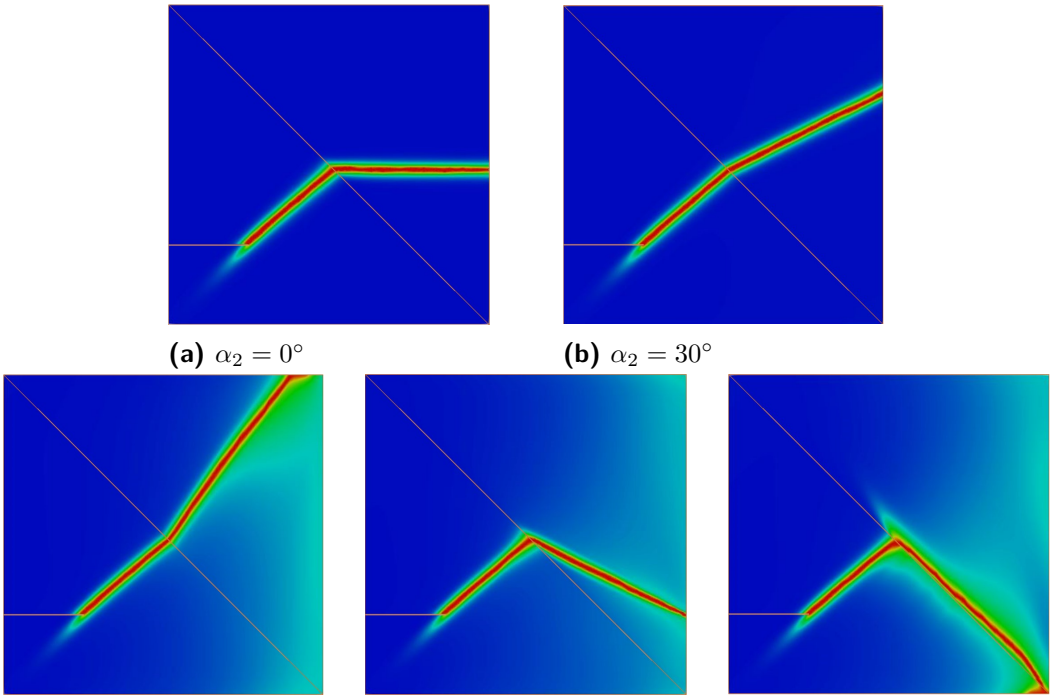

(a) $\alpha_2 = 0°$ **(b)** $\alpha_2 = 30°$

(c) $\alpha_2 = 60°$ **(d)** $\alpha_2 = -30°$ **(e)** $\alpha_2 = -60°$

Figure 5.5: Influence of crack orientation θ on crack paths.

The geometry of this microstructure is generated using the open source software Voronoi [20]. Each grain is associated with a randomly material orientation as depicted in Fig. 5.6. The material parameters are listed in Table 5.1. The unstructured mesh consists of 60622 four-node quadrilateral elements with an effective element size $h = 0.05\,\text{mm}$. The diffuse length κ is chosen as $0.05\,\text{mm}$.

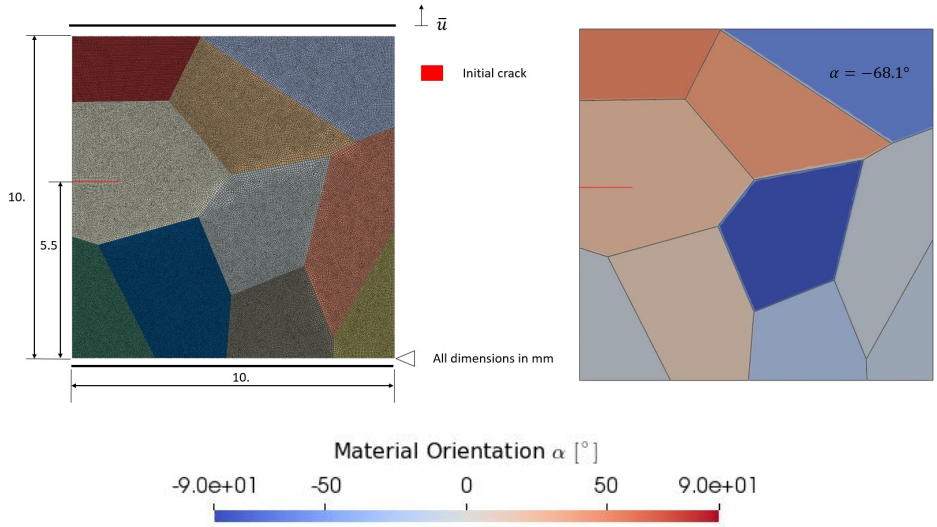

Figure 5.6: Geometry and boundary conditions of the polycrystalline structure containing 10 grains (left); Material orientations (right).

Fig. 5.7 depicts the evolution of the crack phase-field at several failure stages under tensile loadings. In each transgranular fracture system, the direction of crack propagation appears not identical. Fig. 5.7e shows that the crack runs within the grain boundary from the secondary transgranular fracture system, and subsequently propagates into the neighboring grain. A phenomenon for inter- and transgranular fracture can be observed from the results that the direction of crack propagation is strongly dependent on the material orientation in each transgranular fracture system. The intergranular fracture will take place mainly when the orientation of grain boundaries resists crack propagation from transgranular fracture systems. The same arrangement of polycrystals is used for another simulation in which the material orientation α in

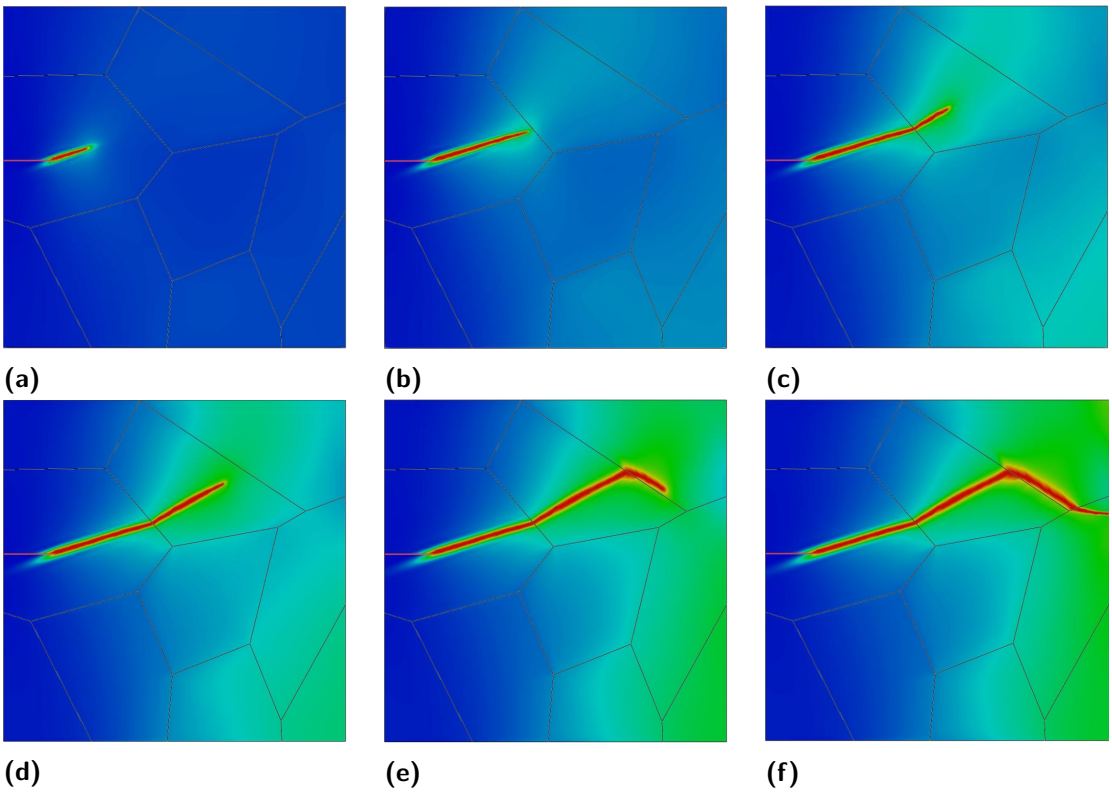

Figure 5.7: Crack phase-field at different failure stages.

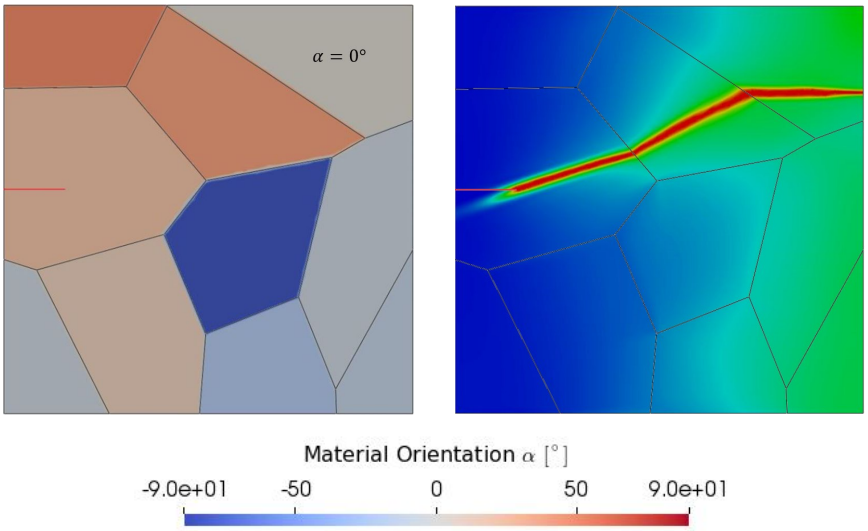

Figure 5.8: Modified material orientations (left); Crack phase-field at the final failure stage (right).

a chosen grain is changed from $-68.1°$ to $0°$ as shown in Fig. 5.8. All other settings remain as before. The impact of this modification is illustrated in Fig. 5.8. It can be observed that the crack propagates nearly horizontally in the modified grain due to the change of material orientation. Obviously, the simulated crack path may be changed by defining a new material orientation for another involved grain. It signifies that the anisotropic properties within each grain can strongly affect the microscopic crack propagation. Hence, for a detailed investigation of such cracks the anisotropic properties should be taken into account.

6

Phase-field modelling of thermoelastic fracture in polycrystalline materials

In this chapter, several numerical examples to demonstrate the capability of modelling thermoelastic crack evolution in anisotropic solids are provided. These include thermoelastic fracture in a sole material, in a bi-material and in a multi-layered material, as well as in polycrystalline materials. Moreover, the effects of grain size on the fracture behavior in polycrystalline materials are investigated.

Mechanical	**Value**	**Unit**
Elastic moduli $\underline{C}_{11}$	565 000	MPa
Elastic moduli $\underline{C}_{12}$	501 000	MPa
Elastic moduli $\underline{C}_{22}$	95 000	MPa
Elastic moduli $\underline{C}_{44}$	169 000	MPa
Thermal	**Value**	**Unit**
Density ρ	3.21×10^{-6}	kg/mm^3
Specific heat capacity c_p	750	J/kgK
Coefficient of thermal conductivity $\underline{k}_{11}$	0.12	W/mmK
Coefficient of thermal conductivity $\underline{k}_{22}$	0.08	W/mmK
Coefficient of thermal expansion $\underline{\alpha}_{T,11}$	4.46×10^{-6}	1/K
Coefficient of thermal expansion $\underline{\alpha}_{T,22}$	4.06×10^{-6}	1/K
Phase-field	**Value**	**Unit**
Crack width κ	0.1	mm
Stiffness resistance η	1.0×10^{-6}	-
Crack is isolating ζ	1.0	-
Fracture toughness $\mathscr{G}_c$	0.02	N/mm

Table 6.1: Parameters used in the phase-field modelling of thermoelastic fracture in polycrystalline materials (Silicon carbide [93])

6.1 Thermoelastic fracture in a sole material

In this example, the proposed model is applied to simulate thermoelastic crack propagation in a rectangular specimen of width 7.5 mm and height 20 mm with an intial crack of 2.5 mm.

The details of the geometry and boundary conditions of the specimen are plotted in Fig. 6.1. Both ends of the specimen are fixed in y-direction, and all other edges are free. The specimen is discretized by 17346 four-node quadrilateral elements with an effective element size $h = 0.05$ mm as shown in Fig. 6.1. The initial temperature of the specimen is 273.5 K, and the temperature of the bottom edge is held constant at the initial temperature $\theta = 273.5$ K. The temperature of the top edge is decreased from 273.5 K to 203.5 K. The time step is chosen as 0.0005 s during the stable crack

propagation. Plain strain condition is considered [164, 185, 218, 222]. The simulation parameters are presented in Table 6.1. Material orientation is given as $\alpha = -45°$, and the penalty factors β of 0, 1, 5, 20 and 50 are used. The contours of the crack phase-field and the corresponding temperature changes are depicted in Fig. 6.2 and Fig. 6.3, respectively. The undamaged material is plotted in blue while red color indicating the totally damaged material. In case of isotropic fracture ($\beta = 0$), the thermoelastic crack propagates in a horizontal direction as shown in Fig. 6.2a. On the contrary, the anisotropic cracks ($\beta \neq 0$) are not horizontally aligned as plotted in Figs. 6.2b to 6.2e. The cooling treatment leads to contraction and tensile stresses in the specimen, re-

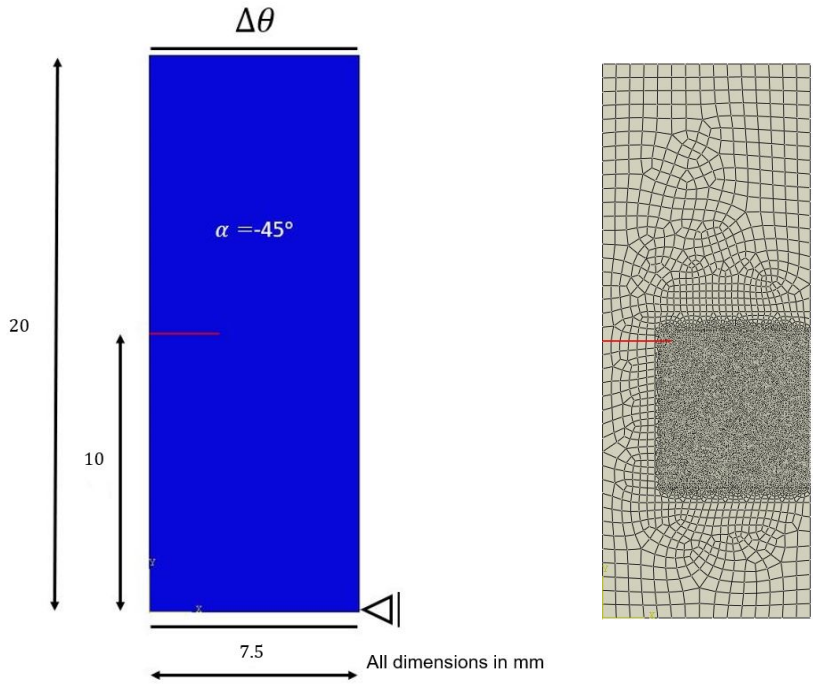

Figure 6.1: Geometry and boundary conditions of the specimen containing an initial crack (left); Finite element discretization (right).

sulting in the evolution of the thermoelastic crack phase-field. Finally, the specimen breaks into two parts.

As shown in Fig. 6.2, when the penalty factor β is chosen sufficiently high (e.g.

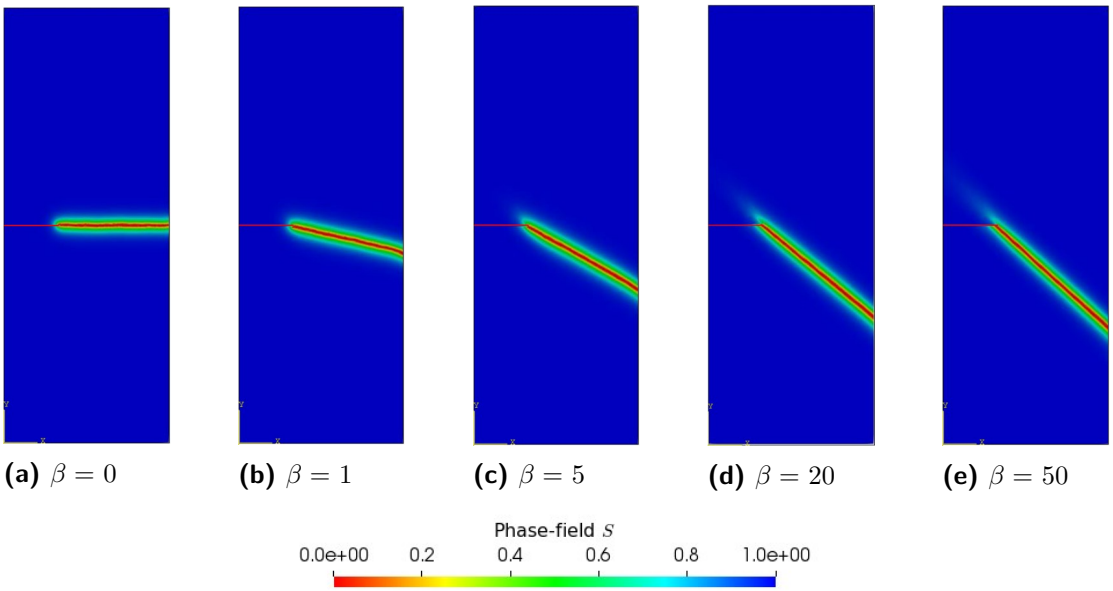

(a) $\beta = 0$ **(b)** $\beta = 1$ **(c)** $\beta = 5$ **(d)** $\beta = 20$ **(e)** $\beta = 50$

Figure 6.2: Influence of the penalty factor β on the direction of crack propagation.

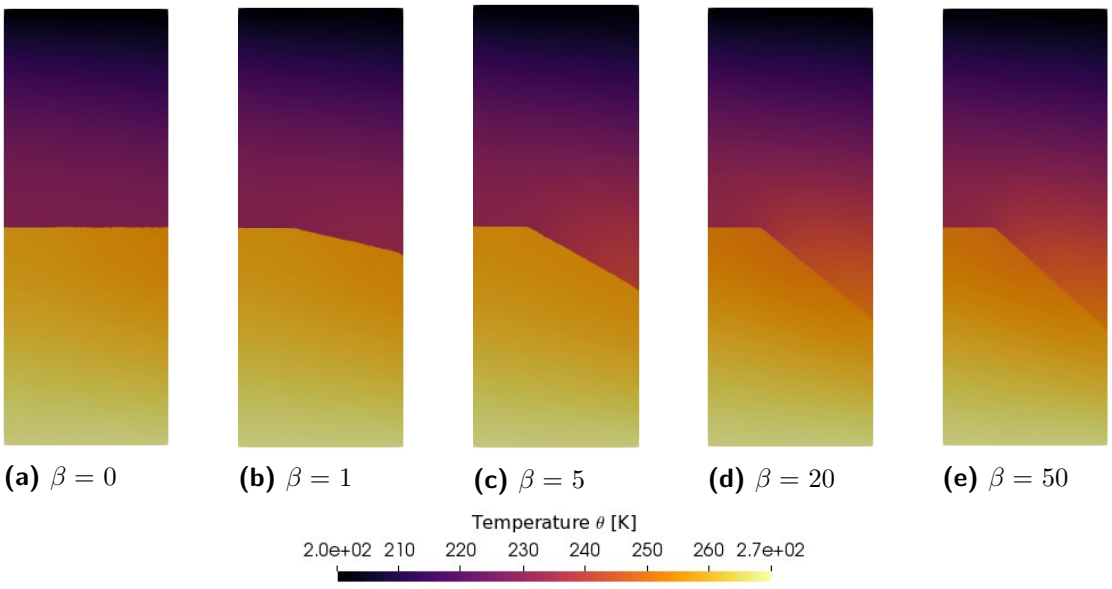

(a) $\beta = 0$ **(b)** $\beta = 1$ **(c)** $\beta = 5$ **(d)** $\beta = 20$ **(e)** $\beta = 50$

Figure 6.3: Influence of the penalty factor β on the temperature field.

$\beta = 20$), the crack will follow the pre-defined material orientation $\alpha = -45°$. Moreover, the crack phase-field is considered as isolating ($\zeta = 1$) so that a noticeable temperature gradient along the direction of crack growth can be observed in Fig. 6.3.

This example demonstrates the capability of the proposed model for simulating thermoelastic crack evolution in a sole material.

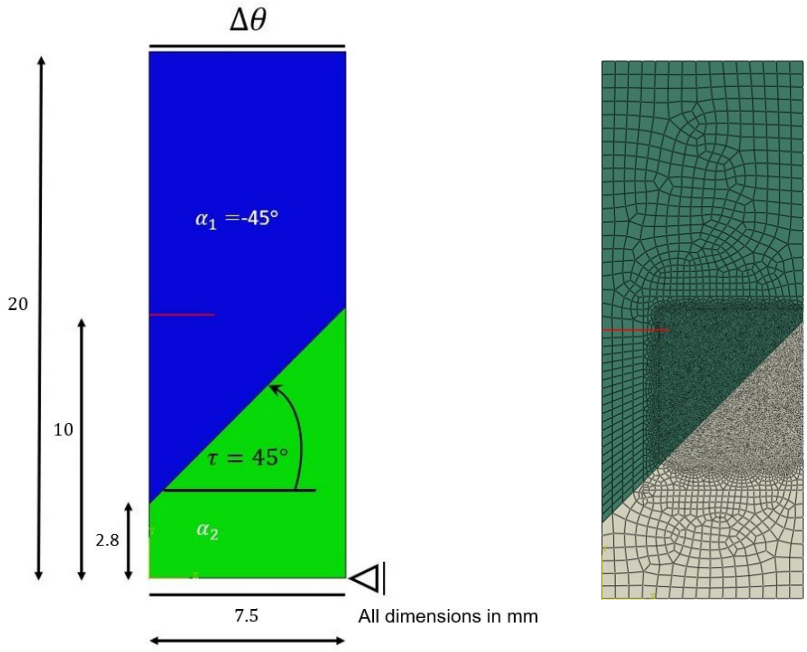

Figure 6.4: Geometry and boundary conditions of the notched specimen containing two different oriented materials (left); Finite element discretization (right)

6.2 Thermoelastic fracture in a bi-material

The purpose of this example is to demonstrate the potential of the proposed model to simulate the trans- and intergranular fracturing processes under thermomechanical loadings. The specimen consists of two different oriented anisotropic materials. The details of the geometry and boundary conditions of the specimen are plotted in Fig. 6.4. The specimen is discretized by 17825 four-node quadrilateral elements, and

the effective element size is chosen as $h = 0.05\,\text{mm}$. Plain strain condition is assumed. The material parameters are the same as those in the previous section. The top and bottom edges are fixed in y direction, and the initial temperature of all nodes of the specimen is $\theta = 273.5\,\text{K}$. The temperature of the top edge is decreased from $273.5\,\text{K}$ to $203.5\,\text{K}$ while keeping the temperature of the bottom edge constant at $273.5\,\text{K}$. Due to the cooling of the top edge, a transient heat transfer in the specimen is obtained. In this example, the material orientation in material 1 is given as $\alpha_1 = -45°$, and the penalty factors β in material 1 and material 2 are chosen as $\beta = 20$. The pre-defined material orientation α in material 2 is varied to investigate its effects on the simulation of anisotropic fracture under thermomechanical loadings. The material orientations α of $0°$, $30°$, $55°$ and $70°$ are used.

The crack phase-field for different material orientations α and the corresponding temperature changes are shown in Figs. 6.5 and 6.6, respectively. Again, red color represents the totally damaged material. In case of $\alpha = 0°$, the thermoelastic crack propagates horizontally in material 2 as shown in Fig. 6.5a. Moreover, in case of $\alpha = 30°$, the direction of crack propagation is the same as the pre-defined material orientation in material 2 (see Fig. 6.5b). Rather than following the material orientation, the thermally induced crack propagates nearly along the material interface in case of $\alpha = 55°$ as plotted in Fig. 6.5c. Similar fracture behavior can be found in case of $\alpha = 70°$, too. Both inter- and transgranular thermoelastic cracks are observed in the simulation. The results clearly demonstrate that, when the orientation of material interface ($\tau = 45°$) is lower than the material orientation (material 2: $\alpha = 55°$), the thermoelastic crack will take place at the material interface.

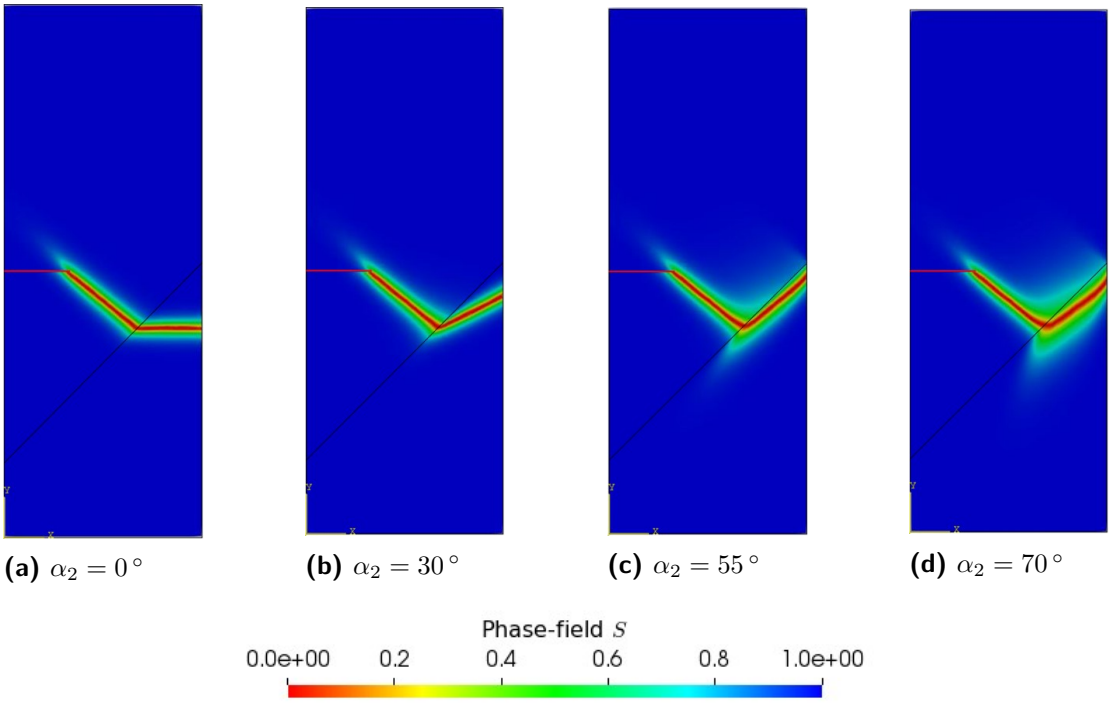

(a) $\alpha_2 = 0\,^\circ$ **(b)** $\alpha_2 = 30\,^\circ$ **(c)** $\alpha_2 = 55\,^\circ$ **(d)** $\alpha_2 = 70\,^\circ$

Figure 6.5: Influence of material orientation α on the crack path.

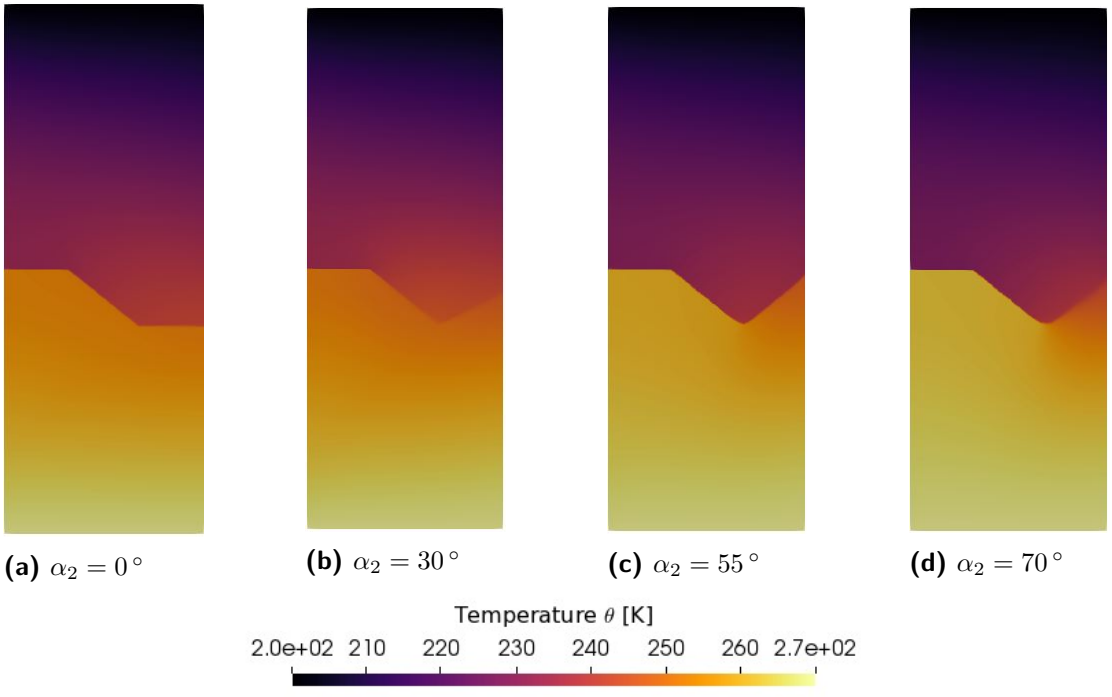

(a) $\alpha_2 = 0\,^\circ$ **(b)** $\alpha_2 = 30\,^\circ$ **(c)** $\alpha_2 = 55\,^\circ$ **(d)** $\alpha_2 = 70\,^\circ$

Figure 6.6: Influence of material orientation α on the temperature field.

6.3 Thermoelastic fracture in a multi-layered material

In this section, simulations of the thermoelastic crack growth in a multi-layered material are performed. Fig. 6.7 shows the geometry size and boundary conditions of the notched multi-layered specimen of width 10 mm and height 20 mm with an initial crack of 2.5 mm. Moreover, each layer has its own material orientation ($\alpha_1 = -45°$ for the left layer, $\alpha_2 = 45°$ for the middle layer and $\alpha_3 = -45°$ for the right layer). Material parameters are listed in Table 6.1.

The multi-layered specimen is refined in the areas where the thermoelastic fracture is expected to develop. The effective mesh size is chosen as 0.05 mm, and 47808 four-node quadrilateral elements are used as shown in Fig. 6.7.

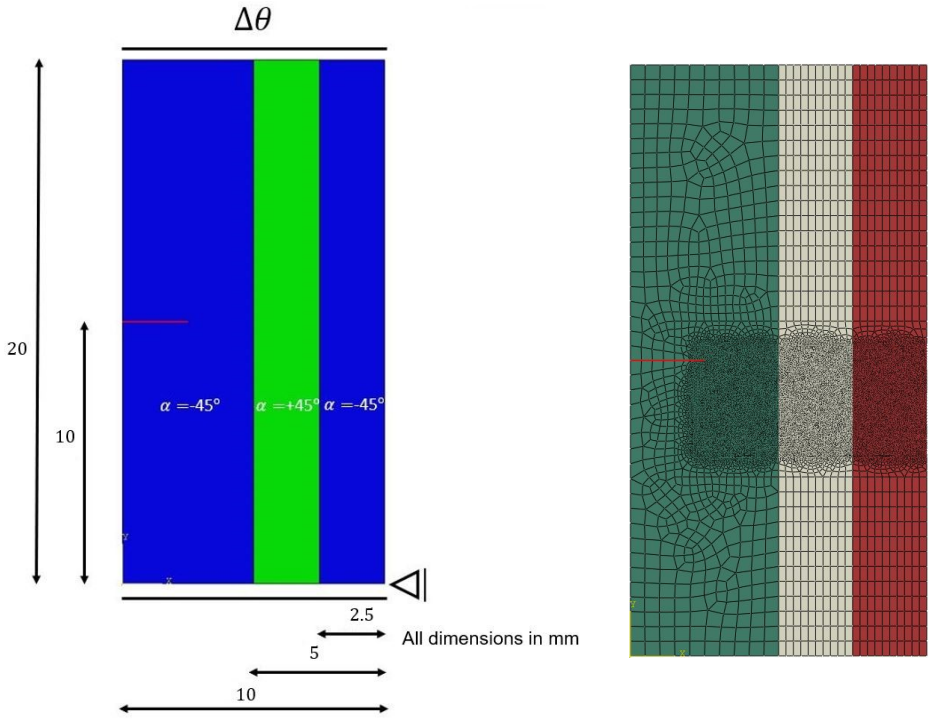

Figure 6.7: Geometry and boundary conditions of the multi-layered specimen (left); Finite element discretization (right)

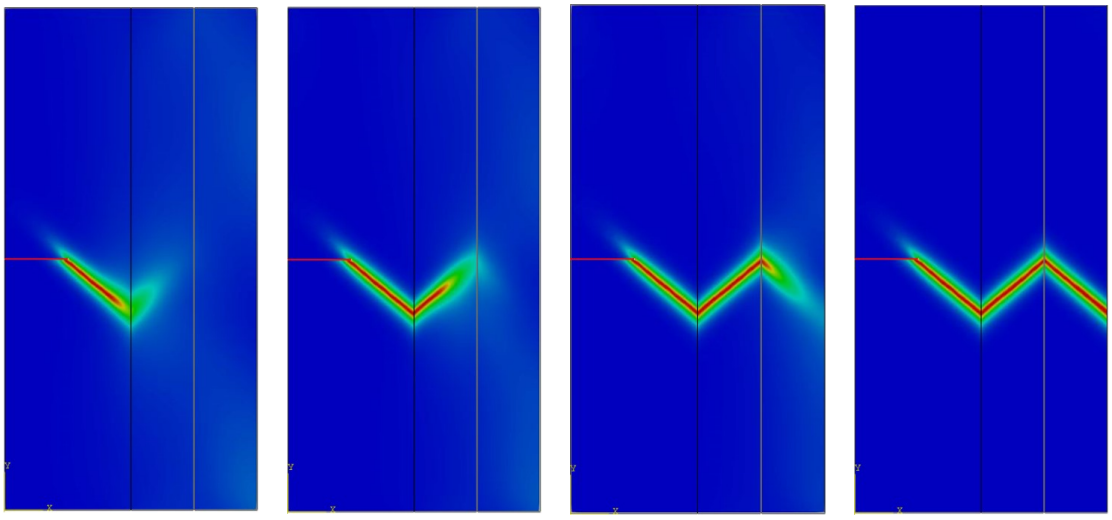

Figure 6.8: Crack evolution process in the notched multi-layered specimen

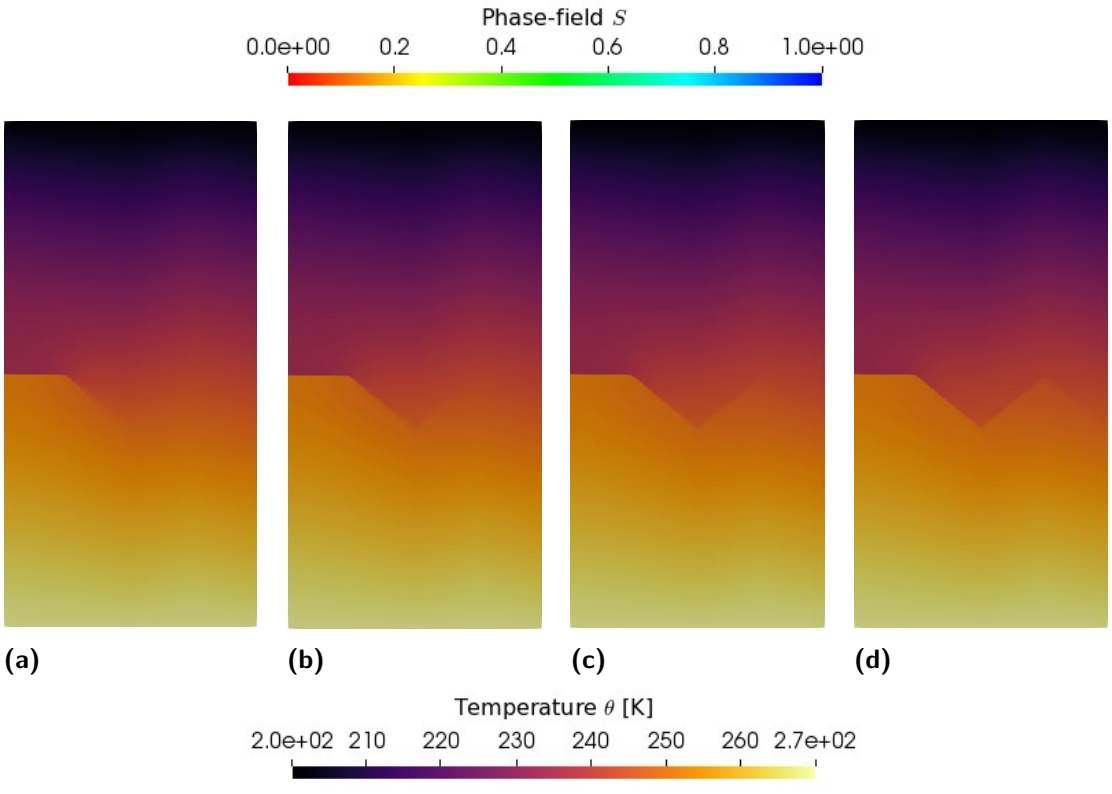

Figure 6.9: Temperature changes at different failure stages.

The specimen is subjected to an initial temperature of 273.5 K. The temperature field is decreased at the top edge by $\Delta\theta = 70\,\mathrm{K}$ while the temperature of the bottom edge remains unchanged (the initial temperature of 273.5 K). The time step is given as 0.0005 s during the stable thermoelastic crack propagation. The crack first initiates in the left layer as shown in Fig. 6.8a. Due to further cooling, the crack starts to propagate in the middle layer (see Fig. 6.8b). Because the penalty factor $\beta = 20$ is chosen sufficiently high, the thermoelastic crack follows the pre-defined material orientation in each layer (see also the discussion in Sect. 6.1).

Finally, the specimen is separated into pieces with inhomogeneous temperature distributions as shown in Fig. 6.9.

6.4 Thermoelastic fracture in polycrystalline materials

6.4.1 Thermoelastic fracture in 40 grains

The purpose of this example is to demonstrate the capability of modelling crack evolution in polycrystalline materials under thermomechanical loadings. Fig. 6.10 shows the details of the geometry and boundary conditions of a polycrystalline structure of width 10 mm and height 20 mm with an initial crack of 1 mm. This microstructure containing 40 grains is generated using open source software Voronoi [20], and is discretized by 54431 four-node quadrilateral elements with an effective element size $h = 0.05\,\mathrm{mm}$ as plotted in Fig. 6.10. The polycrystalline structure is refined in the areas where the thermoelastic crack is expected to propagate. The diffuse length κ is chosen as 0.05 mm. The penalty factor is chosen as $\beta = 20$. Plane strain condition is considered [164, 185, 218, 222].

The initial temperature of all nodes in this microstructure is 273.5 K, and the temperature of the bottom edge is held constant at the initial temperature 273.5 K. The

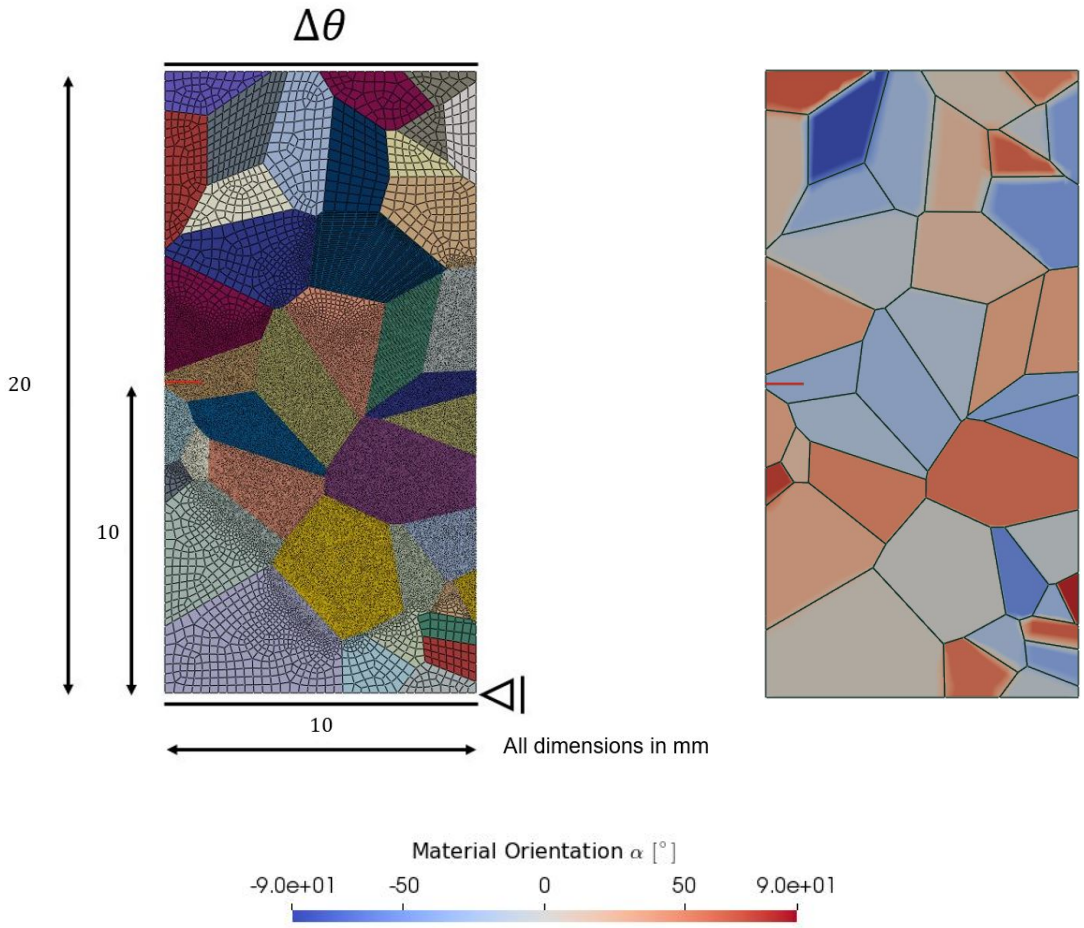

Figure 6.10: Geometry, boundary conditions and finite element discretization of the polycrystalline structure containing 40 grains (left); Material orientations (right)

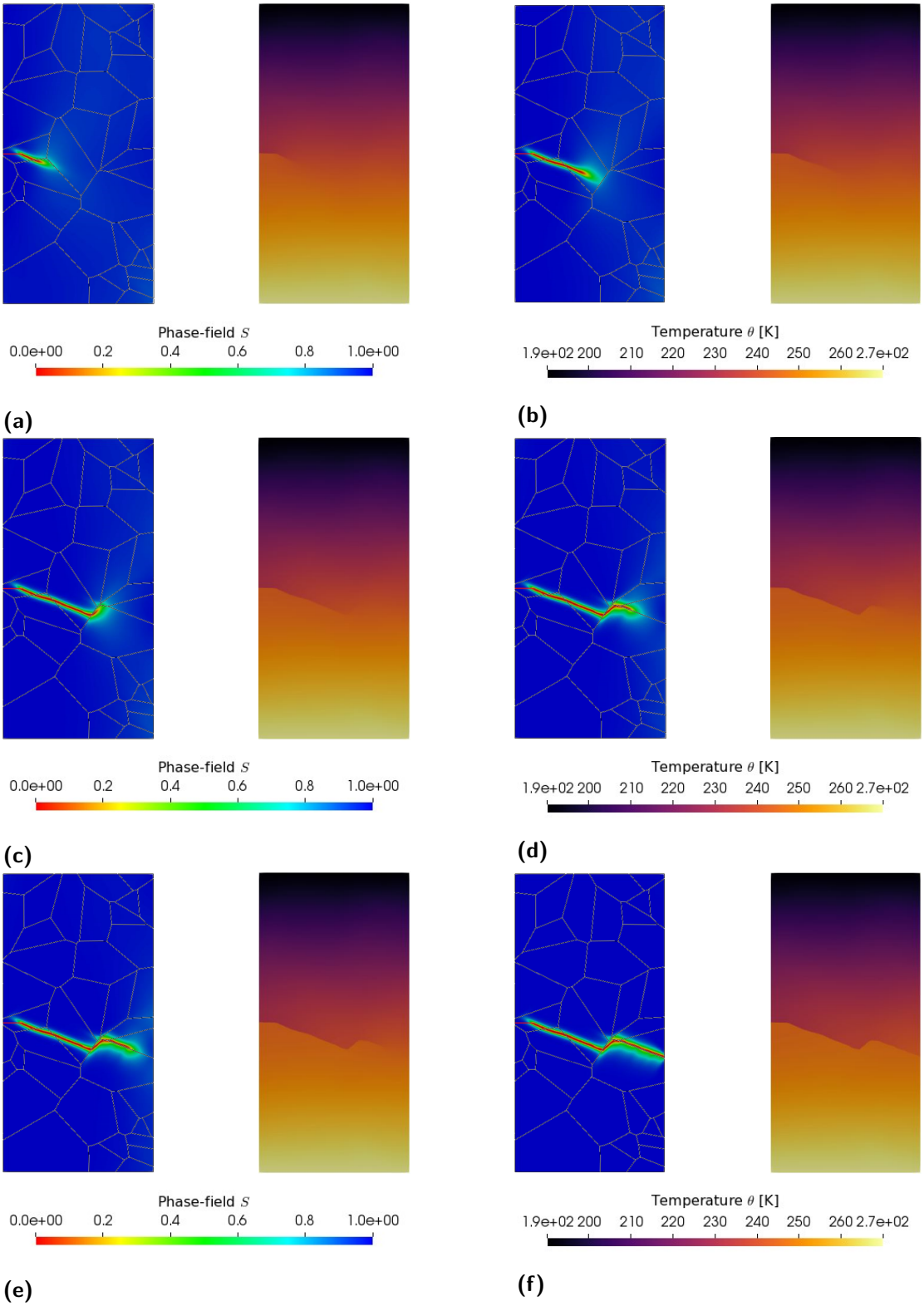

Figure 6.11: Crack phase-field at different failure stages with the corresponding temperature changes in case of 40 grains.

cooling process is achieved by a Dirichlet type control of the temperature field at the top edge. The temperature of the top edge is decreased from 273.5 K to 193.5 K. Such a cooling-induced contraction yields high tensile stresses in polycrystalline materials. Once thermally induced tensile stress exceeds the critical value, the crack starts to propagate.

Fig. 6.11 shows the contours of the crack phase-field at different failure stages. According to the material orientation in the polycrystalline structure, the crack first propagates along the pre-defined material orientation in the grain interior (see Figs. 6.11a and 6.11b). Then, the crack propagates into the neighbouring grain, in which the direction of crack propagation follows the material orientation in the involved grain. However, when the crack comes close to some oriented grains, the crack will run within the grain boundaries (see Figs. 6.11c and 6.11f). Both inter- and transgranular cracks are observed in this simulation.

Fig. 6.11 shows the corresponding temperature changes at different stages of the cooling process. It can be seen that the heat transfer is strongly affected by the crack phase-field.

6.4.2 Thermoelastic fracture in 200 grains

In order to investigate the effects of grain size on the fracture behavior in polycrystalline materials, simulations of the thermoelastic crack initiation and propagation in a polycrystalline structure containing 200 grains are performed. Fig. 6.12 shows the details of the geometry and boundary conditions of this microstructure. Again, the geometry of this microstructure is generated using the open source software Voronoi [20], and the material orientation in each grain is generated randomly. The simulation parameters are the same as those in the above example (see Section 6.4.1). The domain is discretized by 70275 four-node quadrilateral elements with an effective element size

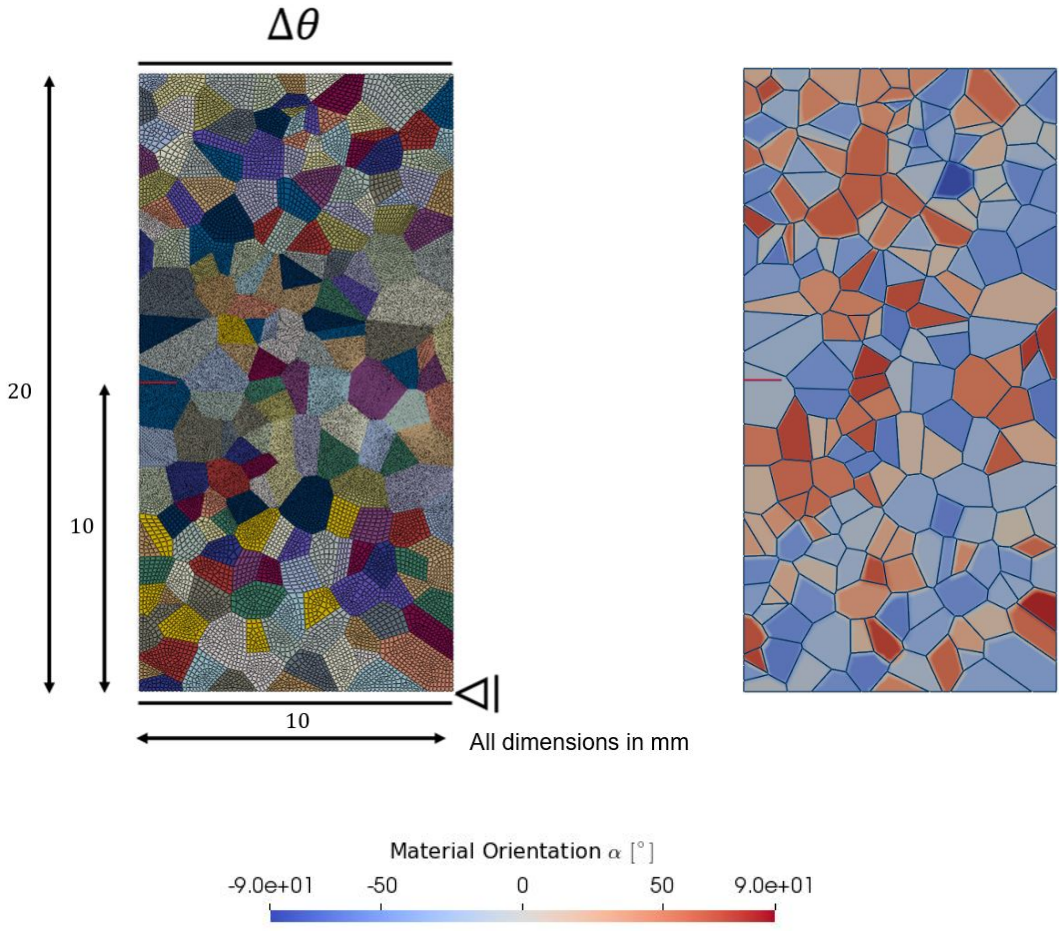

Figure 6.12: Geometry, boundary conditions and finite element discretization of the polycrystalline structure containing 200 grains (left); Material orientations (right)

$h = 0.05\,\text{mm}$ as shown in Fig. 6.12. This microstructure is refined in the areas where the thermoelastic crack is expected to propagate. The top and bottom edges are fixed in y direction, and the initial temperature of all nodes is held at 273.5 K. The cooling process is induced by a prescribed temperature 193.5 K (the corresponding temperature difference is 80 K) at the top edge, while the temperature of the bottom edge remains constant at the initial temperature of 273.5 K. The time step is set as 0.0005 s during the stable thermoelastic crack propagation.

Fig. 6.13 shows the contours of the crack phase-field and the corresponding temperature changes at different failure stages. Blue and red colors correspond to the undamaged and the broken materials, respectively. Due to the cooling of the top edge, high tensile stresses arise in this microstructure, leading to the thermoelastic crack evolution. Fig. 6.13a shows that the crack is first derived from the notch. After that, the crack develops within the grain interior (see Fig. 6.13b). Due to further cooling, the crack propagates along the grain boundaries, which is dependent on the orientations of the grain boundaries and neighbouring grains (see Fig. 6.13e). An interesting point in this simulation is that, crack growth in the grain interior is often observed (see Fig. 6.13). Thus, a transgranular fracture is promoted in case of 200 grains. Finally, this microstructure breaks into pieces with inhomogeneous temperature distributions as depicted in Fig. 6.13f.

A comparison of these two cases is depicted in Fig. 6.14. Both thermal stress-induced inter- and transgranular fracturing processes can be observed in the phase-field simulations. In case of 200 grains, the thermoelastic crack is less constrained to develop through the grain interior, and a complex (zigzag) crack path is clearly observed.

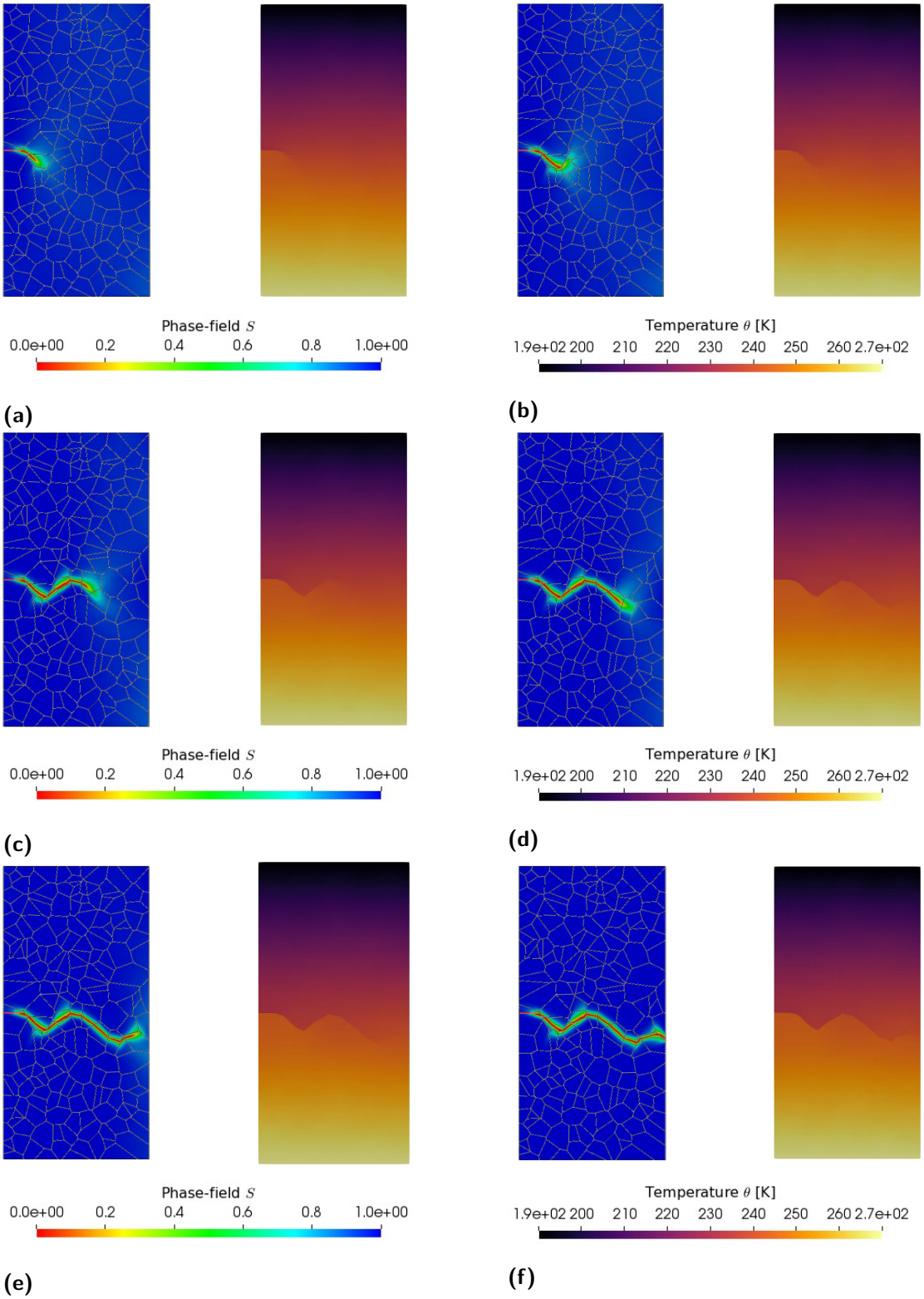

Figure 6.13: Crack phase-field at different failure stages with the corresponding temperature changes in case of 200 grains.

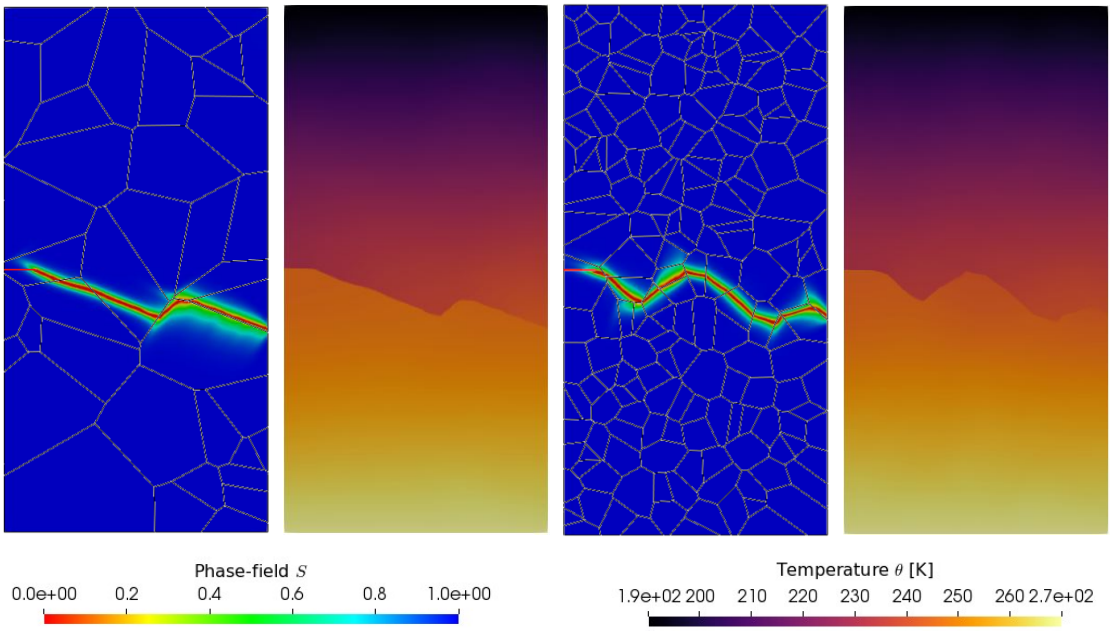

(a) **(b)**

Figure 6.14: Crack phase-field at the final failure stage with the corresponding temperature changes. 40 grains (left); 200 grains (right).

7

Adaptive phase-field modelling of brittle fracture in compression

This section starts with a quasi-static fracture problem, i.e. a single-edge notched shear test. The performances of different refinement strategies [107] on curved fracture problems are investigated. Furthermore, simulations of crack evolution in a PBX 9502 plate specimen with cavity subjected to overall compression are carried out, and the results are discussed in detail. The tests were run on an Intel(R) Core(TM) i7-

4710HQ CPU @ 2.50GHz machine.

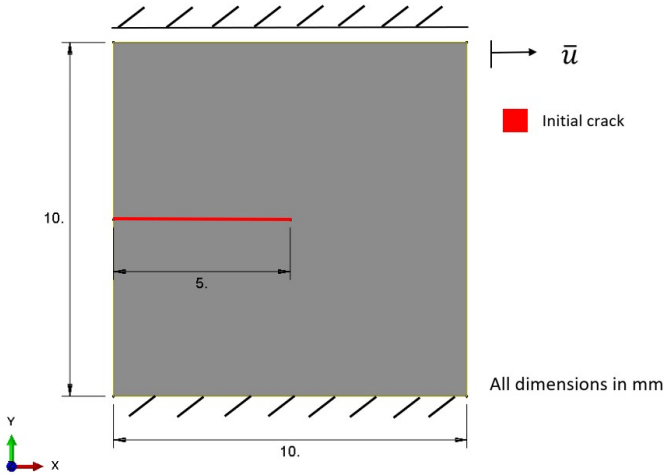

Figure 7.1: Geometry and boundary conditions of the single-edge notched shear test.

7.1 Single notched shear test

In order to demonstrate the capability of the adaptive phase-field model [107] to simulate curved crack propagation in 2D case, the shear test specimen is considered as shown in Fig. 7.1. The material and model parameters used in the simulation are $\lambda = 121\,150\,\text{MPa}$, $\mu = 80\,770\,\text{MPa}$, $\mathscr{G}_c = 2.7\,\text{N/mm}$, $\eta = 1.0 \times 10^{-10}$, and $\kappa = 0.011\,\text{mm}$ [153]. Plane strain condition is assumed. The displacement increment $\Delta u = 0.0001\,\text{mm}$ at each time step is used.

First of all, one of primary tasks in this section is to compare the results obtained from the uniform mesh to different locally refined discretizations for a fixed diffuse scale $\kappa = 0.011\,\text{mm}$. Therefore, four different mesh levels are performed: Case A: 16×16 elements with 3 cycles mesh refinement (with an initial mesh size $h = 0.088\,\text{mm}$), Case B: 32×32 elements with 2 cycles mesh refinement (with an initial mesh size $h = 0.044\,\text{mm}$), Case C: 64×64 elements without mesh refinement (with an initial mesh size $h = 0.022\,\text{mm}$), and Case D: 128×128 elements without mesh refinement

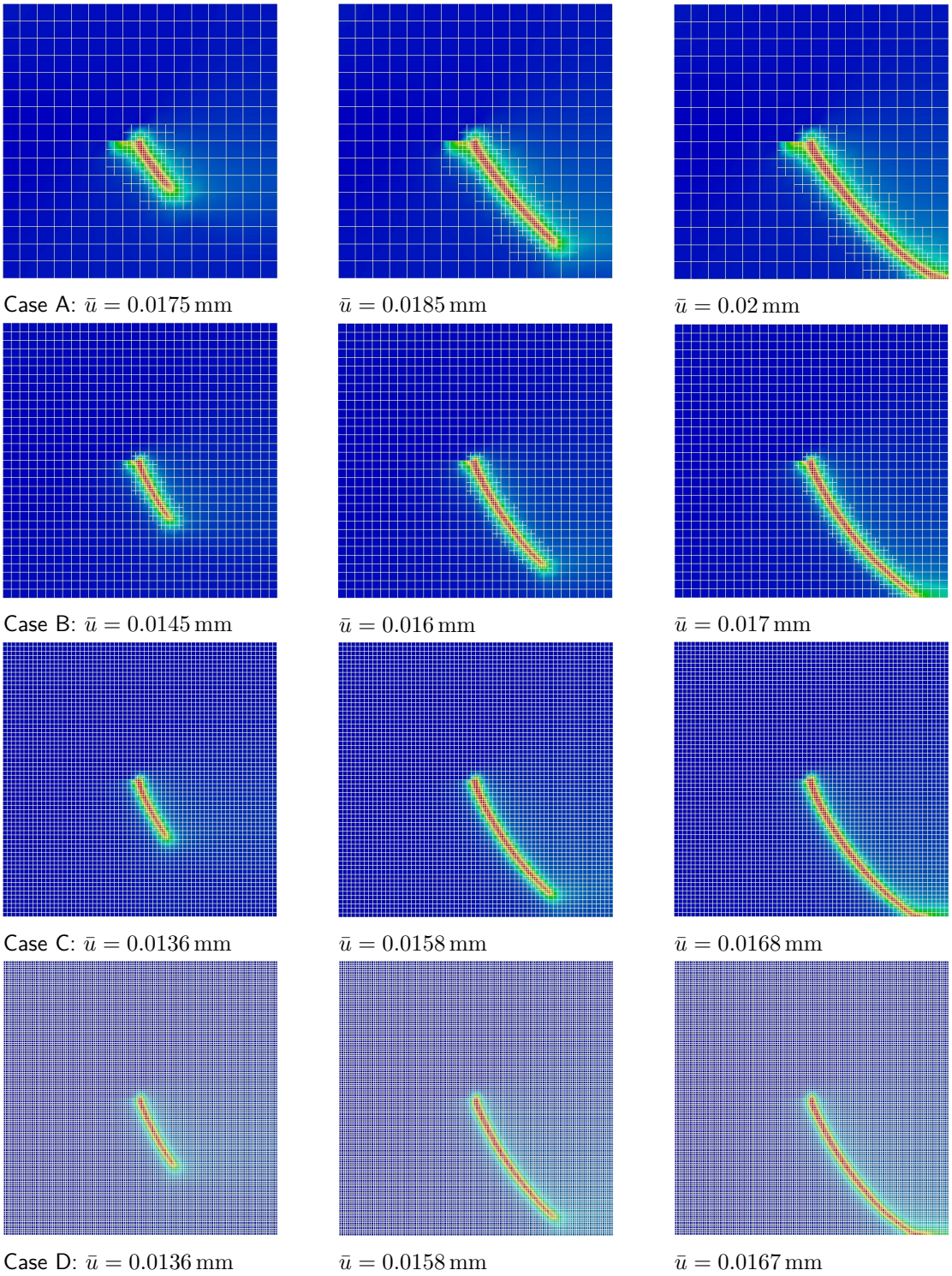

Figure 7.2: Comparison of the crack phase-field for uniformly and iteratively refined meshes.

(with an initial mesh size $h = 0.011\,\text{mm}$). These four different meshes lead to the smallest mesh size $h = 0.011\,\text{mm}$. The threshold for the mesh refinement process $C = 0.2$, is considered for crack propagation over the course of the simulation.

Fig. 7.2 depicts snapshots of the crack phase-field evolution at different displacements and the corresponding displacement-force curves are shown in Fig. 7.3. The following conclusions were drawn from the results. In Fig. 7.2, even though the resulting crack paths are as expected for all cases, a significant difference in the process of the crack phase-field evolution is observed for the initial coarse mesh (Case A Fig. 7.2a). In this case, crack propagation is rather slower than in other cases. This finding is also reflected in Fig. 7.3 where the peak force in Case A shows an overestimated behavior. For all cases, the convergence can be clearly observed as the level of the mesh refinement is increased. In Table 7.1, the number of DOFs and the run time compar-

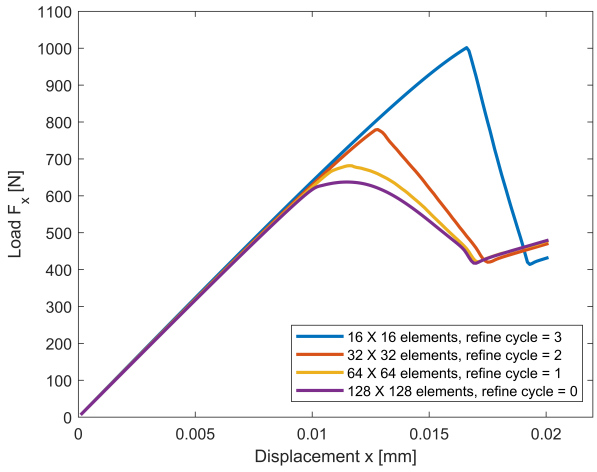

Figure 7.3: Comparison of force-displacement curves for four different mesh levels.

ison for the four cases under consideration are reported. The results clearly reflect that a smaller number of DOFs using multi-level mesh refinements need a much lower computational cost. Next, the influence of the locally refined mesh on the same mesh refinement depth is evaluated at the same level of mesh refinements for a fixed diffuse

Mesh [elements]	Refine cycle	Initial DOFs	Final DOFs	Run time [s]
16 × 16	3	891	3702	65.456
32 × 32	2	3315	5472	209.350
64 × 64	1	12771	14136	858.223
128 × 128	0	50115	50115	3959.346

Table 7.1: Parametric comparison for uniformly and iteratively refined meshes.

scale $\kappa = 0.011\,\text{mm}$ and a fixed initial mesh size $h = 0.022\,\text{mm}$, respectively. Case A: 64×64 elements with one cycle mesh refinement and the threshold for the mesh refinement process is $C = 0.65$, Case B: 64×64 elements with one cycle mesh refinement and the threshold for the mesh refinement process $C = 0.965$, and Case C: 128×128 elements globally pre-refined mesh with an initial mesh size $h = 0.011\,\text{mm}$ are investigated. The crack phase-field evolution at different displacements is illustrated in Fig. 7.4. The locally and globally pre-refined meshes are compared which yields the findings that the crack paths for all cases are almost the same. It means that for the same mesh refinement depth, the local mesh from different predictor refinements can obtain the similar crack phase-field evolution results. Again, in comparison with Case B (Threshold $C = 0.965$), larger regions around the crack are locally refined as in Case A (Threshold $C = 0.65$), where much more areas have met the criterion for the predictor refinement. It can be understood that in the predictor refinement concept, the elements are refined when the value of the crack phase-field concentrated around the crack regions is lower than the value of the pre-defined threshold C. In addition, the displacement-force curves for different refinement levels and global refinement are compared in Fig. 7.6. According to this finding, an excellent convergence can be clearly observed.

To investigate the minimum required refinement depth, a uniformed initial mesh with 64×64 elements and five different refinement depths 1, 2, 3, 4 and 5 are considered. The crack width $\kappa = 0.011\,\text{mm}$ and threshold $C = 0.10$ are fixed. The resulting

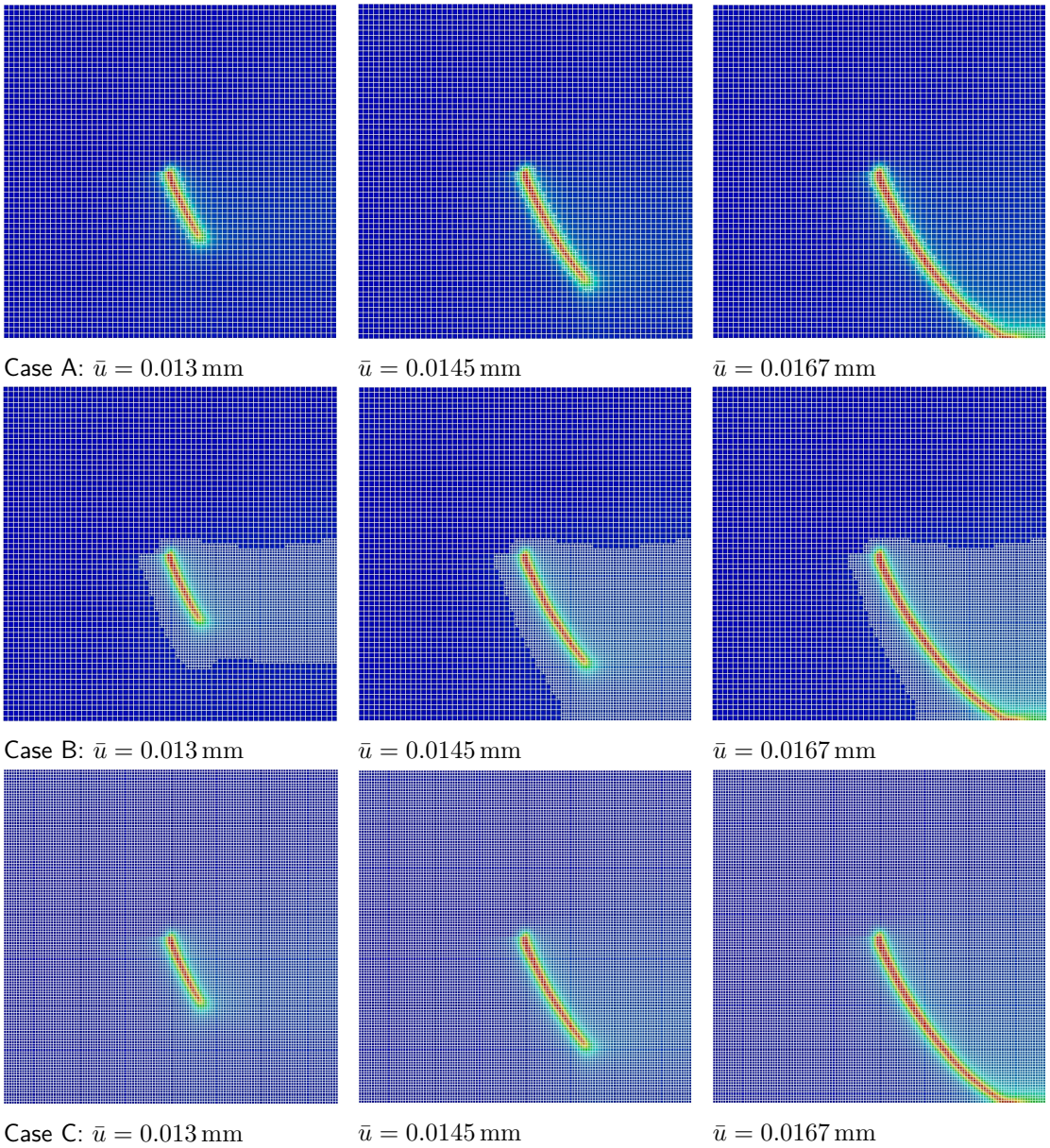

Figure 7.4: Comparison of the crack phase-field evolution for uniformly and iteratively refined meshes.

crack patterns at the final failure stage are illustrated in Fig. 7.5. As expected, the same crack pattern is obtained for the fine mesh (refinement depths 1, 2 and 3) and very fine mesh (refinement depths 4 and 5). For a mesh refinement depth 4 the smallest element size $h = 0.001\,375\,\text{mm}$ is obtained. The shear test is repeated by a refinement depth 5, leading to the smallest element size $h = 0.000\,687\,5\,\text{mm}$ in the critical zone. The subsequent study on the global responses in Fig. 7.7 leads to the conclusion that the results are mesh-independent when the effective mesh size is smaller than $h = 0.001\,375\,\text{mm}$ (refinement depth 4).

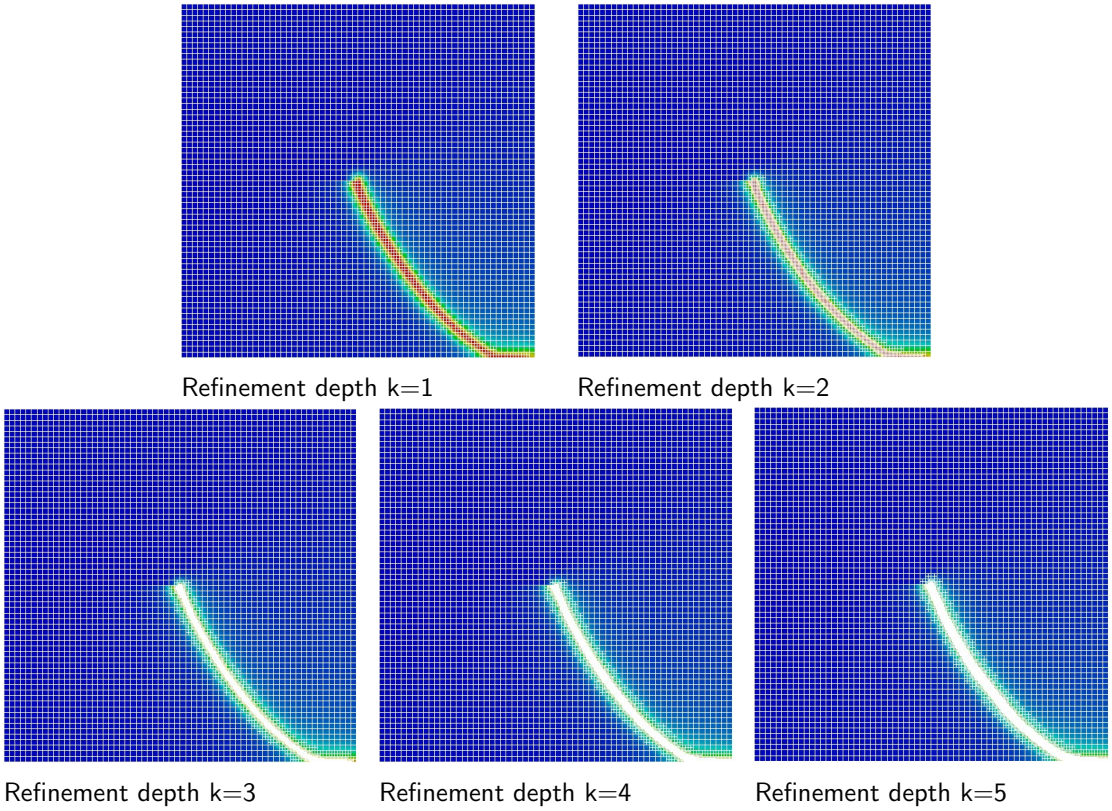

Figure 7.5: Final crack patterns for iteratively refined meshes.

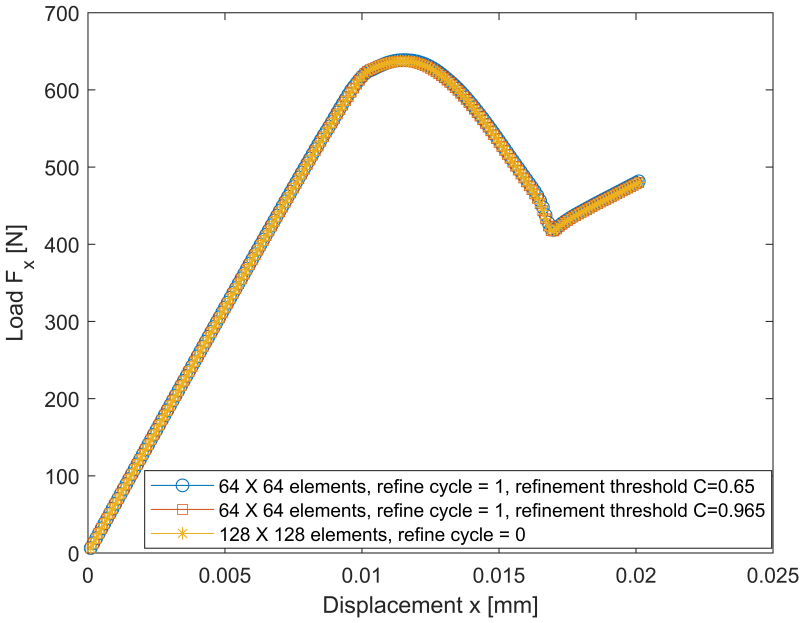

Figure 7.6: Comparison of force-displacement curves for uniformly and iteratively refined meshes.

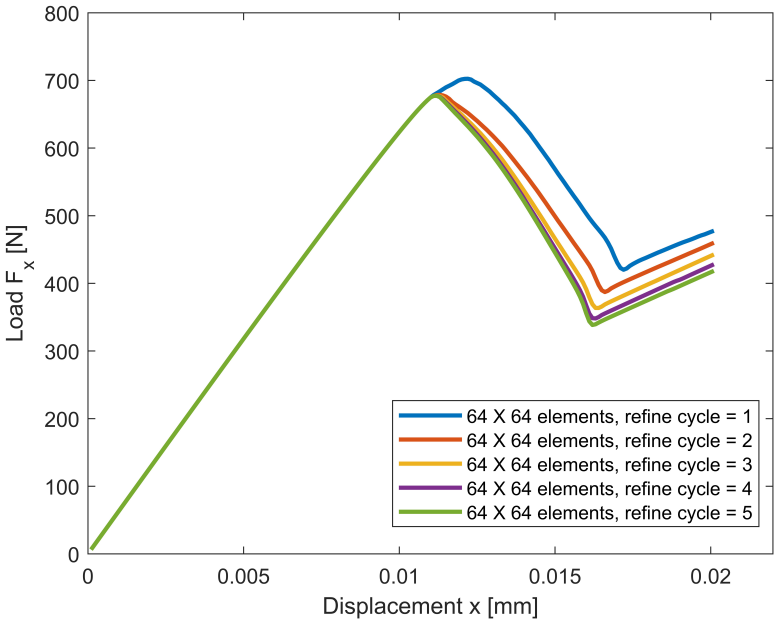

Figure 7.7: Comparison of force-displacement curves for five different mesh refinement depths.

7.2 Experimental validation: Crack initiation and propagation in the PBX 9502 plate specimen with cavity subjected to overall compression

In this example, simulations of crack propagation in a crack-free PBX 9502 specimen [149] with thickness of 12.7 mm are performed as shown in Fig. 7.8. The material of the specimen has $\lambda = 3285\,\text{MPa}$, $\mu = 821\,\text{MPa}$, and $\mathscr{G}_c = 0.1\,\text{N/mm}$. The displacement increment $\Delta\text{u} = 0.001\,\text{mm}$ at each time step is considered. The diffuse scale κ is chosen as 0.297 mm. An unstructured discretization with 12648 DOFs, linear shape functions, plane stress and refinement depth $k = 3$ are used. The value of the refinement threshold C is chosen as 0.15 in the simulation. Fig. 7.9 shows the crack phase-field

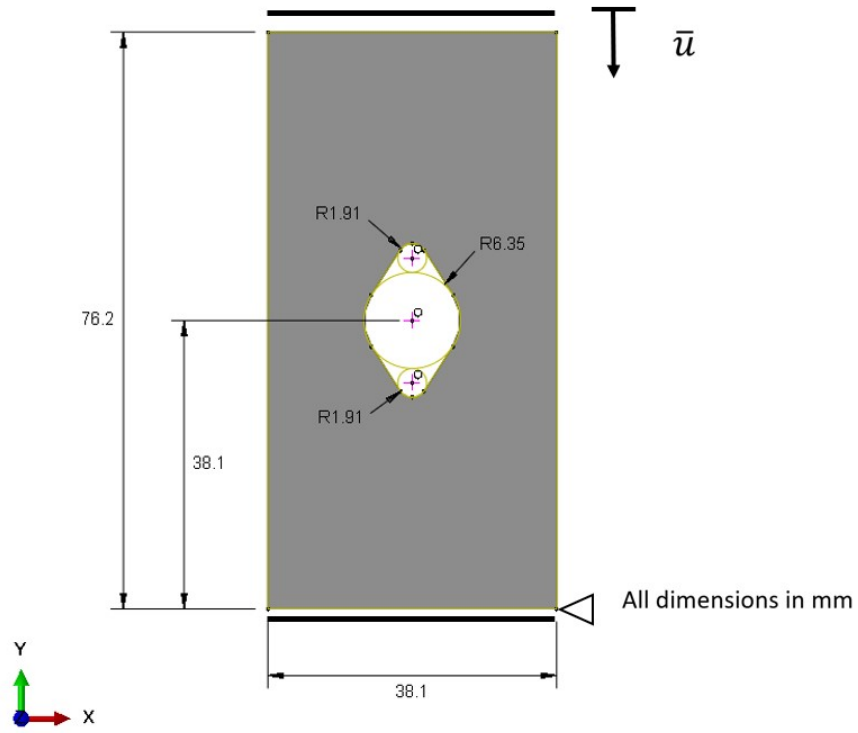

Figure 7.8: Geometry and boundary conditions of the plate specimen of plastic bonded explosive (PBX 9502) with a cavity sujected to compression.

evolution over time. In Fig. 7.9a and Fig. 7.9b, two cracks develop from the top and bottom of the cavity to the top and bottom edges. After that, the secondary damage zones appear at the left and right regions of the cavity. In order to objectively check whether the crack initiates in the secondary damage zones, the value of phase-field along the radius of the cavity is measured as shown in Fig. 7.10. It can be observed from the measured results is that no crack initiates in the secondary damage zones. Fig. 7.11 shows the experimental and simulated results, respectively. As evident from

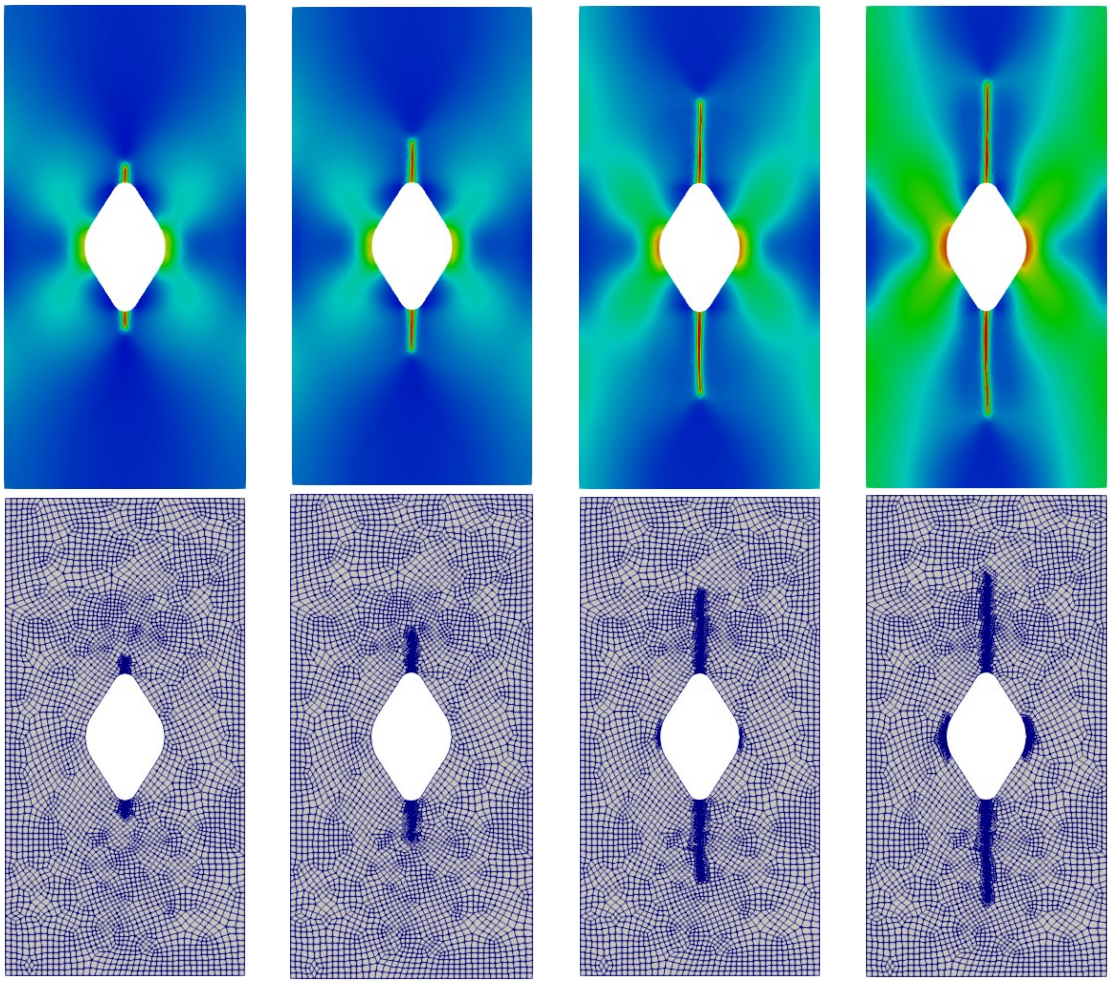

(a) $\bar{u} = 0.60\,\mathrm{mm}$ **(b)** $\bar{u} = 0.62\,\mathrm{mm}$ **(c)** $\bar{u} = 0.72\,\mathrm{mm}$ **(d)** $\bar{u} = 0.95\,\mathrm{mm}$

Figure 7.9: Crack phase-field evolution process and the corresponding refined meshes.

these data, the experimental results are similar to the ones obtained from the phase-field simulation.

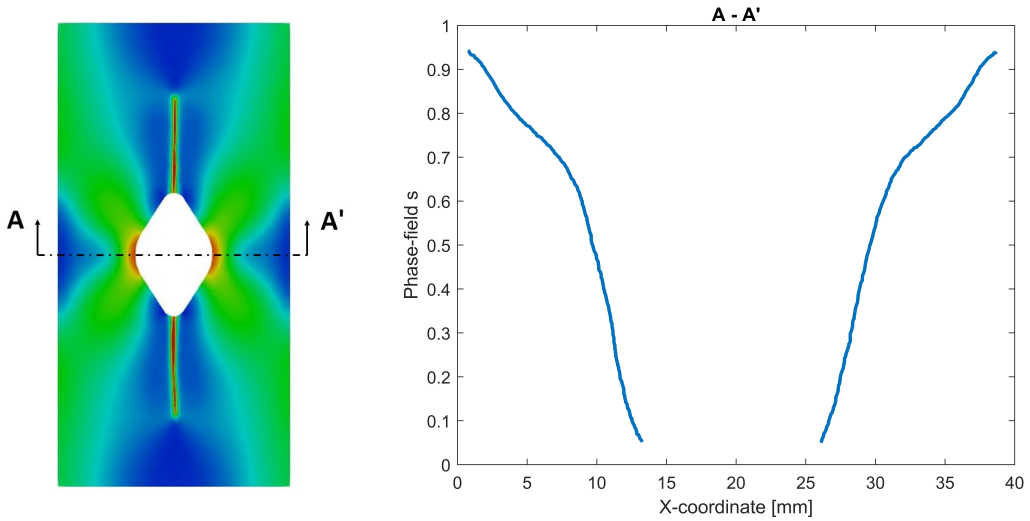

Figure 7.10: The measured position for the cross-section (left), and crack phase field in the cross-section (right).

The initial coarse mesh and final mesh obtained by applying the refinement technique are depicted in Fig. 7.12. 12648 DOFs are initially generated with the smallest mesh size $h = 2.376\,\text{mm}$ in the entire domain. After the adaptive refinement process, 28563 DOFs are achieved with the smallest mesh size $h = 0.297\,\text{mm}$.

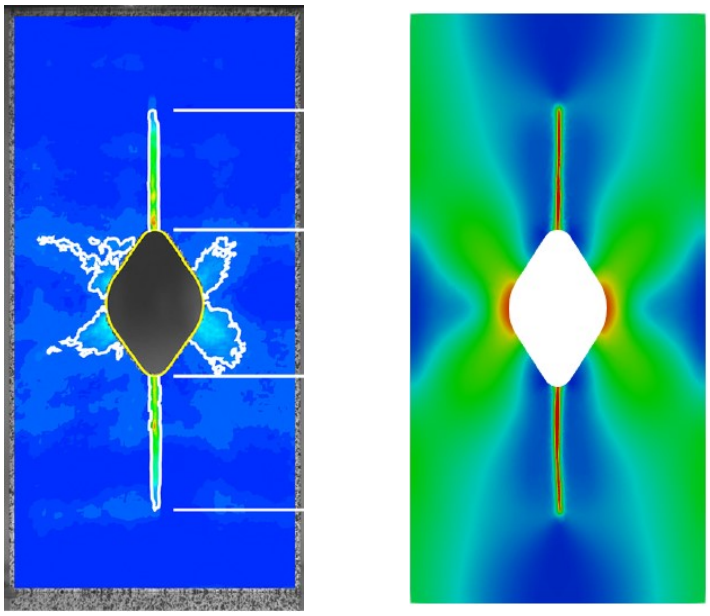

Figure 7.11: Measured cracks [149] (left); Crack phase-field (right).

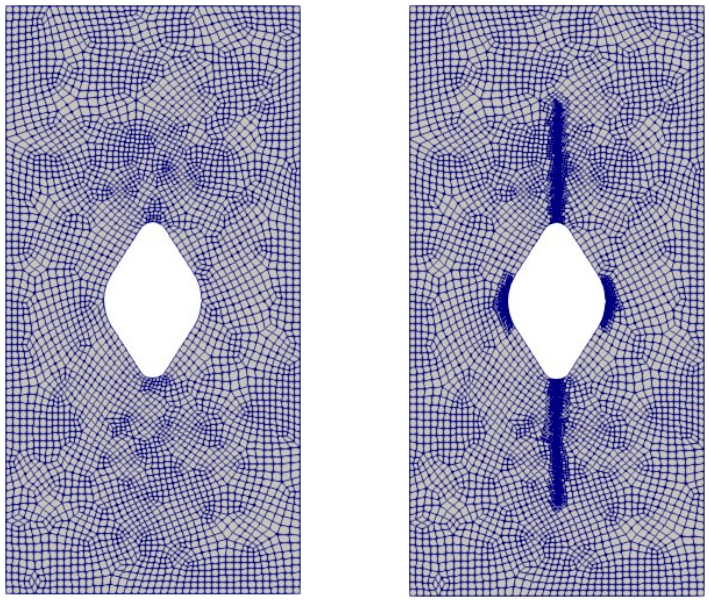

Figure 7.12: Initial mesh (left); Final mesh (right).

8

Conclusions and future research

8.1 Summary of achievements

In this PhD thesis, a phase-field model was proposed to predict crack evolution under thermomechanical loadings, with special attention paid to thermoelastic fracturing processes in polycrystalline materials. This thesis started with an overview of phase-field modelling of brittle fracture in Chapter 1. The basic concepts of continuum mechanics and thermodynamics were reviewed in Chapter 2. Moreover, computational implementation aspects of phase-field models were presented in Chapter 3. Four com-

monly used phase-field models were applied to simulate crack initiation and propagation under compressive loadings in Chapter 4. Chapter 5 and Chapter 6 deal with application of the phase-field method to predict fracturing processes in anisotropic materials under isothermal and non-isothermal conditions. Finally, an adaptive phase-field model was used to model the compressive crack evolution in Chapter 7.

One of the most crucial and challenging tasks in the phase-field modelling of fracture is the prediction of compressive and tensile failure in an integrated manner. An improper split of the elastic strain energy density may lead to an incorrect description of the fracture behavior. In Chapter 4, four commonly used phase-field models, the isotropic model [41], the volumetric/deviatoric split [223] and the spectral split [169], as well as the hybrid formulation [69], were investigated using three numerical examples. For the first example, it was concerned with the simulations of crack evolution in a V-notched specimen subjected to cyclic loads. We found that the spectral and volumetric/deviatoric splits can describe the stiffness recovery in compression. On the contrary, the hybrid and isotropic models cannot avoid the issues of material interpenetration when the sample undergoes compressive loadings [246]. An explanation for this is that the stiffness tensor is degraded and remains degraded afterwards in the compressed state. Thus, the modification in the hybrid and isotropic models is at least for this type of load history not applicable.

The second example was designed to demonstrate the capabilities of different models to handle compressive fracture problems. From the results it can quite clearly be seen that the volumetric/deviatoric split still leads to unphysical fracture propagation in compression, e.g. see Fig. 4.9 and particularly Fig. 4.12. One possible explanation is the fact that the compressive energy from the volumetric/deviatoric split evolves into the driving energy for crack growth in compression. It can also be seen that all these models cannot prevent crack face overlapping during the compression phase.

In the third example, these models were applied for predicting intricate compressive fracturing processes. To this end, simulations of mixed mode crack initiation and propagation in a pre-notched specimen containing three different bridge angles γ of 23°, 68° and 90°, were carried out. We found that the isotropic model cannot prevent material interpenetration during the compression phase. An important reason for this phenomenon is that there is no distinction between the fracture behavior in tension and compression in the isotropic model.

Furthermore, an agreement between experimental and numerical results was not found in the volumetric/deviatoric split. In order to avoid unrealistic crack evolution in compression, the spectral split was used, which degraded only the tensile part of the elastic strain energy density in the damage zones. Compared with other models, the spectral split shows a good performance in case of $\gamma = 23^\circ$, $\gamma = 68^\circ$, and $\gamma = 90^\circ$. It is noticeable that the spectral split leads to a large thickness of the diffuse approximation of the crack in case of $\gamma = 68^\circ$, e.g. see Fig. 4.22d. A very small diffuse parameter κ seems to remove some spurious effects in compression, however, extreme fine meshes are required in the simulation. Moreover, the hybrid model cannot correctly simulate the mixed mode fracturing process under compressive loadings. It should be emphasized that the hybrid model is able to remove the spurious effects such as in case of $\gamma = 68^\circ$, whereas the simulated wing crack initiation angle cannot be comparable with experimental data as plotted in Fig. 4.24.

Nevertheless, there are still some discrepancies observed in the spectral split, which can be caused by: (i) frictional movements along the crack surface have not been considered; (ii) specific properties of the rock-like materials, such as geometric and physical nonlinearities, have not been taken into account; (iii) self-contacts algorithms have not yet been implemented. Thus, the proper choice of tension-compression splits (indicated as numerically anisotropic models) must be taken into consideration in case of

compression.

Chapter 5 deals with application of phase-field model to simulate anisotropic crack evolution under tensile loadings. Comprehensive parameter studies were performed, and the results were analyzed. Simulations of the anisotropic fracture within the higher value of material orientation were also considered, though the resulting crack path was no longer in alignment with the predefined crack orientation, and the opposite direction with fluctuating crack paths was observed. Furthermore, it is necessary to account for such phenomena that the widely used anisotropic materials (e.g. woods) consist of the higher value of material orientation in the structure, which can play an important role in material design processes. This topic will be addressed elsewhere. Representative numerical examples of crack evolution in polycrystalline materials were carried out which can validate its capability of modelling of inter- and transgranular fracturing processes.

Having the evolution of the temperature field on the results in mind, the proposed phase-field model for thermoelastic crack nucleation and propagation in polycrystalline materials was investigated by means of representative numerical examples in Chapter 6. The coupled multiphysics problems were robustly solved using a staggered scheme. From the results it can be seen that the material orientation can strongly influence the thermoelastic fracturing processes in polycrystalline solids. Further on, the effects of grain size on the fracture behavior in polycrystalline structures were investigated in detail.

Finally, an adaptive phase-field model was employed to simulate fracturing processes under compressive loadings in Chapter 7. We found that the utilized adaptive mesh refinement strategy can significantly reduce the computational costs.

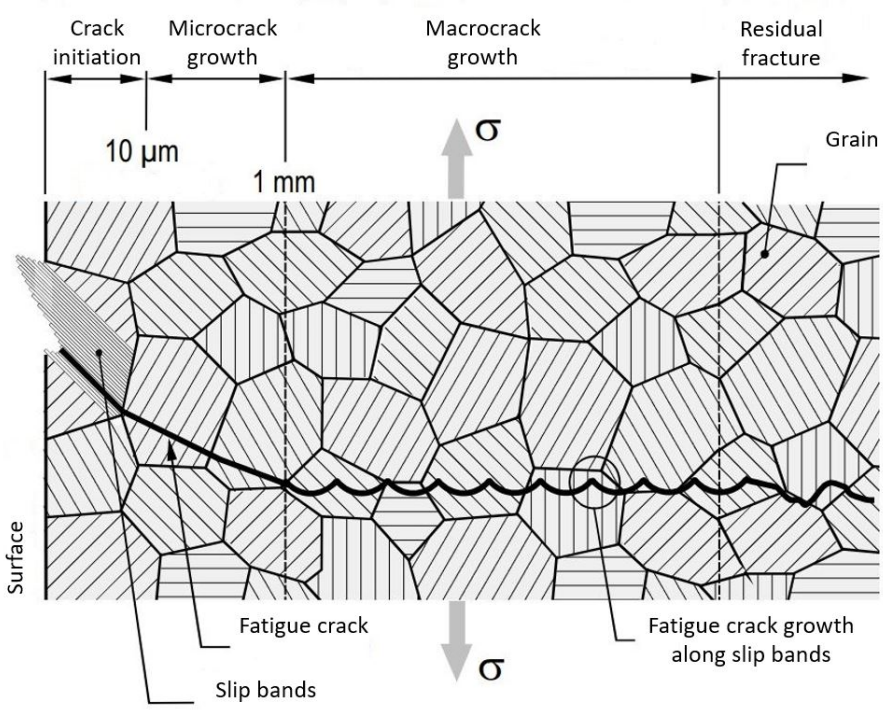

Figure 8.1: Fatigue fracture in polycrystalline materials [138].

8.2 Scope for future work

Undoubtedly, the research work presented in this PhD thesis will be continued, and there are a few research directions that can be taken into account in future studies. In this regard, the following tasks are proposed:

- Implementation of self-contacts algorithms for simulations of crack evolution in compression. Fei & Choo [83] proposed a phase-field method for modelling brittle fracture with frictional contact.
- Modelling of anisotropic ductile fracture under thermomechanical loadings. Dean et al. [65] developed a phase-field model for ductile fracture of anisotropic materials. In their model, the direction of anisotropic ductile crack growth is dependent on the material orientation.

- Development of a phase-field model for fatigue fracture in polycrystalline materials (see Fig. 8.1). Seiler et al. [228] proposed a numerically efficient phase-field model for fatigue crack nucleation and propagation in ductile materials.

A

Implementation Details

A.1 Discretization in space and time

Two-dimensional finite element implementation of phase-field model for crack evolution in anisotropic materials under thermomechanical loadings is explained in this chapter. The nodal degrees of freedom are the displacements $\boldsymbol{u}$, the phase-field s and the temperature field θ. The weak forms of the governing equations are given by

$$\int_{\Omega} [\nabla \delta \boldsymbol{u}]^T : \boldsymbol{\sigma} \mathrm{d}v - \int_{\partial \Omega_{\boldsymbol{t}}} \delta \boldsymbol{u} \cdot \boldsymbol{t} \, \mathrm{d}a = \mathbf{0}, \tag{A.1}$$

$$\int_{\Omega} \left[2\mathscr{G}_c \kappa \nabla \delta s \cdot \boldsymbol{\omega} \cdot \nabla s + \delta s \left[2s\psi_e^+ + \frac{\mathscr{G}_c}{2\kappa}(s-1) \right] \right] \mathrm{d}v = 0, \tag{A.2}$$

and

$$-\int_{\Omega} \left[\rho c_p \dot{\theta} \delta\theta - \boldsymbol{q} \cdot \nabla \delta\theta \right] \mathrm{d}v - \int_{\partial\Omega_{\boldsymbol{q}}} \boldsymbol{q}_s \cdot \boldsymbol{n} \delta\theta \, \mathrm{d}a = 0, \tag{A.3}$$

with $\delta\boldsymbol{u}$, δs and $\delta\theta$ denoting the variational test functions.

Next, the weak forms (Eq. (A.1) - (A.3)) are implicitly solved using finite element method (FEM). The computational domain Ω is discretized with four-node quadrilateral isoparametric elements. Therefore, the nodal values for the continuous variables $\{\boldsymbol{u}, s, \theta\}$ are given by

$$\boldsymbol{u} = \sum_{I=1}^{n} N_I \boldsymbol{u}_I, \quad s = \sum_{I=1}^{n} N_I s_I, \quad \theta = \sum_{I=1}^{n} N_I \theta_I, \tag{A.4}$$

in which n is denoted as the total number of nodes in each element, and the shape functions N_I are associated with node I. The corresponding gradients are written as

$$\boldsymbol{\varepsilon} = \sum_{I=1}^{n} \boldsymbol{B}_I^{\boldsymbol{u}} \boldsymbol{u}_I, \quad \nabla s = \sum_{I=1}^{n} \boldsymbol{B}_I^{s} s_I, \quad \nabla\theta = \sum_{I=1}^{n} \boldsymbol{B}_I^{\theta} \theta_I, \tag{A.5}$$

with

$$\boldsymbol{B}_I^{\boldsymbol{u}} = \begin{bmatrix} N_{I,x} & 0 \\ 0 & N_{I,y} \\ N_{I,y} & N_{I,x} \end{bmatrix} \quad \text{and} \quad \boldsymbol{B}_I^{s} = \boldsymbol{B}_I^{\theta} = \begin{bmatrix} N_{I,x} \\ N_{I,y} \end{bmatrix}, \tag{A.6}$$

where $N_{I,x}$ and $N_{I,y}$ are defined as the differentiation of the bilinear shape functions with respect to the coordinates x and y, respectively.

The internal force $\boldsymbol{F}_I^{\boldsymbol{u},\mathrm{int}}$ and external force $\boldsymbol{F}_I^{\boldsymbol{u},\mathrm{ext}}$ of the displacement field are given by

$$\boldsymbol{F}_I^{\boldsymbol{u},\mathrm{int}} = \int_{\Omega} [\boldsymbol{B}_I^{\boldsymbol{u}}]^T \boldsymbol{\sigma} \, \mathrm{d}v, \tag{A.7}$$

and

$$\boldsymbol{F}_I^{\boldsymbol{u},\text{ext}} = \int_{\partial\Omega^t} N_I \boldsymbol{t}\, \mathrm{d}a, \tag{A.8}$$

respectively.

The internal forces of the phase-field are defined as

$$F_I^{s,\text{int}} = \int_\Omega \left[2\kappa \mathscr{G}_c \left[\boldsymbol{B}_I^s\right]^T \boldsymbol{\omega} \nabla s + N_I \left[2s\psi_e^+ + \frac{\mathscr{G}_c}{2\kappa}(s-1) \right] \right] \mathrm{d}v. \tag{A.9}$$

Finally, the inner force $F_I^{\theta,\text{int}}$ and external force $F_I^{\theta,\text{ext}}$ of the thermal field are written as

$$F_I^{\theta,\text{int}} = \int_\Omega \left[N_I c_\theta \rho \dot{\theta} - \left[\boldsymbol{B}_I^\theta\right]^T \boldsymbol{q} \right] \mathrm{d}v, \tag{A.10}$$

and

$$F_I^{\theta,\text{ext}} = -\int_{\partial\Omega_{\boldsymbol{q}}} \boldsymbol{q}_s^T \boldsymbol{n} N_I \, \mathrm{d}a, \tag{A.11}$$

respectively.

By means of Eqs. (A.7) - (A.11), the residual of the weak forms at node I can be expressed as

$$\begin{cases} \boldsymbol{R}_I^{\boldsymbol{u}} & = \boldsymbol{F}_I^{\boldsymbol{u},\text{ext}} - \boldsymbol{F}_I^{\boldsymbol{u},\text{int}}, \\ R_I^s & = -F_I^{s,\text{int}}, \\ R_I^\theta & = F_I^{\theta,\text{ext}} - F_i^{\theta,\text{int}}. \end{cases} \tag{A.12}$$

The stiffness matrix $\boldsymbol{K}_{IJ}$ on the element level is calculated by

$$\boldsymbol{K}_{IJ} = \begin{bmatrix} \boldsymbol{K}_{IJ}^{\boldsymbol{uu}} & \boldsymbol{K}_{IJ}^{\boldsymbol{us}} & \boldsymbol{K}_{IJ}^{\boldsymbol{u}\theta} \\ \boldsymbol{K}_{IJ}^{\boldsymbol{su}} & K_{IJ}^{ss} & K_{IJ}^{s\theta} \\ \boldsymbol{K}_{IJ}^{\theta\boldsymbol{u}} & K_{IJ}^{\theta s} & K_{IJ}^{\theta\theta} \end{bmatrix}, \quad \text{with} \quad I, J = 1, 2, \ldots, n, \tag{A.13}$$

where the corresponding stiffness submatrices are given by

$$\boldsymbol{K}_{IJ}^{\boldsymbol{uu}} = \int_{\Omega} [\boldsymbol{B}_I^{\boldsymbol{u}}]^T \frac{\partial \boldsymbol{\sigma}}{\partial \boldsymbol{\varepsilon}_e} \boldsymbol{B}_J^{\boldsymbol{u}} \, \mathrm{d}v, \tag{A.14}$$

$$\boldsymbol{K}_{IJ}^{\boldsymbol{us}} = \int_{\Omega} [\boldsymbol{B}_I^{\boldsymbol{u}}]^T \frac{\partial \boldsymbol{\sigma}}{\partial s} N_J^s \, \mathrm{d}v, \tag{A.15}$$

$$\boldsymbol{K}_{IJ}^{\boldsymbol{u}\theta} = \int_{\Omega} [\boldsymbol{B}_I^{\boldsymbol{u}}]^T \frac{\partial \boldsymbol{\sigma}}{\partial \theta} N_J^{\theta} \, \mathrm{d}v, \tag{A.16}$$

$$\boldsymbol{K}_{IJ}^{\boldsymbol{su}} = \int_{\Omega} 2sN_I^s \left[\frac{\partial \psi_e^+}{\partial \boldsymbol{\varepsilon}_e} \right]^T \boldsymbol{B}_J^{\boldsymbol{u}} \, \mathrm{d}v, \tag{A.17}$$

$$K_{IJ}^{ss} = \int_{\Omega} \left[2\kappa \mathscr{G}_c \, [\boldsymbol{B}_I^s]^T \, \boldsymbol{\omega} \boldsymbol{B}_J^s + \left(\frac{\mathscr{G}_c}{2\kappa} + 2\psi_e^+ \right) N_I^s N_J^s \right] \mathrm{d}v, \tag{A.18}$$

$$K_{IJ}^{s\theta} = \int_{\Omega} 2sN_I^s \frac{\partial \psi_e^+}{\partial \boldsymbol{\varepsilon}_e} \frac{\partial \boldsymbol{\varepsilon}_e}{\partial \theta_J} \, \mathrm{d}v, \tag{A.19}$$

$$\boldsymbol{K}_{IJ}^{\theta \boldsymbol{u}} = \boldsymbol{0}, \tag{A.20}$$

$$K_{IJ}^{\theta s} = -\int_{\Omega} \left[\boldsymbol{B}_I^{\theta}\right]^T \frac{\partial \boldsymbol{q}}{\partial s_J}\,\mathrm{d}v, \tag{A.21}$$

and

$$K_{IJ}^{\theta\theta} = \int_{\Omega} \left(\zeta\left(s^2-1\right)+1\right)\left[\boldsymbol{B}_I^{\theta}\right]^T \boldsymbol{K}\boldsymbol{B}_J^{\theta}\,\mathrm{d}v. \tag{A.22}$$

Similar to the element stiffness matrix, the damping matrix $\boldsymbol{D}_{IJ}$ is expressed as

$$\boldsymbol{D}_{IJ} = \begin{bmatrix} \mathbf{0} & \mathbf{0} & \mathbf{0} \\ \mathbf{0} & 0 & 0 \\ \mathbf{0} & 0 & \int_{\Omega} \rho c_p N_I^{\theta} N_J^{\theta}\mathrm{d}v. \end{bmatrix}. \tag{A.23}$$

Now, the system (tangent) matrix on the element level reads

$$\boldsymbol{S}_{IJ} = \boldsymbol{K}_{IJ} + \frac{1}{\Delta t}\boldsymbol{D}_{IJ}. \tag{A.24}$$

Remark 4 *Due to the staggered solution scheme, the coupling terms* $\boldsymbol{K}_{IJ}^{\boldsymbol{us}}$, $\boldsymbol{K}_{IJ}^{\boldsymbol{u}\theta}$, $\boldsymbol{K}_{IJ}^{\boldsymbol{su}}$, $K_{IJ}^{s\theta}$, $\boldsymbol{K}_{IJ}^{\boldsymbol{\theta u}}$, *and* $K_{IJ}^{\theta s}$ *are neglected whereby the resulting error is assumed to be small.*

A.2 Implementation of the irreversibility constraint

To prevent the crack from healings, a history variable $\mathcal{H}(\boldsymbol{x},\tau)$ can be applied

$$\mathcal{H}(\boldsymbol{x},\tau) = \max_{\tau\in[0,t]} \psi_e^{+}(\boldsymbol{\varepsilon}_e(\boldsymbol{x})), \tag{A.25}$$

which is updated during the simulation time t.

Therefore, the residual and tangent can be recovered by

$$R_I^s = -\int_\Omega \left[2\kappa \mathscr{G}_c \left[\boldsymbol{B}_I^s\right]^T \boldsymbol{\omega} \nabla s + N_I \left[2s\mathcal{H} + \frac{\mathscr{G}_c}{2\kappa}\left(s-1\right) \right] \right] \mathrm{d}v, \tag{A.26}$$

and

$$K_{IJ}^{ss} = \int_\Omega \left[2\kappa \mathscr{G}_c \left[\boldsymbol{B}_I^s\right]^T \boldsymbol{\omega} \boldsymbol{B}_J^s + \left(\frac{\mathscr{G}_c}{2\kappa} + 2\mathcal{H} \right) N_I^s N_J^s \right] \mathrm{d}v, \tag{A.27}$$

respectively.

References

[1] Akarapu, S. & Zbib, H. M. (2006). Numerical analysis of plane cracks in strain-gradient elastic materials. *International Journal of Fracture*, 141(3), 403–430.

[2] Akatsu, T., Takashima, H., Shinoda, Y., Wakai, F., & Wakayama, S. (2016). Thermal-shock fracture and damage resistance improved by whisker reinforcement in alumina matrix composite. *International Journal of Applied Ceramic Technology*, 13(4), 653–661.

[3] Alessi, R., Ambati, M., Gerasimov, T., Vidoli, S., & De Lorenzis, L. (2018). *Comparison of Phase-Field Models of Fracture Coupled with Plasticity*, book section Chapter 1, (pp. 1–21). Computational Methods in Applied Sciences. Springer-Verlag.

[4] Aliabadi, M. H. (1997). Boundary element formulations in fracture mechanics. *Applied Mechanics Reviews*, 50(2), 83–96.

[5] Aliabadi, M. H. & Sollero, P. (1998). Crack growth analysis in homogeneous orthotropic laminates. *Composites Science and Technology*, 58(10), 1697–1703.

[6] Alipour, A., Reese, S., & Wulfinghoff, S. (2019). A grain boundary model for gradient-extended geometrically nonlinear crystal plasticity: theory and numerics. *International Journal of Plasticity*, 118, 17–35.

[7] Alipour, A., Wulfinghoff, S., Bayat, H. R., Reese, S., & Svendsen, B. (2018). The concept of control points in hybrid discontinuous galerkin methods—application to geometrically nonlinear crystal plasticity. *International Journal for Numerical Methods in Engineering*, 114(5), 557–579.

[8] Amani, J., Oterkus, E., Areias, P., Zi, G., Nguyen-Thoi, T., & Rabczuk, T. (2016). A non-ordinary state-based peridynamics formulation for thermoplastic fracture. *International Journal of Impact Engineering*, 87, 83–94.

[9] Ambati, M. (2017). *Phase-field modeling and computations of brittle and ductile fracture for solids and shells*. Technische Universität Braunschweig.

[10] Ambati, M. & De Lorenzis, L. (2016). Phase-field modeling of brittle and ductile fracture in shells with isogeometric nurbs-based solid-shell elements. *Computer Methods in Applied Mechanics and Engineering*, 312, 351–373.

[11] Ambati, M., Gerasimov, T., & De Lorenzis, L. (2014). A review on phase-field models of brittle fracture and a new fast hybrid formulation. *Computational Mechanics*, 55(2), 383–405.

[12] Ambati, M., Gerasimov, T., & De Lorenzis, L. (2015). Phase-field modeling of ductile fracture. *Computational Mechanics*, 55(5), 1017–1040.

[13] Amor, H., Marigo, J.-J., & Maurini, C. (2009). Regularized formulation of the variational brittle fracture with unilateral contact: Numerical experiments. *Journal of the Mechanics and Physics of Solids*, 57(8), 1209–1229.

[14] Anderson, T. L. (2017). *Fracture Mechanics: Fundamentals and Applications*. Taylor & Francis.

[15] Anitescu, C., Hossain, M. N., & Rabczuk, T. (2018). Recovery-based error estimation and adaptivity using high-order splines over hierarchical t-meshes. *Computer Methods in Applied Mechanics and Engineering*, 328, 638–662.

[16] Areias, P., Msekh, M. A., & Rabczuk, T. (2016). Damage and fracture algorithm using the screened poisson equation and local remeshing. *Engineering Fracture Mechanics*, 158, 116–143.

[17] Arndt, D., Bangerth, W., Blais, B., Clevenger, T. C., Fehling, M., Grayver, A. V., Heister, T., Heltai, L., Kronbichler, M., Maier, M., Munch, P., Pelteret, J.-P., Rastak, R., Thomas, I., Turcksin, B., Wang, Z., & Wells, D. (2020). The `deal.II` library, version 9.2. *Journal of Numerical Mathematics*, 28(3), 131–146.

[18] Arndt, D., Bangerth, W., Davydov, D., Heister, T., Heltai, L., Kronbichler, M., Maier, M., Pelteret, J.-P., Turcksin, B., & Wells, D. (2021). The deal.II finite element library: Design, features, and insights. *Computers & Mathematics with Applications*, 81, 407–422.

[19] Artina, M., Fornasier, M., Micheletti, S., & Perotto, S. (2015). Anisotropic mesh adaptation for crack detection in brittle materials. *SIAM Journal on Scientific Computing*, 37(4), B633–B659.

[20] Aßmus, M., Naumenko, K., & Altenbach, H. (2016). A multiscale projection approach for the coupled global–local structural analysis of photovoltaic modules. *Composite Structures*, 158, 340 – 358.

[21] Ayachit, U. (2015). The paraview guide: A parallel visualization application. *Kitware, Inc.*

[22] Azinpour, E., Ferreira, J. P. S., Parente, M. P. L., & de Sa, J. C. (2018). A simple and unified implementation of phase field and gradient damage models. *Advanced Modeling and Simulation in Engineering Sciences*, 5(1).

[23] Badnava, H., Msekh, M. A., Etemadi, E., & Rabczuk, T. (2018). An h-adaptive thermo-mechanical phase field model for fracture. *Finite Elements in Analysis and Design*, 138, 31–47.

[24] Bahr, H. A., Weiss, H. J., Maschke, H. G., & Meissner, F. (1988). Multiple crack propagation in a strip caused by thermal shock. *Theoretical and Applied Fracture Mechanics*, 10(3), 219–226.

[25] Bathe, K.-J. (1982). Finite element procedures for solids and structures linear analysis. *Finite Element Procedures*, (pp. 148–214).

[26] Bedford, A. & Passman, L. (1985). *Hamilton's principle in continuum mechanics*. University of Texas at Austin.

[27] Belnoue, J. P., Nguyen, G. D., & Korsunsky, A. M. (2007). A one-dimensional nonlocal damage-plasticity model for ductile materials. *International Journal of Fracture*, 144(1), 53–60.

[28] Benedetti, I. & Aliabadi, M. H. (2013). A three-dimensional cohesive-frictional grain-boundary micromechanical model for intergranular degradation and failure in polycrystalline materials. *Computer Methods in Applied Mechanics and Engineering*, 265, 36–62.

[29] Benedetti, I. & Barbe, F. (2013). Modelling polycrystalline materials: an overview of three-dimensional grain-scale mechanical models. *Journal of Multiscale Modelling*, 5(01), 1350002.

[30] Benedetti, I., Gulizzi, V., & Milazzo, A. (2018). Grain-boundary modelling of hydrogen assisted intergranular stress corrosion cracking. *Mechanics of Materials*, 117, 137–151.

[31] Benvenuti, E. & Simone, A. (2013). One-dimensional nonlocal and gradient elasticity: Closed-form solution and size effect. *Mechanics Research Communications*, 48, 46–51.

[32] Bertram, A. & Glüge, R. (2015). *Solid Mechanics*. Springer-Verlag.

[33] Betten, J. (2001). *Kontinuumsmechanik*. Springer-Verlag.

[34] Bilgen, C., Kopanicakova, A., Krause, R., & Weinberg, K. (2017). A phase-field approach to conchoidal fracture. *Meccanica*, 53(6), 1203–1219.

[35] Biner, S. B. (2017). *Programming Phase-Field Modeling*. Springer-Verlag.

[36] Blendell, J. E. & Coble, R. L. (1982). Measurement of stress due to thermal expansion anisotropy in al2o3. *Journal of the American Ceramic Society*, 65(3), 174–178.

[37] Bleyer, J. & Alessi, R. (2018). Phase-field modeling of anisotropic brittle fracture including several damage mechanisms. *Computer Methods in Applied Mechanics and Engineering*, 336, 213–236.

[38] Borden, M. J., Hughes, T. J. R., Landis, C. M., Anvari, A., & Lee, I. J. (2016). A phase-field formulation for fracture in ductile materials: Finite deformation balance law derivation, plastic degradation, and stress triaxiality effects. *Computer Methods in Applied Mechanics and Engineering*, 312, 130–166.

[39] Borden, M. J., Hughes, T. J. R., Landis, C. M., & Verhoosel, C. V. (2014). A higher-order phase-field model for brittle fracture: Formulation and analysis within the isogeometric analysis framework. *Computer Methods in Applied Mechanics and Engineering*, 273, 100–118.

[40] Borden, M. J., Verhoosel, C. V., Scott, M. A., Hughes, T. J. R., & Landis, C. M. (2012). A phase-field description of dynamic brittle fracture. *Computer Methods in Applied Mechanics and Engineering*, 217-220, 77–95.

[41] Bourdin, B., Francfort, G. A., & Marigo, J.-J. (2008). The variational approach to fracture. *Journal of Elasticity*, 91(1-3), 5–148.

[42] Bourdin, B., Marigo, J.-J., Maurini, C., & Sicsic, P. (2014). Morphogenesis and propagation of complex cracks induced by thermal shocks. *Physical Review Letters*, 112(1), 014301.

[43] Bower, A. F. (2013). *Applied Mechanics of Solids*. CRC Press.

[44] Bryant, E. C. & Sun, W. (2018). A mixed-mode phase field fracture model in anisotropic rocks with consistent kinematics. *Computer Methods in Applied Mechanics and Engineering*, 342, 561 – 584.

[45] Burke, S., Ortner, C., & Süli, E. (2010). An adaptive finite element approximation of a variational model of brittle fracture. *SIAM Journal on Numerical Analysis*, 48(3), 980–1012.

[46] Cajuhi, T. (2019). *Fracture in porous media: phase-field modeling, simulation and experimental validation*. Technische Universität Braunschweig.

[47] Camacho, G. T. & Ortiz, M. (1996). Computational modelling of impact damage in brittle materials. *International Journal of Solids and Structures*, 33(20-22), 2899–2938.

[48] Carlsson, J. & Isaksson, P. (2019). Crack dynamics and crack tip shielding in a material containing pores analysed by a phase field method. *Engineering Fracture Mechanics*, 206, 526–540.

[49] Carollo, V., Guillén-Hernández, T., Reinoso, J., & Paggi, M. (2018a). Recent advancements on the phase field approach to brittle fracture for heterogeneous materials and structures. *Advanced modeling and simulation in engineering sciences*, 5(1), 1–29.

[50] Carollo, V., Reinoso, J., & Paggi, M. (2017). A 3d finite strain model for intralayer and interlayer crack simulation coupling the phase field approach and cohesive zone model. *Composite Structures*, 182, 636–651.

[51] Carollo, V., Reinoso, J., & Paggi, M. (2018b). Modeling complex crack paths in ceramic laminates: A novel variational framework combining the phase field method of fracture and the cohesive zone model. *Journal of the European Ceramic Society*, 38(8), 2994–3003.

[52] Carrara, P., Ambati, M., Alessi, R., & De Lorenzis, L. (2020). A framework to model the fatigue behavior of brittle materials based on a variational phase-field approach. *Computer Methods in Applied Mechanics and Engineering*, 361, 112731.

[53] Choo, J. & Sun, W. (2018). Cracking and damage from crystallization in pores: Coupled chemo-hydro-mechanics and phase-field modeling. *Computer Methods in Applied Mechanics and Engineering*, 335, 347–379.

[54] Chu, D., Li, X., & Liu, Z. (2017). Study the dynamic crack path in brittle material under thermal shock loading by phase field modeling. *International Journal of Fracture*, 208(1-2), 115–130.

[55] Clayton, J. D. & Knap, J. (2016). Phase field modeling and simulation of coupled fracture and twinning in single crystals and polycrystals. *Computer Methods in Applied Mechanics and Engineering*, 312, 447–467.

[56] Clayton, J. D., Leavy, R. B., & Knap, J. (2019). Phase field modeling of heterogeneous microcrystalline ceramics. *International Journal of Solids and Structures*, 166, 183–196.

[57] Conti, S., Focardi, M., & Iurlano, F. (2016). Phase field approximation of cohesive fracture models. *Annales de l'Institut Henri Poincaré C, Analyse non linéaire*, 33(4), 1033–1067.

[58] Corson, F., Adda-Bedia, M., Henry, H., & Katzav, E. (2009). Thermal fracture as a framework for quasi-static crack propagation. *International Journal of Fracture*, 158(1), 1–14.

[59] Cottrell, J. A., Hughes, T. J., & Bazilevs, Y. (2009). *Isogeometric analysis: toward integration of CAD and FEA*. John Wiley & Sons.

[60] Dal, H., Gültekin, O., Aksu Denli, F., & Holzapfel, G. A. (2017). Phase-field models for the failure of anisotropic continua. *Pamm*, 17(1), 91–94.

[61] Davidge, R. W. & Green, T. J. (1968). The strength of two-phase ceramic/glass materials. *Journal of Materials Science*, 3(6), 629–634.

[62] de Borst, R. & Verhoosel, C. V. (2016). Gradient damage vs phase-field approaches for fracture: Similarities and differences. *Computer Methods in Applied Mechanics and Engineering*, 312, 78–94.

[63] De Lorenzis, L., McBride, A., & Reddy, B. D. (2016). Phase-field modelling of fracture in single crystal plasticity. *GAMM-Mitteilungen*, 39(1), 7–34.

[64] de Souza Neto, E. A., Peric, D., & Owen, D. R. (2011). *Computational methods for plasticity: theory and applications*. John Wiley & Sons.

[65] Dean, A., Reinoso, J., Jha, N., Mahdi, E., & Rolfes, R. (2020). A phase field approach for ductile fracture of short fibre reinforced composites. *Theoretical and Applied Fracture Mechanics*, 106, 102495.

[66] del Busto, S., Betegón, C., & Martínez-Pañeda, E. (2017). A cohesive zone framework for environmentally assisted fatigue. *Engineering Fracture Mechanics*, 185, 210–226.

[67] Dinachandra, M. & Alankar, A. (2020). A phase-field study of crack propagation and branching in functionally graded materials using explicit dynamics. *Theoretical and Applied Fracture Mechanics*, 109, 102681.

[68] Dittmann, M., Krüger, M., Schmidt, F., Schuß, S., & Hesch, C. (2018). Variational modeling of thermomechanical fracture and anisotropic frictional mortar contact problems with adhesion. *Computational Mechanics*, 63, 571–591.

[69] Doan, D. H., Bui, T. Q., Duc, N. D., & Fushinobu, K. (2016). Hybrid phase field simulation of dynamic crack propagation in functionally graded glass-filled epoxy. *Composites Part B: Engineering*, 99, 266–276.

[70] Doan, D. H., Bui, T. Q., Van Do, T., & Duc, N. D. (2017). A rate-dependent hybrid phase field model for dynamic crack propagation. *Journal of Applied Physics*, 122(11).

[71] Duda, F. P., Ciarbonetti, A., Sánchez, P. J., & Huespe, A. E. (2015). A phase-field/gradient damage model for brittle fracture in elastic–plastic solids. *International Journal of Plasticity*, 65, 269–296.

[72] Egger , A., Pillai , U., Agathos , K., Kakouris , E., Chatzi , E., Aschroft , I. A., & Triantafyllou , S. P. (2019). Discrete and phase field methods for linear elastic fracture mechanics: A comparative study and state-of-the-art review. *Applied Sciences*, 9(12).

[73] Emdadi, A., Fahrenholtz, W. G., Hilmas, G. E., & Asle Zaeem, M. (2018). A modified phase-field model for quantitative simulation of crack propagation in single-phase and multi-phase materials. *Engineering Fracture Mechanics*, 200, 339–354.

[74] Engwer, C. & Schumacher, L. (2017). A phase field approach to pressurized fractures using discontinuous galerkin methods. *Mathematics and Computers in Simulation*, 137, 266–285.

[75] Esmaeilzadeh, P., Behnagh, R. A., Pour, M. A. M., Zhang, X., & Liao, Y. (2020a). Phase-field modeling of fracture and crack growth in friction stir processed pure copper. *The International Journal of Advanced Manufacturing Technology*, 109(9), 2377–2392.

[76] Esmaeilzadeh, P., Behnagh, R. A., Pour, M. A. M., Zhang, X., & Liao, Y. (2020b). Phase-field modeling of fracture and crack growth in friction stir processed pure copper. *The International Journal of Advanced Manufacturing Technology*, 109(9), 2377–2392.

[77] Espinosa, H. D. & Zavattieri, P. D. (2003). A grain level model for the study of failure initiation and evolution in polycrystalline brittle materials. part i: Theory and numerical implementation. *Mechanics of Materials*, 35(3-6), 333–364.

[78] Evans, A. (1978). Microfracture from thermal expansion anisotropy—i. single phase systems. *Acta Metallurgica*, 26(12), 1845–1853.

[79] Fan, M., Jin, Y., & Thomas, W. (2019). A phase-field description for mixed-mode fracture propagation. *Hannover : Institutionelles Repositorium der Leibniz Universität Hannover*, (pp. 1–40).

[80] Fang, J., Wu, C., Rabczuk, T., Wu, C., Ma, C., Sun, G., & Li, Q. (2019a). Phase field fracture in elasto-plastic solids: Abaqus implementation and case studies. *Theoretical and Applied Fracture Mechanics*, 103, 102252.

[81] Fang, J., Wu, C., Rabczuk, T., Wu, C., Ma, C., Sun, G., & Li, Q. (2019b). Phase field fracture in elasto-plastic solids: Abaqus implementation and case studies. *Theoretical and Applied Fracture Mechanics*, 103, 102252.

[82] Farrell, P. & Maurini, C. (2017). Linear and nonlinear solvers for variational phase-field models of brittle fracture. *International Journal for Numerical Methods in Engineering*, 109(5), 648–667.

[83] Fei, F. & Choo, J. (2020). A phase-field method for modeling cracks with frictional contact. *International Journal for Numerical Methods in Engineering*, 121(4), 740–762.

[84] Feng, D. & Wu, J. (2018). Phase-field regularized cohesive zone model (czm) and size effect of concrete. *Engineering Fracture Mechanics*, 197, 66–79.

[85] Ferreira, A. J. (2009). *MATLAB codes for finite element analysis*. Springer-Verlag.

[86] Ferro, N., Micheletti, S., & Perotto, S. (2018). Anisotropic mesh adaptation for crack propagation induced by a thermal shock in 2D. *Computer Methods in Applied Mechanics and Engineering*, 331, 138–158.

[87] Francfort, G. A. & Marigo, J.-J. (1998). Revisiting brittle fracture as an energy minimization problem. *Journal of the Mechanics and Physics of Solids*, 46(8), 1319–1342.

[88] Freddi, F. & Iurlano, F. (2017). Numerical insight of a variational smeared approach to cohesive fracture. *Journal of the Mechanics and Physics of Solids*, 98, 156–171.

[89] Freddi, F. & Royer-Carfagni, G. (2010). Regularized variational theories of fracture: A unified approach. *Journal of the Mechanics and Physics of Solids*, 58(8), 1154–1174.

[90] Fu, G., Zhou, S., & Qi, L. (2020). On the strain gradient elasticity theory for isotropic materials. *International Journal of Engineering Science*, 154, 103348.

[91] Gabriele, S., Rizzi, N., & Varano, V. (2014). A 1d higher gradient model derived from koiter's shell theory. *Mathematics and Mechanics of Solids*, 21(6), 737–746.

[92] Geelen, R. J. M., Liu, Y., Dolbow, J. E., & Rodriguez-Ferran, A. (2018). An optimization-based phase-field method for continuous-discontinuous crack propagation. *International Journal for Numerical Methods in Engineering*, 116, 1–20.

[93] Geraci, G. & Aliabadi, M. H. (2018a). Micromechanical modeling of cohesive thermoelastic steady state and transient cracking in polycrystalline materials. *International Journal for Numerical Methods in Engineering*, 117, 1205–1233.

[94] Geraci, G. & Aliabadi, M. H. (2018b). Micromechanical modelling of cohesive thermoelastic cracking in orthotropic polycrystalline materials. *Computer Methods in Applied Mechanics and Engineering*, 339, 567–590.

[95] Gerasimov, T. & De Lorenzis, L. (2016). A line search assisted monolithic approach for phase-field computing of brittle fracture. *Computer Methods in Applied Mechanics and Engineering*, 312, 276–303.

[96] Geyer, J. F. & Nemat-Nasser, S. (1982). Experimental investigation of thermally induced interacting cracks in brittle solids. *International Journal of Solids and Structures*, 18(4), 349–356.

[97] Glüge, R. (2019). A c1 incompatible mode element formulation for strain gradient elasticity. In *Higher Gradient Materials and Related Generalized Continua* (pp. 95–120). Springer-Verlag.

[98] Goswami, S., Anitescu, C., Chakraborty, S., & Rabczuk, T. (2020a). Transfer learning enhanced physics informed neural network for phase-field modeling of fracture. *Theoretical and Applied Fracture Mechanics*, 106, 102447.

[99] Goswami, S., Anitescu, C., & Rabczuk, T. (2020b). Adaptive fourth-order phase field analysis for brittle fracture. *Computer Methods in Applied Mechanics and Engineering*, 361, 112808.

[100] Goswami, S., Anitescu, C., & Rabczuk, T. (2020c). Adaptive fourth-order phase field analysis using deep energy minimization. *Theoretical and Applied Fracture Mechanics*, 107, 102527.

[101] Griffith, A. A. (1921). The phenomena of rupture and flow in solids. *Philosophical Transactions of the Royal Society A: Mathematical, Physical and Engineering Sciences*, 221(582-593), 163–198.

[102] Gültekin, O., Dal, H., & Holzapfel, G. A. (2016). A phase-field approach to model fracture of arterial walls: Theory and finite element analysis. *Computer Methods in Applied Mechanics and Engineering*, 312, 542–566.

[103] Gültekin, O., Dal, H., & Holzapfel, G. A. (2018). Numerical aspects of anisotropic failure in soft biological tissues favor energy-based criteria: A rate-dependent anisotropic crack phase-field model. *Computer Methods in Applied Mechanics and Engineering*, 331, 23–52.

[104] Hansen-Dörr, A. C., Brummund, J., & Kästner, M. (2021). Phase-field modeling of fracture in heterogeneous materials: jump conditions, convergence and crack propagation. *Archive of Applied Mechanics*, 91(2), 579–596.

[105] Harutyunyan, H. (2019). *PhD Dissertation and Doktorarbeit LaTeX Template for FAU (Friedrich-Alexander-Universität Erlangen-Nürnberg)*. Overleaf.

[106] Haveroth, G. A., Moraes, E. A. B. d., Boldrini, J. L., & Bittencourt, M. L. (2018). Comparison of semi and fully-implicit time integration schemes applied to a damage and fatigue phase field model. *Latin American Journal of Solids and Structures*, 15(5).

[107] Heister, T., Wheeler, M. F., & Wick, T. (2015). A primal-dual active set method and predictor-corrector mesh adaptivity for computing fracture propagation using a phase-field approach. *Computer Methods in Applied Mechanics and Engineering*, 290, 466–495.

[108] Heister, T. & Wick, T. (2018). Parallel solution, adaptivity, computational convergence, and open-source code of 2d and 3d pressurized phase-field fracture problems. *Pamm*, 18(1).

[109] Heister, T. & Wick, T. (2020). pfm-cracks: A parallel-adaptive framework for phase-field fracture propagation. *Software Impacts*, 6, 100045.

[110] Henry, H. & Levine, H. (2004). Dynamic instabilities of fracture under biaxial strain using a phase field model. *Physical Review Letters*, 93(10), 105504.

[111] Hernandez Padilla, C. A. & Markert, B. (2015). A coupled ductile fracture phase-field model for crystal plasticity. *Continuum Mechanics and Thermodynamics*, 29(4), 1017–1026.

[112] Hesch, C., Schuß, S., Dittmann, M., Franke, M., & Weinberg, K. (2016). Isogeometric analysis and hierarchical refinement for higher-order phase-field models. *Computer Methods in Applied Mechanics and Engineering*, 303, 185–207.

[113] Hirshikesh, N. S. & Annabattula, R. K. (2019). Modeling crack propagation in variable stiffness composite laminates using the phase field method. *Composite Structures*, 209, 424–433.

[114] Hofacker, M. & Miehe, C. (2012). Continuum phase field modeling of dynamic fracture: variational principles and staggered fe implementation. *International Journal of Fracture*, 178(1-2), 113–129.

[115] Hofacker, M. & Miehe, C. (2013). A phase field model of dynamic fracture: Robust field updates for the analysis of complex crack patterns. *International Journal for Numerical Methods in Engineering*, 93(3), 276–301.

[116] Honda, S., Ogihara, Y., Kishi, T., Hashimoto, S., & Iwamoto, Y. (2009). Estimation of thermal shock resistance of fine porous alumina by infrared radiation heating method. *Journal of the Ceramic Society of Japan*, 117(1371), 1208–1215.

[117] Honda, S., Suzuki, T., Nishikawa, T., Awaji, H., Akimune, Y., & Hirosaki, N. (2002). Estimation of thermal shock properties for silicon nitride having high thermal conductivity. *Journal of the Ceramic Society of Japan*, 110(1277), 38–43.

[118] Hughes, T. J. (2012). *The finite element method: linear static and dynamic finite element analysis*. Courier Corporation.

[119] Hughes, T. J., Cottrell, J. A., & Bazilevs, Y. (2005). Isogeometric analysis: Cad, finite elements, nurbs, exact geometry and mesh refinement. *Computer methods in applied mechanics and engineering*, 194(39-41), 4135–4195.

[120] Huynh, G. D., Zhuang, X., & Nguyen-Xuan, H. (2018). Implementation aspects of a phase-field approach for brittle fracture. *Frontiers of Structural and Civil Engineering*, 13, 417–428.

[121] Irwin, G. R. (1958). Fracture. *Elasticity and Plasticity / Elastizität und Plastizität*.

[122] Jenkins, D. R. (2005). Optimal spacing and penetration of cracks in a shrinking slab. *Physical review/E, Statistical, nonlinear, and soft matter physics*, 71, 056117.

[123] Jeong, H., Signetti, S., Han, T.-S., & Ryu, S. (2018). Phase field modeling of crack propagation under combined shear and tensile loading with hybrid formulation. *Computational Materials Science*, 155, 483–492.

[124] Jiang, C. P., Wu, X. F., Li, J., Song, F., Shao, Y. F., Xu, X. H., & Yan, P. (2012). A study of the mechanism of formation and numerical simulations of crack patterns in ceramics subjected to thermal shock. *Acta Materialia*, 60(11), 4540–4550.

[125] Kalthoff, J. F. (2000). Modes of dynamic shear failure in solids. *International Journal of Fracture*, 101(1/2), 1–31.

[126] Kiendl, J., Ambati, M., De Lorenzis, L., Gomez, H., & Reali, A. (2016). Phase-field description of brittle fracture in plates and shells. *Computer Methods in Applied Mechanics and Engineering*, 312, 374–394.

[127] Kikis, G., Ambati, M., De Lorenzis, L., & Klinkel, S. (2019). A phase field model of brittle fracture for an isogeometric reissner-mindlin shell formulation. *Pamm*.

[128] Klinsmann, M., Rosato, D., Kamlah, M., & McMeeking, R. M. (2015). An assessment of the phase field formulation for crack growth. *Computer Methods in Applied Mechanics and Engineering*, 294, 313–330.

[129] Klinsmann, M., Rosato, D., Kamlah, M., & McMeeking, R. M. (2016). Modeling crack growth during li insertion in storage particles using a fracture phase field approach. *Journal of the Mechanics and Physics of Solids*, 92, 313–344.

[130] Korelc, J. & Wriggers, P. (2016). Automation of the finite element method. *Springer-Verlag*.

[131] Kristensen, P. K., Niordson, C. F., & Martínez-Pañeda, E. (2020). A phase field model for elastic-gradient-plastic solids undergoing hydrogen embrittlement. *Journal of the Mechanics and Physics of Solids*, 143, 104093.

[132] Kuhn, C. & Müller, R. (2009). Phase field simulation of thermomechanical fracture. *Pamm*, 9(1), 191–192.

[133] Kuhn, C. & Müller, R. (2010). A continuum phase field model for fracture. *Engineering Fracture Mechanics*, 77(18), 3625–3634.

[134] Kuhn, C. & Müller, R. (2014). Simulation of size effects by a phase field model for fracture. *Theoretical and Applied Mechanics Letters*, 4(5).

[135] Kuhn, C. & Müller, R. (2016). A discussion of fracture mechanisms in heterogeneous materials by means of configurational forces in a phase field fracture model. *Computer Methods in Applied Mechanics and Engineering*, 312, 95–116.

[136] Kuhn, C., Noll, T., & Müller, R. (2016). On phase field modeling of ductile fracture. *GAMM-Mitteilungen*, 39(1), 35–54.

[137] Kuhn, C., Schlüter, A., & Müller, R. (2015). On degradation functions in phase field fracture models. *Computational Materials Science*, 108, 374–384.

[138] Läpple, V. (2016). *Einführung in die Festigkeitslehre: Lehr- und Übungsbuch*. Springer-Verlag.

[139] Lee, S., Mikelić, A., Wheeler, M. F., & Wick, T. (2016). Phase-field modeling of proppant-filled fractures in a poroelastic medium. *Computer Methods in Applied Mechanics and Engineering*, 312, 509–541.

[140] Lepillier, B., Yoshioka, K., Parisio, F., Bakker, R., & Bruhn, D. (2020). Variational phase-field modeling of hydraulic fracture interaction with natural fractures and application to enhanced geothermal systems. *Journal of Geophysical Research: Solid Earth*, 125(7).

[141] Lesičar, T., Tonković, Z., & Sorić, J. (2014). A second-order two-scale homogenization procedure using c^1 macrolevel discretization. *Computational Mechanics*, 54(2), 425–441.

[142] Li, B., Peco, C., Millán, D., Arias, I., & Arroyo, M. (2015a). Phase-field modeling and simulation of fracture in brittle materials with strongly anisotropic surface energy. *International Journal for Numerical Methods in Engineering*, 102(3-4), 711–727.

[143] Li, D., Wang, R., Wang, X., & Li, W. (2020). Simulation of the thermal shock cracking behaviors of ceramics under water quenching for 3-dimension conditions. *European Journal of Mechanics-A/Solids*, 84, 104080.

[144] Li, J., Song, F., & Jiang, C. (2015b). A non-local approach to crack process modeling in ceramic materials subjected to thermal shock. *Engineering Fracture Mechanics*, 133, 85–98.

[145] Li, P., Zhu, Q., Gu, S., & Tao, N. (2018). A phase field method to simulate crack nucleation and crack propagation in rock-like materials. *Gong Cheng Li Xue/Engineering Mechanics*.

[146] Li, Z. & Bradt, R. C. (1986). Thermal expansion of the hexagonal (6h) polytype of silicon carbide. *Journal of the American Ceramic Society*, 69(12), 863–866.

[147] Li, Z. & Bradt, R. C. (1987). Thermal expansion and thermal expansion anisotropy of sic polytypes. *Journal of the American Ceramic Society*, 70(7), 445–448.

[148] Lin, L., Wang, X., & Zeng, X. (2015). The role of cohesive zone properties on intergranular to transgranular fracture transition in polycrystalline solids. *International Journal of Damage Mechanics*, 26(3), 379–394.

[149] Liu, C. & Thompson, D. G. (2014). Crack initiation and growth in pbx 9502 high explosive subject to compression. *Journal of Applied Mechanics*, 81(10).

[150] Liu, G., Li, Q., Msekh, M. A., & Zuo, Z. (2016). Abaqus implementation of monolithic and staggered schemes for quasi-static and dynamic fracture phase-field model. *Computational Materials Science*, 121, 35–47.

[151] Liu, J., Liang, X., Xue, Y., Fu, Y., Yao, K., & Dou, F. (2020). Investigation on crack initiation and propagation in hydraulic fracturing of bedded shale by hybrid phase-field modeling. *Theoretical and Applied Fracture Mechanics*, 108, 102651.

[152] Liu, Z. & Juhre, D. (2018). Phase-field modelling of crack propagation in anisotropic polycrystalline materials. *Technische Mechanik*, 38, 286–299.

[153] Liu, Z. & Juhre, D. (2019). Adaptive phase-field model of mixed mode fracture in compression and its experimental verification. *14. Magdeburger Maschinenbautage 2019 - MAGDEBURGER INGENIEURTAGE*.

[154] Lo, Y.-S., Borden, M. J., Ravi-Chandar, K., & Landis, C. M. (2019). A phase-field model for fatigue crack growth. *Journal of the Mechanics and Physics of Solids*, 132, 103684.

[155] Loew, P. J., Poh, L. H., Peters, B., & Beex, L. A. (2020). Accelerating fatigue simulations of a phase-field damage model for rubber. *Computer Methods in Applied Mechanics and Engineering*, 370, 113247.

[156] Mandal, T. K., Nguyen, V. P., Wu, J.-Y., Nguyen-Thanh, C., & de Vaucorbeil, A. (2021). Fracture of thermo-elastic solids: Phase-field modeling and new results with an efficient monolithic solver. *Computer Methods in Applied Mechanics and Engineering*, 376, 113648.

[157] Mang, K., Walloth, M., Wick, T., & Wollner, W. (2019). Mesh adaptivity for quasi-static phase-field fractures based on a residual-type a posteriori error estimator. *GAMM-Mitteilungen*, 43(1), e202000003.

[158] Martínez-Pañeda, E. & Betegón, C. (2015). Modeling damage and fracture within strain-gradient plasticity. *International Journal of Solids and Structures*, 59, 208–215.

[159] Martínez-Pañeda, E., Golahmar, A., & Niordson, C. F. (2018). A phase field formulation for hydrogen assisted cracking. *Computer Methods in Applied Mechanics and Engineering*, 342, 742–761.

[160] Martínez-Pañeda, E. & Niordson, C. F. (2016). On fracture in finite strain gradient plasticity. *International Journal of Plasticity*, 80, 154–167.

[161] Maurini, C., Bourdin, B., Gauthier, G., & Lazarus, V. (2013). Crack patterns obtained by unidirectional drying of a colloidal suspension in a capillary tube: experiments and numerical simulations using a two-dimensional variational approach. *International Journal of Fracture*, 184(1-2), 75–91.

[162] May, S., Vignollet, J., & de Borst, R. (2015). A numerical assessment of phase-field models for brittle and cohesive fracture: γ-convergence and stress oscillations. *European Journal of Mechanics-A/Solids*, 52, 72–84.

[163] Mesgarnejad, A., Bourdin, B., & Khonsari, M. M. (2015). Validation simulations for the variational approach to fracture. *Computer Methods in Applied Mechanics and Engineering*, 290, 420–437.

[164] Miao, X., Kolditz, O., & Nagel, T. (2019). Modelling thermal performance degradation of high and low-temperature solid thermal energy storage due to cracking processes using a phase-field approach. *Energy Conversion and Management*, 180, 977–989.

[165] Miehe, C. (1998). Comparison of two algorithms for the computation of fourth-order isotropic tensor functions. *Computers & structures*, 66(1), 37–43.

[166] Miehe, C., Hofacker, M., & Welschinger, F. (2010a). A phase field model for rate-independent crack propagation: Robust algorithmic implementation based on operator splits. *Computer Methods in Applied Mechanics and Engineering*, 199(45-48), 2765–2778.

[167] Miehe, C. & Lambrecht, M. (2001). Algorithms for computation of stresses and elasticity moduli in terms of seth–hill's family of generalized strain tensors. *Communications in numerical methods in engineering*, 17(5), 337–353.

[168] Miehe, C., Schänzel, L.-M., & Ulmer, H. (2015). Phase field modeling of fracture in multi-physics problems. part i. balance of crack surface and failure criteria for brittle crack propagation in thermo-elastic solids. *Computer Methods in Applied Mechanics and Engineering*, 294, 449–485.

[169] Miehe, C., Welschinger, F., & Hofacker, M. (2010b). Thermodynamically consistent phase-field models of fracture: Variational principles and multi-field fe implementations. *International Journal for Numerical Methods in Engineering*, 83(10), 1273–1311.

[170] Minh, P. P., Van Do, T., Duc, D. H., & Duc, N. D. (2018). The stability of cracked rectangular plate with variable thickness using phase field method. *Thin-Walled Structures*, 129, 157–165.

[171] Molnár, G. & Gravouil, A. (2017). 2D and 3D abaqus implementation of a robust staggered phase-field solution for modeling brittle fracture. *Finite Elements in Analysis and Design*, 130, 27–38.

[172] Msekh, M. (2017). *Phase Field Modeling for Fracture with Applications to Homogeneous and Heterogeneous Materials*. Bauhaus-Universität Weimar.

[173] Msekh, M. A., Cuong, N. H., Zi, G., Areias, P., Zhuang, X., & Rabczuk, T. (2018). Fracture properties prediction of clay/epoxy nanocomposites with interphase zones using a phase field model. *Engineering Fracture Mechanics*, 188, 287–299.

[174] Msekh, M. A., Sargado, J. M., Jamshidian, M., Areias, P. M., & Rabczuk, T. (2015). Abaqus implementation of phase-field model for brittle fracture. *Computational Materials Science*, 96, 472–484.

[175] Müller, R. (2016). *A Phase Field Model for the Evolution of Martensite Microstructures in Metastable Austenites*. Technische Universität Kaiserslautern.

[176] Mulville, D. R., Mast, P. W., & Vaishnav, R. N. (1976). Strain energy release rate for interfacial cracks between dissimilar media. *Engineering Fracture Mechanics*, 8(3), 555–565.

[177] Na, S. & Sun, W. (2018). Computational thermomechanics of crystalline rock, part i: A combined multi-phase-field/crystal plasticity approach for single crystal simulations. *Computer Methods in Applied Mechanics and Engineering*, 338, 657–691.

[178] Nagaraja, S. (2018). Phase-field modeling of brittle fracture with multi-level hp-fem and the finite cell method. *Master Thesis*.

[179] Nagaraja, S., Elhaddad, M., Ambati, M., Kollmannsberger, S., De Lorenzis, L., & Rank, E. (2018). Phase-field modeling of brittle fracture with multi-level hp-fem and the finite cell method. *Computational Mechanics*, 63, 1283–1300.

[180] Naumenko, K. & Altenbach, H. (2016). *Modeling High Temperature Materials Behavior for Structural Analysis*. Advanced Structured Materials. Springer-Verlag.

[181] Nguyen, C. T. & Oterkus, S. (2019). Peridynamics formulation for beam structures to predict damage in offshore structures. *Ocean Engineering*, 173, 244–267.

[182] Nguyen, T. T., Bolivar, J., Shi, Y., Réthoré, J., King, A., Fregonese, M., Adrien, J., Buffiere, J. Y., & Baietto, M. C. (2018). A phase field method for modeling anodic dissolution induced stress corrosion crack propagation. *Corrosion Science*, 132, 146–160.

[183] Nguyen, T. T., Réthoré, J., & Baietto, M.-C. (2017a). Phase field modelling of anisotropic crack propagation. *European Journal of Mechanics-A/Solids*, 65, 279–288.

[184] Nguyen, T.-T., Réthoré, J., Yvonnet, J., & Baietto, M.-C. (2017b). Multi-phase-field modeling of anisotropic crack propagation for polycrystalline materials. *Computational Mechanics*, 60(2), 289–314.

[185] Nguyen, T.-T., Waldmann, D., & Bui, T. Q. (2019). Computational chemo-thermo-mechanical coupling phase-field model for complex fracture induced by early-age shrinkage and hydration heat in cement-based materials. *Computer Methods in Applied Mechanics and Engineering*, 348, 1–28.

[186] Nguyen, T. T., Yvonnet, J., Bornert, M., Chateau, C., Sab, K., Romani, R., & Le Roy, R. (2016). On the choice of parameters in the phase field method for simulating crack initiation with experimental validation. *International Journal of Fracture*, 197(2), 213–226.

[187] Nguyen, T. T., Yvonnet, J., Waldmann, D., & He, Q. C. (2020). Implementation of a new strain split to model unilateral contact within the phase field method. *International Journal for Numerical Methods in Engineering*, 121(21), 4717–4733.

[188] Ooi, E. T., Song, C., & Natarajan, S. (2018). A scaled boundary finite element formulation for poroelasticity. *International Journal for Numerical Methods in Engineering*, 114(8), 905–929.

[189] Özdemir, I., Brekelmans, W. A. M., & Geers, M. G. D. (2010). A thermo-mechanical cohesive zone model. *Computational Mechanics*, 46(5), 735–745.

[190] Paggi, M., Corrado, M., & Reinoso, J. (2018). Fracture of solar-grade anisotropic polycrystalline silicon: A combined phase field–cohesive zone model approach. *Computer Methods in Applied Mechanics and Engineering*, 330, 123–148.

[191] Paggi, M. & Reinoso, J. (2017). Revisiting the problem of a crack impinging on an interface:a modeling framework for the interaction between the phase field approach for brittle fracture and the interface cohesive zone model. *Computer Methods in Applied Mechanics and Engineering*, 321, 145–172.

[192] Papazafeiropoulos, G., Muñiz-Calvente, M., & Martínez-Pañeda, E. (2017). Abaqus2matlab: A suitable tool for finite element post-processing. *Advances in Engineering Software*, 105, 9–16.

[193] Parisch, H. (2003). *Festkörper-Kontinuumsmechanik*. Springer-Verlag.

[194] Park, K. & Paulino, G. H. (2011). Cohesive zone models: A critical review of traction-separation relationships across fracture surfaces. *Applied Mechanics Reviews*, 64(6).

[195] Peerlings, R. H. J., De Borst, R., Brekelmans, W. A. M., & De Vree, J. H. P. (1996). Gradient enhanced damage for quasi-brittle materials. *International Journal for Numerical Methods in Engineering*, 39(19), 3391–3403.

[196] Pillai, U., Triantafyllou, S., Essa, Y., & de la Escalera, F. M. (2020). An anisotropic cohesive phase field model to model quasi-brittle fractures in thin fibre-reinforced composites. *Composite Structures*, (pp. 112635).

[197] Portela, A., Aliabadi, M. H., & Rooke, D. P. (1992). The dual boundary element method: Effective implementation for crack problems. *International Journal for Numerical Methods in Engineering*, 33(6), 1269–1287.

[198] Portela, A., Aliabadi, M. H., & Rooke, D. P. (1993). Dual boundary element incremental analysis of crack propagation. *Computers & Structures*, 46(2), 237–247.

[199] Prasad, N. N. V., Aliabadi, M. H., & Rooke, D. P. (1994a). The dual boundary element method for thermoelastic crack problems. *International Journal of Fracture*, 66(3), 255–272.

[200] Prasad, N. N. V., Aliabadi, M. H., & Rooke, D. P. (1994b). Incremental crack growth in thermoelastic problems. *International Journal of Fracture*, 66(3), R45–R50.

[201] Prasad, N. N. V., Aliabadi, M. H., & Rooke, D. P. (1996). The dual boundary element method for transient thermoelastic crack problems. *International Journal of Solids and Structures*, 33(19), 2695–2718.

[202] Qian, J. & Li, S. (2011). Application of multiscale cohesive zone model to simulate fracture in polycrystalline solids. *Journal of Engineering Materials and Technology*, 133(1).

[203] Qu, Z., Cheng, X., He, R., Pei, Y., Zhang, R., & Fang, D. (2016). Rapid heating thermal shock behavior study of cvd zns infrared window material: Numerical and experimental study. *Journal of Alloys and Compounds*, 682, 565–570.

[204] Rabczuk, T., Song, J.-H., Zhuang, X., & Anitescu, C. (2019). *Extended finite element and meshfree methods*. Academic Press.

[205] Raghu, P., Rajagopal, A., Jalan, S., & Reddy, J. (2020). Modeling of brittle fracture in thick plates subjected to transient dynamic loads using a hybrid phase field model. *Meccanica*, (pp. 1–18).

[206] Rangaraj, S. & Kokini, K. (2004). A study of thermal fracture in functionally graded thermal barrier coatings using a cohesive zone model. *Journal of Engineering Materials and Technology*, 126(1), 103–115.

[207] Reddy, J. & Gartling, D. (2010). *The Finite Element Method in Heat Transfer and Fluid Dynamics*. Applied and Computational Mechanics. CRC Press.

[208] Reinoso, J. & Paggi, M. (2014). A consistent interface element formulation for geometrical and material nonlinearities. *Computational Mechanics*, 54(6), 1569–1581.

[209] Reinoso, J., Paggi, M., & Linder, C. (2017). Phase field modeling of brittle fracture for enhanced assumed strain shells at large deformations: formulation and finite element implementation. *Computational Mechanics*, 59(6), 981–1001.

[210] Ren, H., Zhuang, X., & Rabczuk, T. (2020). A nonlocal operator method for solving partial differential equations. *Computer Methods in Applied Mechanics and Engineering*, 358, 112621.

[211] Rice, R. W. & Pohanka, R. C. (1979). Grain-size dependence of spontaneous cracking in ceramics. *Journal of the American Ceramic Society*, 62(11-12), 559–563.

[212] Richard, H. A. & Sander, M. (2016). Fatigue crack growth. *Springer-Verlag*.

[213] Rodriguez, P., Ulloa, J., Samaniego, C., & Samaniego, E. (2018). A variational approach to the phase field modeling of brittle and ductile fracture. *International Journal of Mechanical Sciences*, 144, 502–517.

[214] Rokhi, M. M. & Shariati, M. (2013). Implementation of the extended finite element method for coupled dynamic thermoelastic fracture of a functionally graded cracked layer. *Journal of the Brazilian Society of Mechanical Sciences and Engineering*, 35(2), 69–81.

[215] Santillá n, D., Mosquera, J. C., & Cueto-Felgueroso, L. (2017). Phase-field model for brittle fracture. validation with experimental results and extension to dam engineering problems. *Engineering Fracture Mechanics*, 178, 109–125.

[216] Sapora, A. & Paggi, M. (2013). A coupled cohesive zone model for transient analysis of thermoelastic interface debonding. *Computational Mechanics*, 53(4), 845–857.

[217] Sargado, J. M., Keilegavlen, E., Berre, I., & Nordbotten, J. M. (2018). High-accuracy phase-field models for brittle fracture based on a new family of degradation functions. *Journal of the Mechanics and Physics of Solids*, 111, 458–489.

[218] Sarkar, S., Singh, I., & Mishra, B. (2020). A thermo-mechanical gradient enhanced damage method for fracture. *Computational Mechanics*, 66(6), 1399–1426.

[219] Schänzel, L. (2015). *Phase Field Modeling of Fracture in Rubbery and Glassy Polymers at Finite Thermo-Viscoelastic Deformations*. Universität Stuttgart.

[220] Schlüter, A. (2018). *Phase Field Modeling of Dynamic Brittle Fracture*. Technische Universität Kaiserslautern.

[221] Schlüter, A., Kuhn, C., & Müller, R. (2014a). Phase field approximation of dynamic brittle fracture. *Pamm*, 14(1), 143–144.

[222] Schlüter, A., Kuhn, C., & Müller, R. (2017). Simulation of laser-induced controlled fracturing utilizing a phase field model. *Journal of Computing and Information Science in Engineering*, 17(2).

[223] Schlüter, A., Kuhn, C., Müller, R., Tomut, M., Trautmann, C., Weick, H., & Plate, C. (2015). Phase field modelling of dynamic thermal fracture in the context of irradiation damage. *Continuum Mechanics and Thermodynamics*, 29(4), 977–988.

[224] Schlüter, A., Willenbücher, A., Kuhn, C., & Müller, R. (2014b). Phase field approximation of dynamic brittle fracture. *Computational Mechanics*, 54(5), 1141–1161.

[225] Schneider, D., Schoof, E., Huang, Y., Selzer, M., & Nestler, B. (2016). Phase-field modeling of crack propagation in multiphase systems. *Computer Methods in Applied Mechanics and Engineering*, 312, 186–195.

[226] Schreiber, C., Kuhn, C., Müller, R., & Zohdi, T. (2020). A phase field modeling approach of cyclic fatigue crack growth. *International Journal of Fracture*, 225(1), 89–100.

[227] Schröder, J., Wick, T., Reese, S., Wriggers, P., Müller, R., Kollmannsberger, S., Kästner, M., Schwarz, A., Igelbüscher, M., Viebahn, N., et al. (2021). A selection of benchmark problems in solid mechanics and applied mathematics. *Archives of Computational Methods in Engineering*, 28(2), 713–751.

[228] Seiler, M., Linse, T., Hantschke, P., & Kästner, M. (2020). An efficient phase-field model for fatigue fracture in ductile materials. *Engineering Fracture Mechanics*, 224, 106807.

[229] Sfantos, G. & Aliabadi, M. (2007a). Multi-scale boundary element modelling of material degradation and fracture. *Computer Methods in Applied Mechanics and Engineering*, 196(7), 1310–1329.

[230] Sfantos, G. K. & Aliabadi, M. H. (2007b). A boundary cohesive grain element formulation for modelling intergranular microfracture in polycrystalline brittle materials. *International Journal for Numerical Methods in Engineering*, 69(8), 1590–1626.

[231] Shao, Y., Zhang, Y., Xu, X., Zhou, Z., Li, W., Liu, B., & Jin, Z. H. (2011). Effect of crack pattern on the residual strength of ceramics after quenching. *Journal of the American Ceramic Society*, 94(9), 2804–2807.

[232] Shen, Y., Mollaali, M., Li, Y., Ma, W., & Jiang, J. (2018). Implementation details for the phase field approaches to fracture. *Journal of Shanghai Jiaotong University (Science)*, 23(1), 166–174.

[233] Shiah, Y. & Tan, C. (1997). Bem treatment of two-dimensional anisotropic field problems by direct domain mapping. *Engineering Analysis with Boundary Elements*, 20(4), 347–351.

[234] Shiah, Y. & Tan, C. (1999). Exact boundary integral transformation of the thermoelastic domain integral in bem for general 2d anisotropic elasticity. *Computational Mechanics*, 23(1), 87–96.

[235] Sicsic, P., Marigo, J.-J., & Maurini, C. (2014). Initiation of a periodic array of cracks in the thermal shock problem: A gradient damage modeling. *Journal of the Mechanics and Physics of Solids*, 63, 256–284.

[236] Sigmund, O. (2001). A 99 line topology optimization code written in matlab. *Structural and multidisciplinary optimization*, 21(2), 120–127.

[237] Simo, J. C. & Hughes, T. J. (2006). *Computational inelasticity*, volume 7. Springer Science & Business Media.

[238] Singh, N., Verhoosel, C. V., & van Brummelen, E. H. (2017). Finite element simulation of pressure-loaded phase-field fractures. *Meccanica*, 53(6), 1513–1545.

[239] Smith, M. (2009). *ABAQUS/Standard User's Manual, Version 6.9*. United States: Dassault Systèmes Simulia Corp.

[240] Sollero, P. & Aliabadi, M. H. (1995). Anisotropic analysis of cracks in composite laminates using the dual boundary element method. *Composite Structures*, 31(3), 229–233.

[241] Song, Y. & Voyiadjis, G. Z. (2020). Strain gradient finite element model for finite deformation theory: size effects and shear bands. *Computational Mechanics*, 65(5), 1219–1246.

[242] Sridhar, N., Yang, W., Srolovitz, D. J., & Fuller, E. R. (1994). Microstructural mechanics model of anisotropic-thermal-expansion-induced microcracking. *Journal of the American Ceramic Society*, 77(5), 1123–1138.

[243] Staroselsky, A., Acharya, R., & Cassenti, B. (2019). Phase field modeling of fracture and crack growth. *Engineering Fracture Mechanics*, 205, 268–284.

[244] Steinmann, P. (2013). *Linear Continuum Mechanics*. Friedrich-Alexander-Universität Erlangen-Nürnberg.

[245] Steinmann, P. (2015). *Geometrical Foundations of Continuum Mechanics*. Lecture Notes in Applied Mathematics and Mechanics. Springer-Verlag.

[246] Storm, J., Supriatna, D., & Kaliske, M. (2019). The concept of representative crack elements (rce) for phase-field fracture - anisotropic elasticity and thermoelasticity. *International Journal for Numerical Methods in Engineering*, 103, 72–99.

[247] Strobl, M.vand Seelig, T. (2016). On constitutive assumptions in phase field approaches to brittle fracture. *Procedia Structural Integrity*, 2, 3705–3712.

[248] Sukumar, N., Srolovitz, D. J., Baker, T. J., & Prévost, J. H. (2003). Brittle fracture in polycrystalline microstructures with the extended finite element method. *International Journal for Numerical Methods in Engineering*, 56(14), 2015–2037.

[249] Sumio, M. (2012). *Continuum Damage Mechanics*. Solid Mechanics and Its Applications. Springer-Verlag.

[250] Suwas, S. & Ray, R. K. (2014). *Crystallographic Texture of Materials*. Springer-Verlag.

[251] Tang, S. B., Zhang, H., Tang, C. A., & Liu, H. Y. (2016). Numerical model for the cracking behavior of heterogeneous brittle solids subjected to thermal shock. *International Journal of Solids and Structures*, 80, 520–531.

[252] Tanné, E., Li, T., Bourdin, B., Marigo, J.-J., & Maurini, C. (2018). Crack nucleation in variational phase-field models of brittle fracture. *Journal of the Mechanics and Physics of Solids*, 110, 80–99.

[253] Tarafder, P., Dan, S., & Ghosh, S. (2020). Finite deformation cohesive zone phase field model for crack propagation in multi-phase microstructures. *Computational Mechanics*, 66(3), 723–743.

[254] Tarasovs, S. & Ghassemi, A. (2014). Self-similarity and scaling of thermal shock fractures. *Physical Review E*, 90(1), 012403.

[255] Taylor, R. L. (2014). Feap-a finite element analysis program.

[256] Teichtmeister, S. & Miehe, C. (2015). Phase-field modeling of fracture in anisotropic media. *PAMM*, 15(1), 159–160.

[257] Thai, C. H., Ferreira, A., & Phung-Van, P. (2020). A nonlocal strain gradient isogeometric model for free vibration and bending analyses of functionally graded plates. *Composite Structures*, 251, 112634.

[258] Tsepoura, K. G., Papargyri-Beskou, S., Polyzos, D., & Beskos, D. E. (2002). Static and dynamic analysis of a gradient-elastic bar in tension. *Archive of Applied Mechanics*, 72(6), 483–497.

[259] Van Do, T., Doan, D. H., Duc, N. D., & Bui, T. Q. (2017). Phase-field thermal buckling analysis for cracked functionally graded composite plates considering neutral surface. *Composite Structures*, 182, 542–548.

[260] Vignollet, J., May, S., de Borst, R., & Verhoosel, C. V. (2014). Phase-field models for brittle and cohesive fracture. *Meccanica*, 49(11), 2587–2601.

[261] Vu Hoai, N., Hong Doan, D., Khoa, N. M., Van Do, T., & Thi Tran, H. (2019). Phase-field buckling analysis of cracked stiffened functionally graded plates. *Composite Structures*, 217, 50–59.

[262] Wang, Q., Feng, Y. T., Zhou, W., Cheng, Y., & Ma, G. (2020a). A phase-field model for mixed-mode fracture based on a unified tensile fracture criterion. *Computer Methods in Applied Mechanics and Engineering*, 370, 113270.

[263] Wang, T., Ye, X., Liu, Z., Chu, D., & Zhuang, Z. (2019). Modeling the dynamic and quasi-static compression-shear failure of brittle materials by explicit phase field method. *Computational Mechanics*, 64(6), 1537–1556.

[264] Wang, T., Ye, X., Liu, Z., Liu, X., Chu, D., & Zhuang, Z. (2020b). A phase-field model of thermo-elastic coupled brittle fracture with explicit time integration. *Computational Mechanics*, 65(5), 1305–1321.

[265] Wcisło, B. (2017). *Large strain thermomechanical material models accounting for inelasticity, instabilities and gradient enhancement*. Cracow University of Technology.

[266] Wcisło, B. & Pamin, J. (2017). Local and non-local thermomechanical modeling of elastic-plastic materials undergoing large strains. *International Journal for Numerical Methods in Engineering*, 109(1), 102–124.

[267] Weinberg, K. & Hesch, C. (2015). A high-order finite deformation phase-field approach to fracture. *Continuum Mechanics and Thermodynamics*, 29(4), 935–945.

[268] Wick, T. (2016). Coupling fluid–structure interaction with phase-field fracture. *Journal of Computational Physics*, 327, 67–96.

[269] Wick, T. (2017). Modified newton methods for solving fully monolithic phase-field quasi-static brittle fracture propagation. *Computer Methods in Applied Mechanics and Engineering*, 325, 577–611.

[270] Willam, K., Rhee, I., & Shing, B. (2004). Interface damage model for thermomechanical degradation of heterogeneous materials. *Computer Methods in Applied Mechanics and Engineering*, 193(30-32), 3327–3350.

[271] Willner, K. (2013). *Kontinuums- und Kontaktmechanik: Synthetische und analytische Darstellung*. Springer-Verlag.

[272] Wriggers, P. (2013). *Nichtlineare finite-element-methoden*. Springer-Verlag.

[273] Wu, J., Wang, D., Lin, Z., & Qi, D. (2020). An efficient gradient smoothing meshfree formulation for the fourth-order phase field modeling of brittle fracture. *Computational Particle Mechanics*, 7(2), 193–207.

[274] Wu, J.-Y. (2017). A unified phase-field theory for the mechanics of damage and quasi-brittle failure. *Journal of the Mechanics and Physics of Solids*, 103, 72–99.

[275] Wu, J.-Y. & Cervera, M. (2016). A thermodynamically consistent plastic-damage framework for localized failure in quasi-brittle solids: Material model and strain localization analysis. *International Journal of Solids and Structures*, 88-89, 227–247.

[276] Wu, J.-Y. & Cervera, M. (2018). A novel positive/negative projection in energy norm for the damage modeling of quasi-brittle solids. *International Journal of Solids and Structures*, 139, 250–269.

[277] Wu, J.-Y. & Nguyen, V. P. (2018). A length scale insensitive phase-field damage model for brittle fracture. *Journal of the Mechanics and Physics of Solids*, 119, 20–42.

[278] Wu, T., Carpiuc-Prisacari, A., Poncelet, M., & De Lorenzis, L. (2017). Phase-field simulation of interactive mixed-mode fracture tests on cement mortar with full-field displacement boundary conditions. *Engineering Fracture Mechanics*, 182, 658–688.

[279] Wulfinghoff, S., Bayat, H. R., Alipour, A., & Reese, S. (2017). A low-order locking-free hybrid discontinuous galerkin element formulation for large deformations. *Computer Methods in Applied Mechanics and Engineering*, 323, 353–372.

[280] Xia, L., Yvonnet, J., & Ghabezloo, S. (2017). Phase field modeling of hydraulic fracturing with interfacial damage in highly heterogeneous fluid-saturated porous media. *Engineering Fracture Mechanics*, 186, 158–180.

[281] Xu, X. P. & Needleman, A. (1995). Numerical simulations of dynamic crack growth along an interface. *International Journal of Fracture*, 74(4), 289–324.

[282] Yang, Z. & Liu, H. (2020). An elastic-plastic constitutive model for thermal shocked oxide/oxide ceramic-matrix composites. *International Journal of Mechanical Sciences*, 175, 105528.

[283] You, T., Zhu, Q.-Z., Li, P.-F., & Shao, J.-F. (2020). Incorporation of tension-compression asymmetry into plastic damage phase-field modeling of quasi brittle geomaterials. *International Journal of Plasticity*, 124, 71–95.

[284] Yousef, S. G., Rodel, J., Fuller, E. R., Zimmermann, A., & El-Dasher, B. S. (2005). Microcrack evolution in alumina ceramics: Experiment and simulation. *Journal of the American Ceramic Society*, 88(10), 2809–2816.

[285] Zamani, A. & Eslami, M. R. (2010). Implementation of the extended finite element method for dynamic thermoelastic fracture initiation. *International Journal of Solids and Structures*, 47(10), 1392–1404.

[286] Zhang, P., Hu, X., Bui, T. Q., & Yao, W. (2019a). Phase field modeling of fracture in fiber reinforced composite laminate. *International Journal of Mechanical Sciences*, 161, 105008.

[287] Zhang, P., Hu, X., Wang, X., & Yao, W. (2018). An iteration scheme for phase field model for cohesive fracture and its implementation in abaqus. *Engineering Fracture Mechanics*, 204, 268–287.

[288] Zhang, P., Hu, X., Yang, S., & Yao, W. (2019b). Modelling progressive failure in multi-phase materials using a phase field method. *Engineering Fracture Mechanics*, 209, 105–124.

[289] Zhang, X., Krischok, A., & Linder, C. (2016). A variational framework to model diffusion induced large plastic deformation and phase field fracture during initial two-phase lithiation of silicon electrodes. *Computer Methods in Applied Mechanics and Engineering*, 312, 51–77.

[290] Zhang, X., Sloan, S. W., Vignes, C., & Sheng, D. (2017). A modification of the phase-field model for mixed mode crack propagation in rock-like materials. *Computer Methods in Applied Mechanics and Engineering*, 322, 123–136.

[291] Zhang, X.-Y. & Li, X.-F. (2017). Thermal shock fracture of a cracked thermoelastic plate based on time–fractional heat conduction. *Engineering Fracture Mechanics*, 171, 22–34.

[292] Zhou, S., Rabczuk, T., & Zhuang, X. (2018a). Phase field modeling of quasi-static and dynamic crack propagation: Comsol implementation and case studies. *Advances in Engineering Software*, 122, 31–49.

[293] Zhou, S. & Zhuang, X. (2020). Phase field modeling of hydraulic fracture propagation in transversely isotropic poroelastic media. *Acta Geotechnica*, 15, 2599–2618.

[294] Zhou, S., Zhuang, X., & Rabczuk, T. (2019a). Phase field modeling of brittle compressive-shear fractures in rock-like materials: A new driving force and a hybrid formulation. *Computer Methods in Applied Mechanics and Engineering*, 355, 729–752.

[295] Zhou, S., Zhuang, X., & Rabczuk, T. (2019b). Phase-field modeling of fluid-driven dynamic cracking in porous media. *Computer Methods in Applied Mechanics and Engineering*, 350, 169–198.

[296] Zhou, S., Zhuang, X., Zhu, H., & Rabczuk, T. (2018b). Phase field modelling of crack propagation, branching and coalescence in rocks. *Theoretical and Applied Fracture Mechanics*, 96, 174–192.

[297] Zhuang, X. & Zhou, S. (2020). An experimental and numerical study on the influence of filling materials on double-crack propagation. *Rock Mechanics and Rock Engineering*, 53(12), 5571–5591.

[298] Ziaei-Rad, V., Shen, L., Jiang, J., & Shen, Y. (2016). Identifying the crack path for the phase field approach to fracture with non-maximum suppression. *Computer Methods in Applied Mechanics and Engineering*, 312, 304–321.